PRECIPITATION ESTIMATION USING C-BAND DUAL POLARIMETRIC WEATHER RADAR

DIAR M. HASSAN

A DISSERTATION SUBMITTED TO THE FACULTY OF GRADUATE STUDIES
IN PARTIAL FULFILMENT OF THE REQUIREMENTS
FOR THE DEGREE OF
DOCTOR OF PHILOSOPHY

Graduate Program in
Earth and Space Science
York University
Toronto, Ontario
October 2015

Abstract

Radar Quantitative Precipitation Estimation (QPE) plays an important role in weather forecasting, especially nowcasting, and hydrology. This study evaluates the current QPE algorithm implemented by the Canadian Radar Network of Environment Canada, suggests an improved algorithm, and also evaluates the use of polarimetric radars for estimation of Snow Water Equivalent (SWE), solid snowfall, and rainfall rates. Data from the dual polarimetric C-band King City radar (CWKR) near Toronto, Ontario, SWE and solid snowfall rates from Oakville, Ontario, SWE from the CAN-Now project at Pearson International Airport (CYYZ), Toronto, Ontario, and Mount Pearl, Newfoundland were used in this project.

The ground observations show that the polarimetric variables could be used to infer a few of the microphysical processes during snowfall. It is suggested that the co-polar correlation coefficient (ρ_{hv}) could be sensitive to the size ranges of different snow habits within the radar sampled volume. Also, higher differential reflectivity (Z_{DR}) values were measured with large aggregates due to the Mie resonance effect, lower fluttering angles, or induced field transverse.

Data from the three sites were used to develop $S(Z_{eH})$-based algorithms at 1 hr interval SWE, where Z_{eH} is the radar equivalent reflectivity factor. Similarly, two additional algorithms were developed using SWE at 10 min intervals from CYYZ and Mt. Pearl but they were found to have less skill. A modest difference was found between $S(Z_{eH})$ and the polarimetric algorithm, $S(Z_{eH}, Z_{DR})$, in estimating SWE. The 1 hr interval

SWE accumulation from the three sites were combined to develop an additional $S(Z_{eH})$ algorithm which had statistically better results. The results show that the current Environment Canada algorithms underestimate SWE and solid snowfall rates. The similarity of the $S(Z_{eH})$ algorithms for CYYZ and Mount Pearl suggests that the same algorithm could be used for many sites.

A strong correlation was found between radar reflectivity factor and ground solid snowfall measurement. Accordingly, $S(Z_{eH})$ and $S(Z_{eH}, Z_{DR})$ algorithms were established to directly estimate solid snowfall rates on the ground. The $S(Z_{eH})$ was found to have superior results compared to the $S(Z_{eH}, Z_{DR})$.

Finally, the polarimetric variables were found to be useful in estimating rainfall rates. Thus, three rainfall algorithms ($R(Z_{eH})$, $R(Z_{eH}, Z_{DR})$, $R(K_{DP})$) were established and compared against the current algorithm employed by the Environment Canada and counterpart algorithms from the United Kingdom. A logic tree was devised with certain polarimetric thresholds to choose the optimal algorithm among the three established ones. It appears that for rain, unlike for snow, the polarimetric parameters are very useful for quantitative precipitation estimation.

Dedication

To my better half, Collette, and the apples of my eyes, Dara and Alan.

Acknowledgements

I would like to thank my co-supervisors, Prof. Peter A. Taylor and Prof. George A. Isaac, for their continuous support and scientific advice throughout the course of this research. I would also like to thank Janti Reid, Robert Crawford, Dr. David Hudak, Dr. Norman Donaldson, and Vlado Stojanovic from the Cloud Physics and Severe Weather Research Division at Meteorological Service of Canada for aiding in providing radar data, weather observation data, and their knowledge and expertise. I would like to thank NSERC Discovery grant for partial financial support.

Table of Contents

List of Tables

List of Figures

CHAPTER ONE

1.1 Introduction

Winter snow storms have moderate-to-severe impact on airports, cities, and communities located at higher latitudes. Among other tools, meteorologists and hydrologists rely on weather radars in preparing their daily forecasts, while radar data are also assimilated in Numerical Weather Prediction (NWP) and hydrological models. Polarimetric radars are capable of providing a more detailed picture of falling hydrometeors through measurements that are less susceptible to attenuation, radar calibration errors, partial beam blockage, and anomalous propagation (Zrnić and Ryzhkov, 1996). For such reasons polarimetric radars are sought by many weather research and operational centers across the globe.

Weather radars are classified based on their frequency with the main three ground-based radar are S-band (2 to 4 GHz), C-band (4 to 8 GHz), and X-band (8 to 12 GHz). Conventional weather radar transmits and receives electrical pulses in one state of polarization, usually horizontally. The returned power, in the same state of polarization as the transmitted power, is then converted to radar equivalent reflectivity factor, Z_{eh} (dBz), as will be explained later in this chapter. Meanwhile, dual-polarized radars can be set up to receive two orthogonally polarized signals, horizontal and vertical at the same time. The returned power is then converted, as will be explained later in this chapter, to Z_{eh} (dBz), differential reflectivity (Z_{dr} in dB), and differential phase shift (φ_{dp} in degrees). It

is worth noting that the small letter (z) at the end of the Z_{eh} unit is only to distinguish it from the Z_{dr}. The amplitude of the returned signal and φ_{dp} is then used to calculate a parameter named correlation coefficient (ρ_{hv}) while the specific differential phase shift (K_{DP} in $^\circ$ km^{-1}) is derived from φ_{dp}. Thus, the polarimetric radars are able to provide more detailed images of meteorological targets and also to distinguish between meteorological and non-meteorological targets.

It is worth noting here that capital letter subscripts used with reflectivity and differential reflectivity will indicate the linear form of both parameters while small letter subscripts indicate the logarithmic form ($\log_{10}$). Also, the terms reflectivity and equivalent radar reflectivity are interchangeable.

Active research with dual-polarized weather radars started several decades ago and was mainly focused on rainfall estimation. It was confirmed through many studies (e.g. Ryzhkov et al. 2001, Baldini et al. 2008, Vulpiani et al. 2009) that polarimetric radar based rainfall algorithms do add value in comparison to the conventional Z-R relationships used in single-polarized radars. Although there is no consensus on the degree of improvement and the choice of an optimal polarization relation for rainfall estimation (Ryzhkov et al. 2005) due to the different rainfall regimes, all studies confirm that polarimetric based rainfall algorithms outperform the conventional Z-R algorithms in moderate-to-heavy rainfall events. Cremonini and Bechini (2010) compared different rainfall algorithms during two flash floods in Ligurian Apennines, Italy, using a network of tipping buckets and C-band radar. They concluded that the K_{DP}-based and ZPHI algorithms are remarkably better than non-polarimetric algorithms. The ZPHI algorithm

uses differential phase shift between two range gates on the same ray to correct for rain attenuation. While studying polarimetric rainfall retrieval from C-band weather radar in a tropical environment in the Philippines, Crisologo et al. (2014) found that rainfall retrieval from K_{DP} substantially improved rainfall estimation at both daily and hourly time scales. The daily K_{DP}-based rainfall accumulations showed a very low estimation bias and small random errors while random scatter was strongly present in hourly accumulations.

Dual polarized radars are capable of simultaneously or alternately transmit and receive linear horizontally and vertically polarized waves. Based on the number of transmitters and receivers, there are four modes of dual polarization Simultaneous Transmit Simultaneous Receive (STSR), Simultaneous Transmit Alternating Receive (STAR), Alternating Transmit Simultaneous Receive (ATSR), and Alternating Transmit Alternating Receive (ATAR). The King City (CWKR) radar and the National Weather Service, USA, use the STSR mode with a slant-linear 45° technique to transmit the two orthogonally polarized waves. One of the advantages of using STSR mode is that both polarized waves are simultaneously sampled. The slant-linear 45° technique is used to detect super-cooled large drops which are considered hazardous to aircraft icing in addition to distinguish between column-like and plate-like crystals (Bringi and Chandrasekar, 2001).

When compared to rainfall, there are less polarimetric radar studies during snowfall events. However, Hogan et al. (2002), Ikeda et al. (2005) and Andric et al. (2010) have indicated that aggregates are associated with small differential reflectivity

Z_{dr} and large reflectivity Z_h. Ikeda et al. (2005) noticed an increase in Z_{dr} with a decrease in Z_{eh}. The authors attributed this inverse behaviour to an increase in bulk density as the number of aggregates decreased and that of compact graupel increased. Meanwhile, Andric et al. (2010) noticed that their maximum measured Z_{dr} was at the -10°C layer where dendritic habits are dominant. While using an X-band polarimetric radar with several weather stations in the eastern Swiss Alps, Schneebeli et al. (2013) showed that the radar variables were able to well capture the evolution of snowflakes from pristine crystals to dendritic crystals to large aggregates. With the aid of a hydrometeor identification scheme they showed that graupel-like particles are found to be dominant right above the melting layer for snow events with high accumulation intensities. A winter storm producing ice pellets was studied by Kumjian et al. (2013) using S-band polarimetric radars. They found a unique signature that marks a re-freezing of hydrometeors below the bright band. This signature is comprised of an enhancement of differential reflectivity Z_{dr} and specific differential phase K_{DP} with a decrease of reflectivity factor Z_{eh} and co-polar correlation coefficient ρ_{hv}.

Hogan et al. (2002), observed a broad band of high Z_{dr} values (around 3 dB) while using an S-band polarimetric radar. The in-situ aircraft observations indicated that pristine ice columns with axial ratios of around 5:1 were responsible for the high Z_{dr} observed by the radar. On the same day a number of plumes of high Z_{dr} (up to 7 dB) in the vicinity of the cloud tops (-15°C) were visible to the radar. The authors attributed such high values of Z_{dr} to plates and dendrites. This matched their theoretical findings that columnar crystals alone, even at their maximum axial ratios, cannot produce values

of Z_{dr} greater than 4 dB, while planar crystals can attain values of up to 10 dB. While using measurements from an S-Band polarimetric radar during winter storms in northeastern Colorado, Kennedy and Rutledge (2011) found that local K_{DP} maxima of (~0.15° to 0.4° km^{-1}) in an elevated layer near the -15°C environmental temperature isotherm are associated with increased precipitation rates. Their microwave scattering model indicated that populations of highly oblate ice particles with moderate bulk densities and diameters in the (~0.8 to 1.2 mm) range can generate K_{DP} and Z_{dr} values that are consistent with the radar observations. This suggests that rapidly growing dendrites likely played a significant role in the production of the observed K_{DP} patterns. They concluded that localized regions of K_{DP} greater than (~0.1° to 0.2° km^{-1}) can be used to identify regions of active dendritic growth, and hence an increase in snowfall rates at the surface. During the Mesoscale Alpine Programme (MAP) field experiment, Rodriguez et al. (2001) found no added value from polarimetric radar for snowfall rate estimation in the Alpine regions. Instead, the authors explored the concept of utilizing different Z-S relationships for different snow crystals.

Rasmussen et al. (2003) provided a description and evaluation for surface-point nowcasting snow-water equivalent (SWE) algorithm. Their method corrected real-time (Z_{eH}) with snow gauge rates. The method showed skill in nowcasting SWE out to at least 1h given a well-shielded snow gauge and appropriate range corrections. This method is not applied in this study. Multiple (Z_{eH}-S) power-law relations were derived by Huang et al. (2010), where Z_{eH} is equivalent radar reflectivity factor and S is liquid equivalent snowfall rate, using WKR radar and a 2D video distrometer (2DVD). The 2DVD images

were used to compute the apparent volume and equi-volume spherical diameter (D_{app}). They computed the snow density using ($\rho = \alpha D_{app}^{\beta}$) where α and β are assumed to be variable while a third parameter, γ, is used to account for strong horizontal winds that tend to decrease the measured concentrations from the 2DVD. The three parameters (α, β, and γ) are determined by minimizing the difference between the radar reflectivity and the equivalent reflectivity computed from the 2DVD in a least squares sense. The Z_e-SR relations were then validated against manually recorded accumulations from the double-fence international reference (DFIR) gauge at the same location (CARE site). The power-law algorithms introduced by Huang et al. (2010) will be used to examine the skills of the algorithms produced in this study.

Following on from the earlier work the present study aims to evaluate the ability of polarimetric radars in estimating SWE using observation data from Greater Toronto Area and the King City radar (CWKR) located just north of Toronto.

1.2 Radar Theory and Project Data

1.2.1 Polarimetric Radar Theory

In addition to pure destruction, sometimes technological developments that serve humanity are an outcome of wars. Precipitation echoes were considered as clutter when first detected during World War II in 1940-1941 but led to the first publication regarding meteorological echoes published in 1943 (Bent 1943). Hitschfeld (1986), Atlas (1990), Rogers and Smith (1996), and Whiton et al. (1998) documented the early development of such usage. The "Stormy Weather" radar research group at McGill University established cutting edge radar research during the Second World War. The latter research was carried on by J. S. Marshall after the war. By 1997 the Canadian radar network was comprised of 19 radars, with 18 radars being C-Band and one S-Band at McGill. One year later, Environment Canada added 12 more radars while upgrading the network to Doppler Radars.

Thirty years after the war, an intense era of radar polarimetry research was started and amazingly is still going on. By simultaneously transmitting not one, but two orthogonal pulses, a vertical and a horizontal one, two independent sets of data will be received by the radar. The returned signal is then used to produce more parameters instead of just reflectivity.

1.2.2 Radar Equations

Using the Rayleigh scattering theory (John Strutt, 1899), the dipole moment (p) induced in a hydrometeor spherical particle is proportional to the magnitude of the incident electric field, (E_{inc}), the hydrometeor volume (D^3) with a diameter (D) in (mm), and the dielectric property of the hydrometeor (K).

$$p = \frac{\pi \varepsilon_0 K D^3 E_{inc}}{2} \tag{1.1}$$

where, ε_0 is the permittivity of free space (Farads/m). The intensity of the scattered electric field (E_r) by the hydrometeor is:

$$E_r = \frac{\pi p}{\lambda^2 \varepsilon_0 r} \tag{1.2}$$

where, r is the distance between the receiver and hydrometeor and λ is the radar wavelength. Re-arranging Equation (1.2) for p and substituting it in Equation (1.1) leads to:

$$E_r = \frac{\pi^2 K D^3 E_{inc}}{2\lambda^2 r} \tag{1.3}$$

The radar cross section equation, σ, can be written as:

$$\sigma = 4\pi r^2 \frac{S_r}{S_{inc}} \tag{1.4}$$

where, S_r is the scattered power density at range r, in (W/m^2) and S_{inc} is the power density that is intercepted by the hydrometeor, in (W/m^2).

Since, $\left(\frac{E_r}{E_{inc}}\right)^2 = \left(\frac{S_r}{S_{inc}}\right)$, squaring Equation (1.3) and substituting it in Equation (1.4) yields:

$$\sigma = \frac{\pi^5 |K|^2 D^6}{\lambda^4} \tag{1.5}$$

It is worth noting that the dielectric factor of the hydrometeor, *K*, is a complex number representing the scattering and absorption characteristics of the precipitating medium and can be written as:

$$K = \frac{\varepsilon_r - 1}{\varepsilon_r + 2} \tag{1.6}$$

Where, ε_r is the ratio of the medium permittivity, ε_1, to free space permittivity, ε_0. In other words, $|K|^2$, is a function of temperature and wavelength.

Summing Equation (1.5) for an array of hydrometeors yields:

$$\bar{\sigma} = \sum_j \sigma_j = \frac{\pi^5 |K|^2}{\lambda^4} \sum_j D_j^6 \tag{1.7}$$

Using Equation (1.7) and $|K|^2$ of water, $|K|_w^2$, one can write the radar reflectivity as:

$$\bar{\eta} = \frac{\sum_j \sigma_j}{V_c} = \frac{\pi^5 |K|_w^2}{\lambda^4} \frac{\sum_j D_j^6}{V_c} \tag{1.8}$$

where V_c is radar volume scan. The images seen on weather radar displays are representative of the logarithms of $\frac{\sum_j D_j^6}{V_c}$, which is termed the radar reflectivity factor, *Z*,

in (mm^6 m^{-3}) of spherical drops with diameters small compared to the radar wavelength and is equal to the radar equivalent radar reflectivity factor, Z_e.

The radar equation for a distributed target can be written as:

$$P_r = \frac{c}{\pi^2 1024 \ln(2)} \left[P_t \tau G^2 \lambda^2 \Phi \Theta \right] \left[\frac{\bar{\eta}}{r^2} \right] \tag{1.9}$$

where P_t is the transmitted power, τ is the pulse duration, G^2 is the antenna gain, Φ is the vertical radar beamwidth, and Θ is the horizontal radar beamwidth.

Substituting Equation (1.8) in (1.9) and arranging for Z, yields:

$$Z = \frac{1024 \ln(2)}{c \pi^3} \left[\frac{\lambda^2}{P_t \tau G^2 \Phi \Theta} \right] \left[\frac{\overline{P_r} r^2}{|K|^2} \right] \tag{1.10}$$

where Z is measured in (mm^6 m^{-3}).

When the radar volume sample encounters frozen hydrometeors, Marshall and Gunn (1952) showed that the irregular shape of the ice particles is irrelevant since they are composed of a weak dielectric. Hence, the radar cross section of such particles is the same as that of sphere of the same mass.

When the radar volumetric sample is mainly composed of frozen hydrometeors, the radar reflectivity, η, Equation (1.8) can be re-written as:

$$\bar{\eta} = \frac{\pi^5 |K|_i^2}{\lambda^4} \frac{\sum_j D_j^6}{V_c} \tag{1.11}$$

Smith (1984) showed that $Z=Z_e$ for spherical rain particles, re-arranging Equation (1.8) for Z_e ($Z_e = \frac{\lambda^4 \eta}{\pi^5 |K|_w^2}$) and substituting η with its equivalent in Equation (1.11) yields:

$$Z_e = \frac{|K|_i^2}{|K|_w^2} \frac{\sum_j D_j^6}{V_c} = \frac{|K|_i^2}{|K|_w^2} Z \tag{1.12}$$

The dielectric factor for water, $|K|_w^2$, is equal to (0.93). Depending on how the hydrometeor particle sizes are determined, $|K|_i^2$ can have two values. If the melted drop diameters are used in calculating Z, as in Gunn and Marshall (1958) and Sekhon and Srivastava (1970), $|K|_i^2$ is equal to 0.208. Using the logarithmic form, Equation (1.12) can be written as:

$$Z_e(dBz) = Z(dBz) - 6.5dBz \tag{1.13}$$

While if equivalent ice sphere diameters used in particle sizes, $|K|_i^2$ would be equal to 0.176 and logarithmic form of Equation (1.12) is represented as:

$$Z_e(dBz) = Z(dBz) - 7.2dBz \tag{1.14}$$

It is worth noting that the Canadian Radar Network is setup to assume melted drop diameters when calculating reflectivity factors, thus Equation (1.13) would be the appropriate form to use during winter season and one can notice a (6.5 dB) difference in reflectivity between winter and summer modes. Accordingly, 6.5 dBz was added to the reflectivity factor values used in chapters 3 and 4 (SWE and solid snow).

1.2.3 Power-Law Relationship

For many decades it has been a common practice to use a power-law relationship between reflectivity factor and precipitation rate (Smith and Krajewski 1993). Radar

reflectivity factor and precipitation rate are related to each other via the raindrop size distribution. To explain this further, the reflectivity factor can be given as a function of size distribution of raindrops in a radar sample as (Battan 1973):

$$Z = \int_0^\infty D^6 N_V(D) dD \tag{1.15}$$

where $N_V(D)dD$ represent the mean number of raindrops with equivalent spherical diameters between D and $D+dD$ (mm) present in a unit volume of air (the subscript $_V$ stands for volume). And $N_V(D)$ is in (mm^{-1} m^{-3}). Since the estimated Z from the radar is always affected by one or a combination of radar calibration, Rayleigh scattering, attenuation, beam shielding and anomalous propagation, meteorologists and radar engineers always use reflectivity factor instead. After fitting raindrop size spectra to filter paper measurements for rain rates between 1 and 23 mm h^{-1}, Marshal and Palmer (1948) proposed a negative exponential parameterisation for the raindrop size distribution as:

$$N_V(D) = N_0 e^{(-\Lambda D)} \tag{1.16}$$

where N_0 (mm^{-1} m^{-3}) is the raindrop concentration and Λ (mm^{-1}) is the slope of $N_V(D)$. Marshall and Palmer found that N_0 was approximately constant (8000 mm^{-1} m^{-3}) and Λ decreased with increasing rain rate R (mm h^{-1}) according to ($\Lambda = 4.1R^{-0.21}$).

Although recent studies suggest a gamma distribution (e.g. Ulbrich, 1983) or a lognormal form (e.g. Feingold and Levin, 1986), the exponential form of Marshal and Palmer is still widely used as empirical evidence shows that averages raindrop size distribution generally tend to the exponential form (Joss and Gori, 1978, Ulbrich and Atlas, 1998).

On the other hand, rain rate (mm h^{-1}) is related to raindrop size distribution $N_V(D)$ as (Uijlenhoet 2001):

$$R = 6\pi \times 10^{-4} \int_0^{\infty} D^3 v(D) N_V(D) dD \tag{1.17}$$

where $v(D)$ is the terminal velocity in still air (m s^{-1}) of the equivalent spherical raindrop with a diameter D in (mm).

Equations (1.15) and (1.17) reveals that the raindrop size distribution $N_V(D)$ (and to a lesser extent the terminal velocity) ties Z and R together. The simplest form of $v(D)$-relationship is a power law one ($v(D) = cD^{\gamma}$) where (c) and (γ) can be obtained through empirical measurements. To complicate matter further, Z is measured aloft while R is estimated at ground level.

Weisuer (1895), measured the raindrop size distribution by the "absorbent-paper method" which consisted of exposing sheets of filter paper, dusted with dye, to the rain and measuring the size of spots caused by raindrops. In 1983, Oguchi used the "flour method" to measure raindrop size distribution. In this method a pan containing fine flour was exposed to the rain and the size of the produced pellets was converted size of the raindrops through a relationship that equates the size of the dried pellets and the size of raindrops. Among the size measurements by the flour method, the most notable one would be the measurements by Laws and Parsons (1943). They made extensive measurements in Washington D.C., for various types of rain. They noticed that even for the same rain rate the size distributions vary considerably from rain to rain, and hence they averaged distributions for each rain rate. Sempere Torres et al. (1994, 1998) have

demonstrated that all the previous proposed parameterisations of the raindrop size distribution are special cases of a general formulation which takes the form of a scaling law. The size distribution here depends on the raindrop diameter *(D)* and on the value of a reference variable, commonly taken to be the rain rate (R mmh^{-1}). The generality of this formulation stems from the fact that it is no longer necessary to impose an *a priori* functional form for the raindrop size distribution. It leads to the ubiquitous power law relationships between rainfall integral parameters between the radar reflectivity factor and rainfall rate (Uijlenhoet 2001). Sempere Torres et al. (1994, 1998) parameterized the raindrop size distribution as:

$$N_V(D,R) = R^{\alpha} g\left(\frac{D}{R^{\beta}}\right) \tag{1.18}$$

where $N_V(D, R)$ (mm^{-1} m^{-3}) is the raindrop size distribution as function of the raindrop diameter D (mm) and rain rate R (mm h^{-1}), α and β are scaling exponents, and $g(x)$ is the general raindrop size distribution as a function of the scaled raindrop diameter $x=D/R^{\beta}$. The values of α and β and $g(x)$ depend on the choice of R but do not have any functional dependence on its value (Uijlenhoet 2001).

Substituting Eq. 1.18 into 1.15 leads to (Uijlenhoet 1999):

$$Z = aR^{b} \tag{1.19}$$

with $(a = \int_0^{\infty} x^6 g(x)dx)$ and $(b = \alpha + 7\beta)$. Thus, (a) and (b) of any power law Z-R relationships is determined by the shape of the raindrop size distribution, whereas, the linear combination of the values of the scaling exponents determines the exponents of the Z-R relationship (Uijlenhoet 2001).

On the other had and based on raindrop size distributions at ground level while assuming the simple *v(D)*-relationship, there is an overwhelming empirical evidence of a power law relationship of the form (Marshall et al. 1947 and Battan 1973)

$$Z = aR^b \tag{1.20}$$

where (*a)* and (*b)* are coefficients that vary from place to place to even during a single rainfall event.

1.2.4 Polarimetric Variables

For half a century, the diversity in radar polarization witnessed development and research in United Kingdom, United States, Soviet Union, and Canada (Browne and Robinson 1952; Hunter 1954; Newell et al. 1955; Wexler 1955; Shupyatsky 1959; Gerzenshon and Shupyatsky 1961; Shupyatsky and Morgunov 1963; Minervin and Shupyatsky 1963; Morgunov and Shupyatsky 1964). More information about the scatterers is encoded in a dual polarized electromagnetic pulse. Each of the polarized waves, i.e. horizontal and vertical, will be reflected back with the same state of polarization, but with degrees of difference, such as the phase angle between the horizontal and vertical pulse and the amplitude of the returned power depending on the type, shape, orientation, tumbling, and density of the scatterers. In addition to the horizontal reflectivity factor (Z_{eH} in dB) obtained from a conventional single polarized radar, a new set of variables can be obtained from dual polarized radars, such as differential reflectivity (Z_{DR} in dBz), differential phase shift (ϕ_{dp} in deg), specific differential phase shift (K_{DP} in °/km), and co-polar correlation coefficient (ρ_{hv}). These

variables are obtained when the radar simultaneously transmits and receives the orthogonally polarized pulses. In addition to the above mentioned variables, linear depolarization ratio (LDR) can be obtained when the radar separately transmits and receives horizontal and vertical pulses. Each one of these variables carries a piece of the puzzle about the scatterers. In addition to the microphysical information about the scatterers, dual polarimetric variables are used to improve radar quality data during the pre-processing stage by suppressing ground clutter and identifying biological scatterers such as birds and insects. Each of the polarimetric variables is briefly described below.

1.2.4.1 Reflectivity Factor (Z_{eH})

Conventional Doppler radars transmit single horizontal pulses and the reflectivity factor is one of three moments received when the pulse encounter a scattering medium. The other two moments are the Doppler velocity (V_r) which is the mean Doppler frequency shift of the scatterers within the sampled volume, and the Doppler spectrum width (W) which measures the scatterers' Doppler velocity variability within the same volume. As mentioned earlier, Z_{eH} correlates to precipitation rates and is weighted toward bigger size scatterers since (Z_{eH} α D^6). Although this variable was and is still largely used to estimate precipitation rates, it shows misleading rainfall rates during rain-hail mixed events or when large snow aggregates are present within the radar sampled volume. While the scattered electromagnetic radiation from ice particles are less than that of rain (by about 6.5 or 7.2 dBz depending on how $|K|_i^2$ is used) due to their low density when compared to liquid water, it is still hard to differentiate rain from snow using only Z_{eH}

without knowing the environmental temperature. Z_{eH} is affected by signal to noise ratio (SNR), Mie scattering, antenna calibration errors, attenuation, and partial beam blockage.

1.2.4.2 Differential Reflectivity (Z_{DR})

The ratio of the horizontal to vertical reflectivity is known as the differential reflectivity (or the logarithmic difference between the reflectivity at the two channels) and it can be written as (Seliga and Bringi 1976):

$$Z_{dr} = 10\log_{10}\left(\frac{Z_H}{Z_V}\right) \tag{1.21}$$

where Z_{dr} in (dB) and Z_H and Z_V in ($mm^6\ m^{-3}$). Equation (1.18) can be simplified as:

$$Z_{dr} = Z_h - Z_v \tag{1.22}$$

where Z_{dr} in (dB) and Z_h and Z_v in (dB).

The cartoon below in Figure (1.1) illustrates a dual polarized pulse and a single rain drop. There are different forces that affect falling raindrops such as surface tension, internal circulation and electrostatic forces in addition to the collision and coalescence mechanisms. All these factors affect the shape and oscillation of falling raindrops.

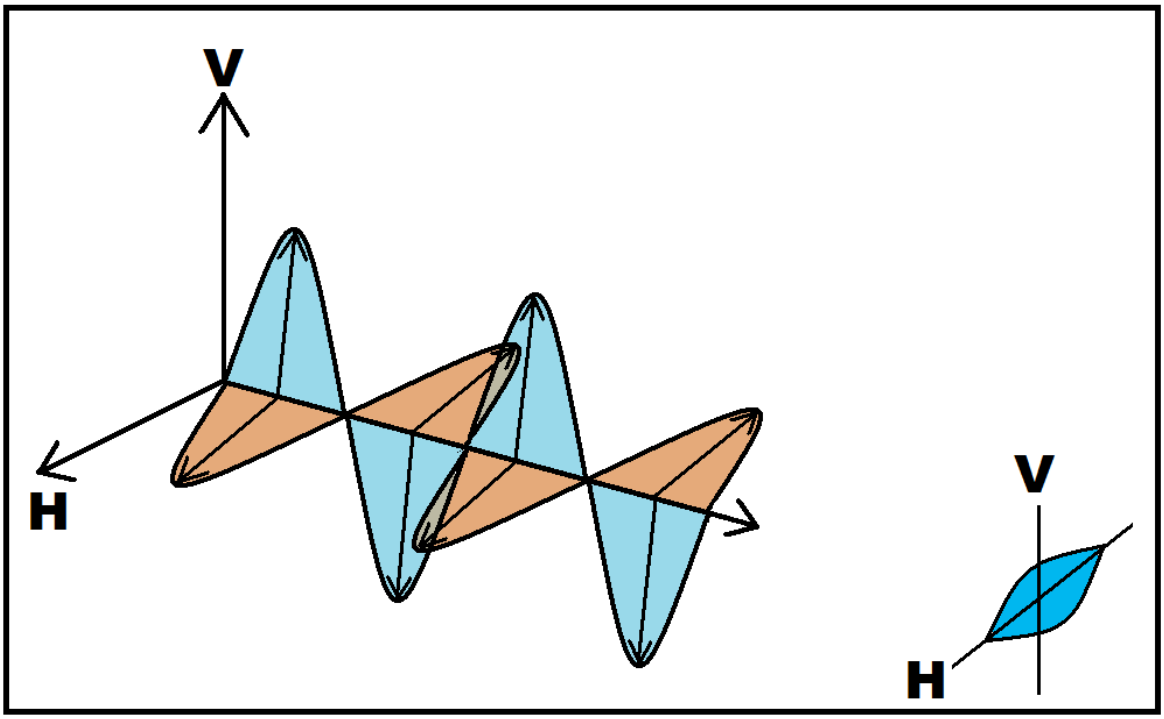

Figure (1.1) Two orthogonal electromagnetic waves intercepting an oblate raindrop.

Since Z_{dr} is a weighted reflectivity factor, it can be used to infer the shape and orientation of scatterers within the sample volume. Z_{dr} tend to be positive for oblate scatterers (horizontally oriented), near zero for spherical scatterers and negative for oblate scatterers (vertically oriented). Z_{dr} is affected by Mie scattering, SNR, scatterers density, antenna calibration, and differential attenuation.

1.2.4.3 Specific Differential Phase Shift (K_{DP})

As the radar electromagnetic pulses encounter scatterers of different shapes and orientations, the two orthogonal waves tend to experience a differential phase shift (ϕ_{dp}) due to the difference in the propagation speed between the two orthogonal waves as they

pass through the medium. The specific differential phase shift (K_{DP}) is calculated as the range derivative of ϕ_{dp} over finite paths and can be expressed as (Bringi and Chandrasekar, 2001):

$$K_{DP} = \frac{\phi_{dp}(r_2) - \phi_{dp}(r_1)}{2(r_2 - r_1)} \tag{1.20}$$

where K_{DP} in (°/km), ϕ_{dp} in (°) and r_1 and r_2 are distances in (km).

The higher the density of the horizontally aligned scatterers within the sampled volume, the greater ϕ_{dp} and K_{DP}. Thus, K_{DP} is proportional to drop concentration and size and correlated to the total liquid water content within the sampled volume. Although K_{DP} is unaffected by absolute antenna calibration, partial beam blockage and attenuation, a trade-off between range resolution and accuracy of K_{DP}-based precipitation estimation can be expected because ϕ_{dp} tend to be noisy over short ranges, thus affecting derived K_{DP} values. There are several approaches used to estimate K_{DP}, e.g. Otto and Russchenberg, (2011), Wang and Chandrasekar (2009) and Hubbert and Bringi (1995). The least squares-fit method over 6 km is used by King City Radar (CWKR) processor to calculate K_{DP}.

1.2.4.4 Co-Polar Correlation Coefficient (ρ_{hv})

The magnitude and phase of the backscattered electric field components received in the horizontal and vertical channels can be used to measure the uniformity in size, shape, and type of sampled hydrometeors. ρ_{hv} takes values between 0 and 1, where the 1 resembles a sample of particles that are close in size, shape, and/or orientation. In

addition to the other polarimetric variables, ρ_{hv} plays a major role in hydrometeor identification process. ρ_{hv} can be defined as (Zrinc et al. 2006):

$$\rho_{hv} = \frac{\left\langle S_{vv} S_{hh}^{*} \right\rangle}{\sqrt{\left(\left\langle S_{hh}^{2} \right\rangle \left\langle S_{vv}^{2} \right\rangle\right)}} \tag{1.21}$$

where S_{vv} and S_{hh} denote the co-polar backscattered electric field components in the vertical and horizontal direction, respectively. The angular brackets are statistical average of the scattering electric field components and the (*) refers to the complex conjugate.

1.2.4.5 Linear Depolarization Ratio (LDR)

Unlike weather radars that are able to simultaneously transmit and receive two orthogonally polarized waves, linear depolarization ratio (LDR) can be calculated from radars that are able to separately transmit and receive horizontally and vertically polarized waves. LDR is the ratio of the received power in the cross polarized channel with respect to the co-polar received power. In other words, when a horizontally polarized wave is transmitted, LDR_H is the ratio of the backscattered vertically polarized power to the horizontally backscattered polarized power. Minimum values of LDR_H can be measured when only spherical particles, e.g. drizzle, are present in the sampled volume while higher values are realized within the bright band (the area around the freezing level where below it rain is detected and snow above it) and rain-hail mixed regions. LDR equation can be written as:

$$LDR_{vh} = 10\log\left(\frac{\left\langle |S_{HV}|^2 \right\rangle}{\left\langle |S_{HH}|^2 \right\rangle}\right) = 10\log\left(\frac{Z_{HV}}{Z_{HH}}\right)$$

$$LDR_{hv} = 10\log\left(\frac{\left\langle |S_{HV}|^2 \right\rangle}{\left\langle |S_{VV}|^2 \right\rangle}\right) = 10\log\left(\frac{Z_{HV}}{Z_{VV}}\right) \quad (1.22)$$

where, $LDR_{VH,HV}$ are the horizontal and vertical linear depolarization ratio in (dB), S_{VH} is the cross-polar backscattered electric field component in the horizontal and vertical channels (similarly for Z_{HV}), and S_{HH} and S_{VV} are the co-polar backscattered electric field components in the vertical and horizontal direction (similarly for Z_{HH} and Z_{VV}), respectively. Just like Z_{DR}, LDR depends on the reflectivity ratio. Hence, it is independent of drop concentration and absolute radar calibration. Due to the weaker cross-polar (depolarized) signal when compared to the co-polar (2 to 3 orders of magnitude), LDR is susceptible to noise contamination (second trip contamination), propagation effects, antenna misalignments, channels coupling, and finally if the two channels orthogonal or not (Brandes, 2000).

1.3 Project Data

This section contains a description of site location and weather data that has been collected from all three sites in addition to the properties of the King City radar (CWKR) in Ontario and Holyrood radar (CWTP) in Newfoundland and the type of data used from each radar.

1.3.1 Weather Data

Both manual and automatically recorded observations have their advantages and disadvantages. There is no doubt that observational tasks become more complex during the winter season. Rasmussen et al. (2012) showed that the GEONOR gauge is still widely used in different field sites, but different SWE measurements can be obtained for the same gauge using different shields and site set up. Three observation sites were selected to gather snowfall measurements for this study.

1.3.1.1 Oakville, Ontario

A field campaign in Oakville, Ontario was set up during Jan-April, 2011 to study snow microphysical properties and to provide this project with snowfall accumulation measurements. The site location is ideal for snow measurements due to its fenced area which minimized the effect of blowing and drifting snow. An acrylic tank with square orifice inner area of 207 cm^2 was used to collect solid snowfall and measure Snow Water Equivalent (SWE) in millimeters. A circular table of 150 cm in diameter was chosen as a base surface to measure solid snowfall accumulation in centimeters. Crystal types,

crystals/flakes maximum dimension and their melted diameters were manually recorded during each observation. Figure (1.2) shows a collection of pictures during an observation in Jan, 2012. Each hour, when snowfall had occurred, the accumulated snow in the acrylic tank was gently melted in a tepid water bath to minimize the effect of evaporation while a medical syringe was utilized to measure the volume of the melted snow. Using a medical syringe minimized the wetting loss by removing every single drop of liquid from the container. A great deal of care was taken during each observation. Solid snowfall measurements ranged between (0.5 and 6.5 cm h^{-1}) while SWE measurements ranged between (0.1 and 3.7 mm h^{-1}) with no wet snowfall cases included. Data from this site will be used to train two pairs of algorithms. The first pair will be used to estimate SWE (mm h^{-1}) while the second pair estimate solid snow (cm h^{-1}). Furthermore, solid snowfall observations were once more taken during winter season of 2012 and 2013. The latter set of data will be used to verify the solid snowfall algorithms.

Figure (1.2) A collection of pictures showing an observation during Jan, 2012. The top left picture shows the table used in solid snowfall observation, the top right and bottom left pictures show collection of solid snowfall for measuring SWE, and the bottom right picture shows snow habit observation.

1.3.1.2 Pearson International Airport (CAN-NOW Project), Ontario

Pearson International Airport (CYYZ) near Toronto was selected due to the availability of multiple sensors for precipitation measurements as part of the CAN-Now project (Isaac et al. 2014). Also, the site is within a reasonable distance from the radar. Data from this site will be used to evaluate the new SWE algorithms.

A GEONOR T-200B precipitation gauge, fitted with a Nipher shield, and an FD12P sensor were chosen to obtain SWE (mm h^{-1}) at 1 min resolution as seen in Figure (1.3).

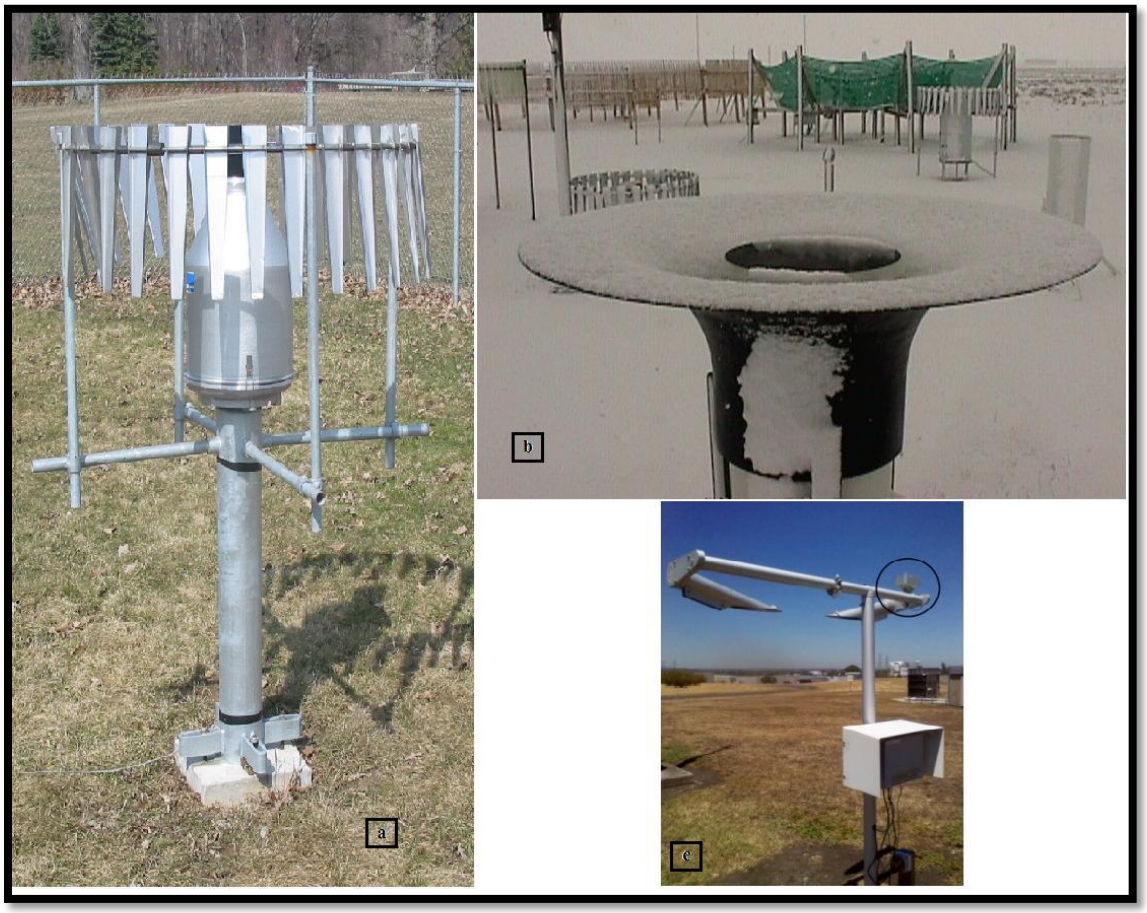

Figure(1.3) SWE measurements (a) GEONOR gauge in a standard shield, (b) GEONOR surrounded by a Nipher shield, (c) FD12P. The black circle in (c) indicates the SWE sensor named DRD12.

The GEONOR T-200B observations were corrected for winds using methods described by Goodison et al. (1998). Such an instrument provides year round measurements of solid and liquid precipitation intensity and accumulations through a

vibrating-wire weighing transducer (GEONOR 2008). To eliminate any instrument systematic errors, hourly accumulated SWE less than 0.2 mm were not used. Figure (1.4) shows GEONOR T-200B data (SWE mm h^{-1}) pre-and post-wind correction for snowfall events during the first three months of 2011.

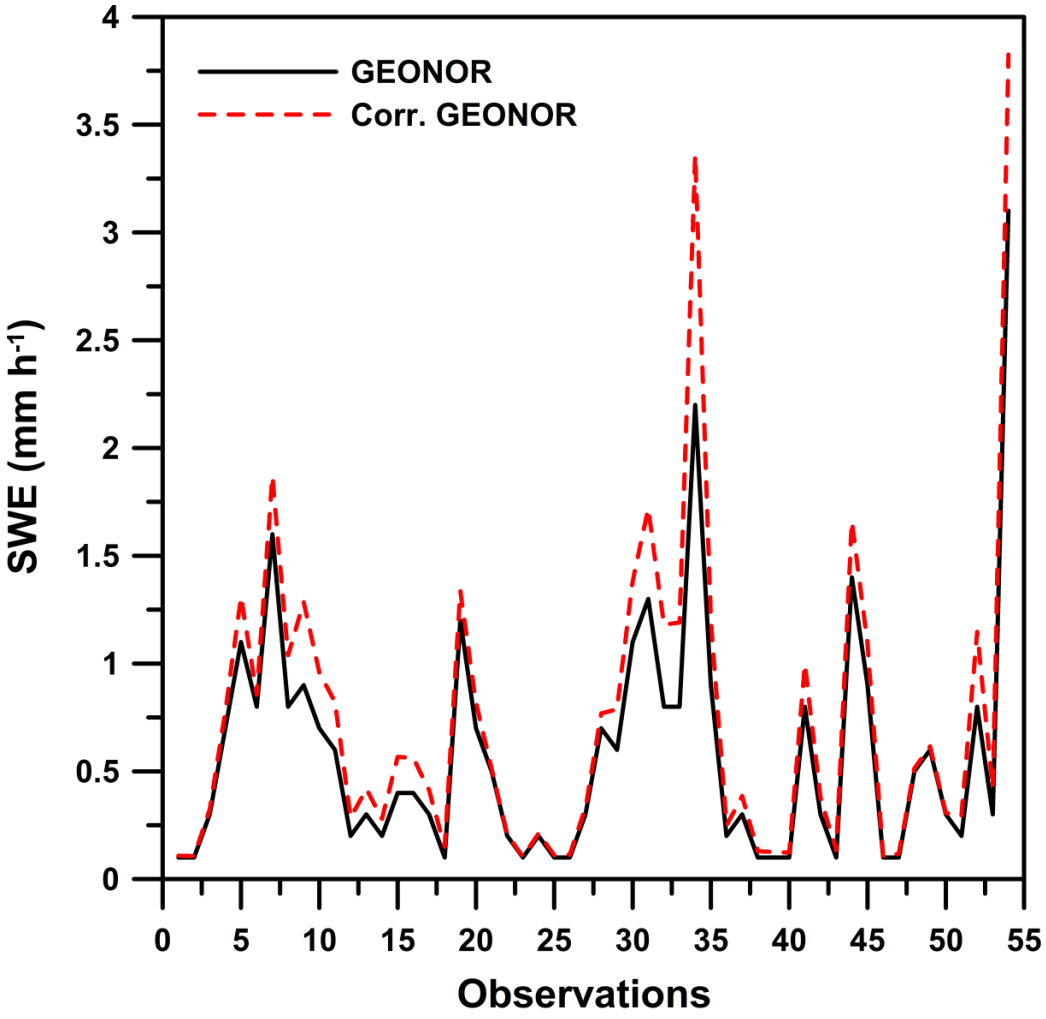

Figure (1.4) SWE (mm h^{-1}) before and after wind correction obtained from GEONOR T-200B fitted with Nipher shield at CYYZ. The x-axis represents 54 hourly observations for the period Jan-March, 2011.

The FD12P data were disregarded based on technical reasons mentioned in APPENDIX A, thus the GEONOR T-200B measurements at CYYZ are considered ground truth. It is worth noting that Oakville and CYYZ are approximately 56 km and 33 km from the CWKR radar, respectively. At an elevation angle of 0.2°, the radar POLPPI beam centerline is 480 m and 240 m AGL over Oakville and CYYZ, respectively. Figure (1.5) shows the geographical location of the two sites relative to the radar.

A third site, Toronto/Buttonville airport CYKZ, will be used in a support to a microphysical observation. Unfortunately, this site does not have any installed precipitation gauges to further compare to the different sites.

To establish polarimetric-based rainfall algorithms, further data from CYYZ will be collected using the same gauge and set up, but this time for rain events. Gauge data collected between May-Sept. of 2011 and 2012 will be used for this purpose as will be further discussed in chapter five.

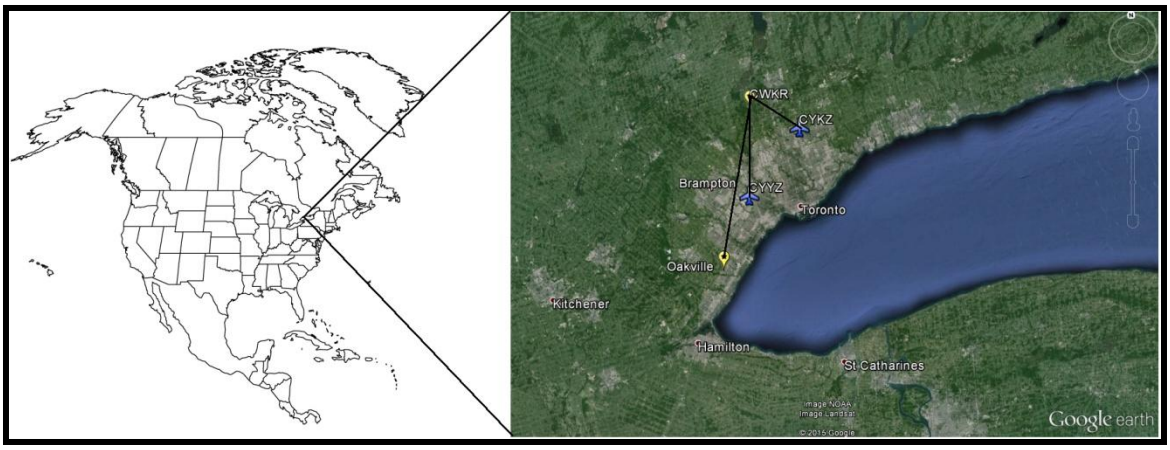

Figure (1.5) Geographical location of the three sites relative to King City (CWKR) radar (©2015 Google).

1.3.1.3 Mount Pearl, Newfoundland

Mount Pearl, NFLD, site is located about 33 km northeast of the only radar that covers the province. Figure (1.6) illustrates the geographical location of the radar and gauge site. SWE measurements were collected using a GEONOR T-200B placed in a single Alter shield at 1 min resolution. Gauge data were corrected for winds using a method mentioned in Theriault et al. 2012. Figure (1.7) shows the raw gauge data versus the corrected values. Due to its location, St. John's and surrounding areas, including Mt. Pearl, are considered windy during the passage of Nor'easters or regular winter storms. This figure shows the under catchment of the gauge and the role wind correction play in adjusting the SWE amounts. The corrected gauge data and the radar PPI CONVOL scan data at 1 km×1° resolution will be used to fit and evaluate SWE algorithms.

It should be noted that the two different wind correction methods applied here for CYYZ and Mount Pearl are due to the different shields used around each gauge.

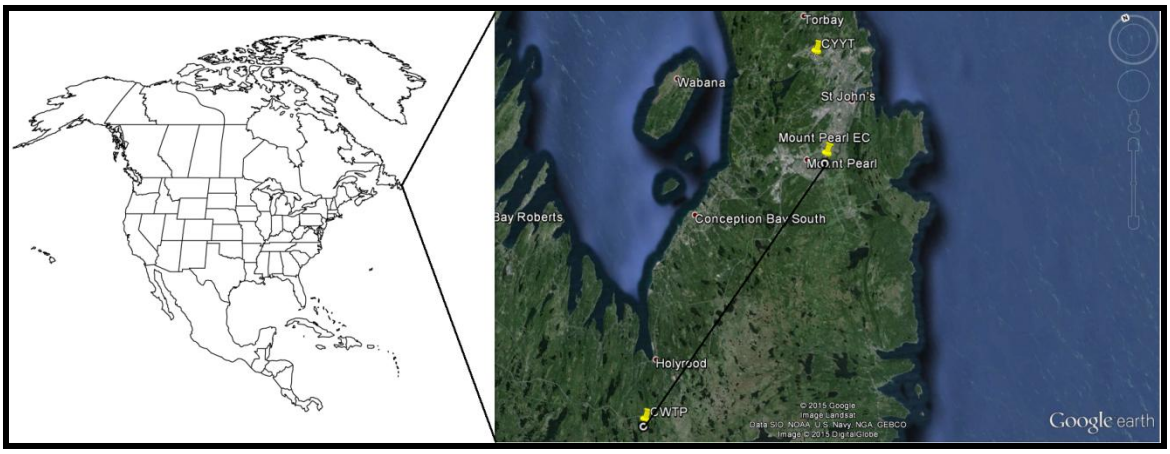

Figure (1.6) Geographical location of the Mount Pearl site relative to Holyrood (CWTP) radar (©2015 Google).

Snow is less dense than rain and has a lower fall speed. Thus, using short interval SWE accumulations in snowfall algorithms could produce different results than using longer interval accumulations. Therefore, the CYYZ and Mt. Pearl data SWE data will be calculated at 10 min and one hour intervals to study such differences. Meanwhile, the rainfall data will be calculated at 10 min interval only. It is worth noting that CYYZ and Mt. Pearl data quality control were handled in the same manner. For the hourly interval data, hourly accumulation below 0.2 mm was discarded. Meanwhile, any 10 min accumulation below 0.2 mm was discarded from the 10 min interval data set for each location.

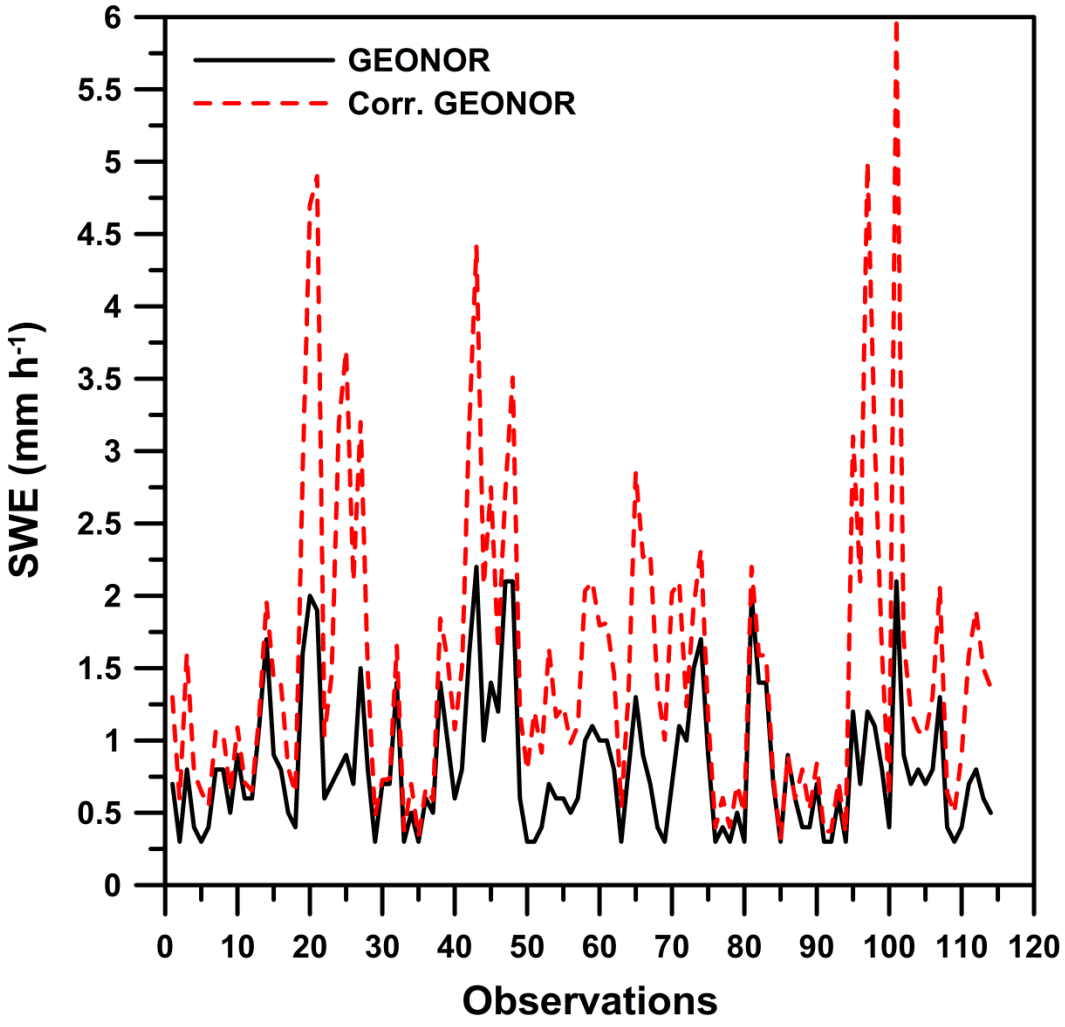

Figure (1.7) SWE (mm h^{-1}) before and after wind correction obtained from GEONOR T-200B with a standard wind shield provided with the gauge at Mt. Pearl. The x-axis represents 115 hourly observations for the period Jan-April, 2011 and Dec2011-Feb 2012.

Table 1.1 shows the number of SWE cases for each of the three sites for the hourly and 10 min intervals data in addition to the solid snowfall and rainfall cases. Unlike the climatological winter, the meteorological winter starts December 1st through End of February. It is commem for snowfall to continue into March or April in parts of Ontario. Precipitation at the Oakville site was visually monitored throughout each

observation to ensure eliminating any rain-snow mix of wet snow cases. For the CYYZ and Mt. Pearl sites, each observation was compared to the type of precipitation reported by the airoprt observer (METAR) to eliminate any type of mixed precipitation. The Oakville and CYYZ SWE data set were for the winter of 2011 (January-February-March) while Mt. Pearl SWE data set were for the winter of 2011 (January-February-March-April) and 2012 (December 2011 and January-February 2012). The combined data consist of all the hourly interval data from the three sites and will be used later in section 3.1.3. The solid snowfall cases are for the winter of 2011 (January-February-March), 2012 (January-February), and 2013 (December 2012 and January-February 2013).

To ensure that there was no mixed precipitation with the rain cases (radar beam above bright band), reported surface tempeatures (METAR) by the airport (CYYZ) must have been greater than 15°C. Since the radar beam centerline is less than 400 m AGL at that location, such a temperature threshold is sufficient to ensure all the scatterers within the radar sampled volume were in liquid form. The rainfall data set of 2011 and 2012 were collected between May and September. Although Table (1.1) shows 77 and 103 cases for the two years, the data used in the $R(Z_{eH}, Z_{DR})$ algorithms were 72 and 97 for 2011 and 2012, repsectively. The latter is due to the radar not reporting Z_{DR} values for a few occasions.

	Interval	Site	Winter	Number of cases
SWE	1 hr	Oakville	2011	24
		CYYZ	2011	38
		Mt. Pearl	2011	85
			2012	29
		Combined	2011-2012	176
	10 min	CYYZ	2011	69
		Mt. Pearl	2011	178
			2012	39
Solid Snowfall	1 hr	Oakville	2011	24
			2012	7
			2013	21
Rainfall	10 min	CYYZ	2011	77
			2012	103

Table (1.1) Total number of cases at different time intervals for the SWE, Solid snowfall, and rainfall events at each site. The combined includes the total of the three sites at 1 hour interval.

1.3.2 Radar Data

The King City C-band Doppler radar (CWKR) is located north of the City of Toronto, Ontario, Canada (43.96393° N, 79.57388° W) with an antenna diameter of 6.1 m and 0.62° beamwidth. The radar is designed to simultaneously transmit and separately receive horizontally and vertically polarized signals with two sampling strategies (Hudak et al. 2006), CONVOL and POLPPI to collect reflectivity (Z_{eH}), differential reflectivity (Z_{DR}), phase shift (φ_{DP}), specific differential phase shift (K_{DP}), and co-polar correlation coefficient (ρ_{hv}). Specifications of each of the above mentioned scan strategies can be summarized in Table (1.1). It is worth noting that CWKR uses a least squares fit method to calculate K_{DP} over a 6 km range. It is also worth noting that the radar is routinely calibrated every three to four months. The radar data used in this research are the output of the Unified Radar Processing (URP) software. This software produces basic conventional and velocity-based products.

The data chosen for this study are drawn from the POLPPI scan due to its higher spatial resolution at 0.2° elevation angle for solid snowfall cases and 0.5° elevation for rainfall cases. The radar spatial resolution is 0.5° x 0.25 km. For each volumetric scan, the radar products were averaged over different bin ranges (3×3, 5×5, 7×7, and 9×9). The two largest bin ranges were selected to study the effect averaging has on the radar parameters and also to account for particle advection. After further analysis, it was noted that there is a negligible difference in the values of Z_{eH}, and Z_{DR} among the different bin ranges while K_{DP} was unreliable in the larger bin ranges.

Task	CONVOL	POLPPI
Elevation angles	24 (0.3° to 24.7°)	0.2°
Samples	16	64
Rotation Rate	6 RPM	1 RPM
Range Resolution	250 m	125 m
Range Averaging	4 bins	2 bins
Azimuth resolution	1°	0.5°
Max Range	250 km	112 km

Table (1.2) Specifications of the King City radar dual polarized scanning strategies.

The Holyrood (CWTP) Doppler radar in NFLD is about 33 km from Mount Pearl site. The radar beam height is about (300 m) AGL from Mount Pearl. Since this radar is not upgraded with polarimetric capabilities, the PPI CONVOL scan was used at 1 km×1° spatial resolution and 0.5° elevation angle. Similar to CWKR data, different bin ranges showed minimal changes in Z_{eH} values.

CHAPTER TWO: Microphysical Analysis of Snowfall Events

Mono-polarized weather radars transmit signals in the horizontal plane while polarimetric radars transmit two orthogonal signals. The backscattered signal from a polarimetric pulse contains more information about the scatterers than a backscattered pulse from a horizontally polarized pulse. One of the important uses of dual polarized radars is distinguishing between rain and snow or finding the zero isotherms, i.e. bright band. Furthermore, various researches (Hogan et al. 2002, Ikeda et al. 2005, Anderic et al 2010, and Kennedy and Rutledge 2011) found that different polarimetric variables can be used to distinguish between pristine ice crystals and snow aggregates, distinguish between few types of pristine ice crystals, and assist in finding dendritic growth zones. This chapter contains observations of different polarimetric variables during snowfall event.

2.1 Co-Polar Correlation Coefficient (ρ_{hv})

Figure (2.1) shows the relationship between ρ_{hv} and Z_{eh} at three different locations: Oakville (56 km from the radar, azimuth 193°), Pearson International Airport, CYYZ, (33 km from radar, azimuth 185°), and Toronto/Buttonville Municipal Airport, CYKZ, (20 km from radar, azimuth 124°). Since temperature differences between the three sites are minimal due to the proximity of the three sites, it is possible that the noticeable difference seen in Figure (2.1 a-c) is due to decreasing signal-to-noise ratio (SNR), radar beam broadening, or both as the radar signals travel away from the radar. One more

potential factor in Figure (2.1 b) is non-uniform beam filling (NBF) due to the heavy ground clutter suppression in the CYYZ area. The other distinguishing feature in Figure (2.1) is that during heavy snowfall events, i.e. higher Z_{eh} (dBz) values, ρ_{hv} tends to reach close to unity. ρ_{hv} is independent of concentration, but depends on the scatterers diversity. Higher values of ρ_{hv} during heavy snowfall events are due to the higher concentration of certain types of scatterers within the sampled volume.

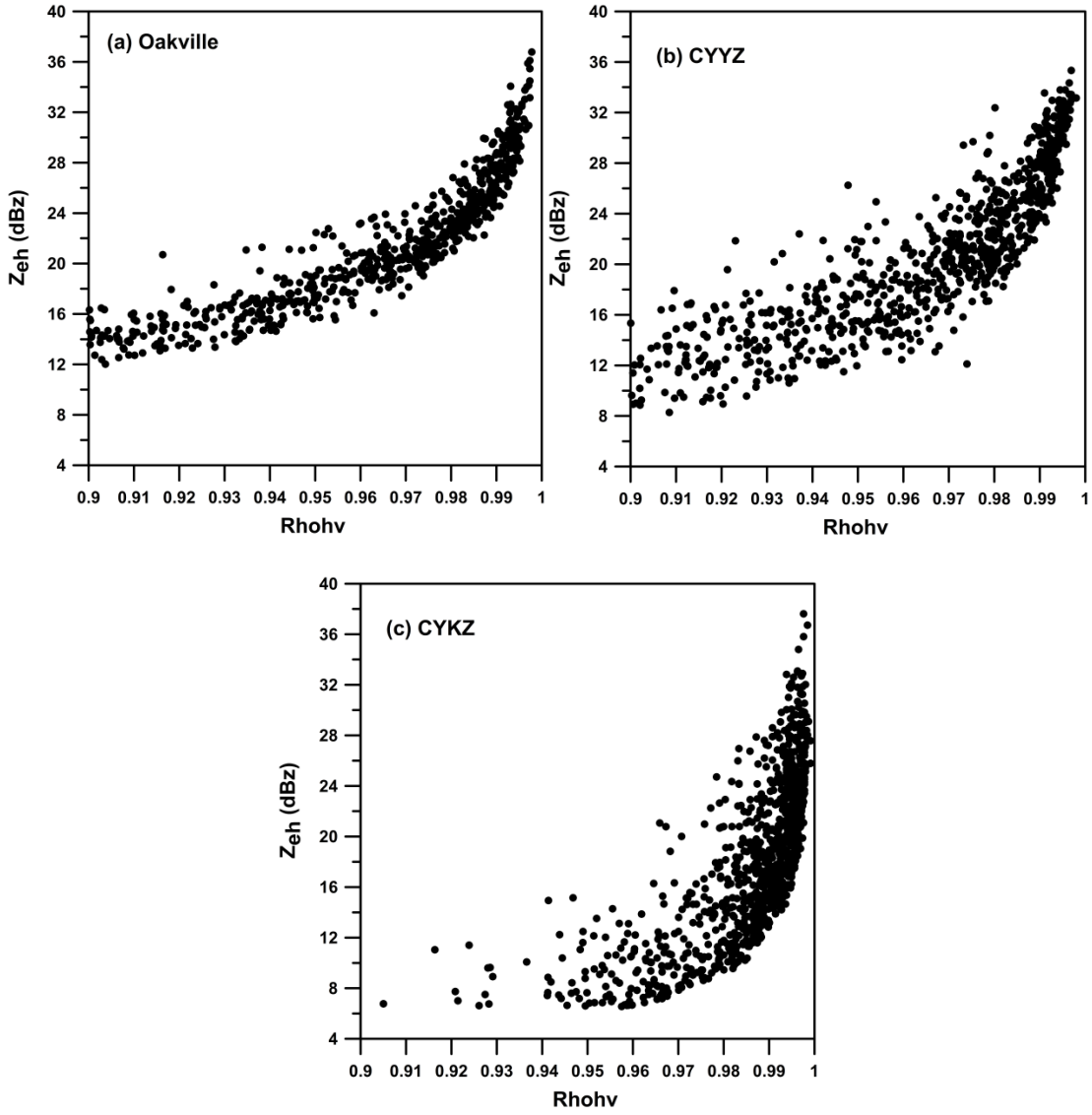

Figure (2.1) Horizontal reflectivity factor (dBz), versus co-polar correlation coefficient (ρ_{hv}) from (a) Oakville, (b) CYYZ, and (c) CYKZ for the period Jan-March, 2011.

The correlation coefficient, $\rho_{hv,}$ represents the coherency of the horizontally and vertically polarized electric fields within the radar sample, and in turn, it reaches unity during uniformly distributed hydrometeor sizes, shapes, orientation, and densities (Trapp et al. 2000). Furthermore, ρ_{hv} is sensitive to shape diversity (aspect ratio) of the scatterers, their canting angles and dielectric constant and/or backscattering differential phase (δ the difference between the two orthogonally polarized components of the backscattered wave once reflected from the scatterers) caused by the scatterers. At the S, C, and X radar bands the backscattering differential phase and dielectric constant diversity can be considered negligible. As snowflakes begin to aggregate, their effective density decreases which means that their shapes no longer matters. Thus, aggregates behave more like isotropic scatterers even when wobbling. Just like Z_{eh}, when the backscattering signal is dominated by such large size aggregates, the radar receiver senses very little variation of shapes or canting angles which leads to higher ρ_{hv} values. On the other hand, pristine ice crystals like dendrites or plates have non-spherical shapes with higher effective density compared to aggregates. Therefore, even with relatively little wobbling, such ice crystals tend to have lower ρ_{hv} values when illuminated by radar signal (private communication with M. R. Kumjian[1]).

On the possibility of using ρ_{hv} to improve rain drop size distribution estimates at C-band, Thurai et al (2008) found that a small decrease in ρ_{hv} can be attributed to broad particle size distributions, thus ρ_{hv} can be considered as a measure of the uniformity of

[1] Dr. Mathew Kumjian, Department of Meteorology, The Pennsylvania State University, 513 Walker Building, University Park, PA, 16801. E-mail: jumjian@psu.edu

the hydrometeor size distributions. Our Oakville observations suggest that ρ_{hv} could be sensitive to the size ranges of different snow habits within the radar sample volume. Table (2.1) shows that the larger the size differences of the hydrometeors within the sample volume, the larger the ρ_{hv} range. To further investigate this point, more ground observations within similar ranges from the radar are required.

Date	UTC	Snowfall (cm)	Size (cm)	ρ_{hv}	Crystal Types
Feb 27, 2011	0000-0100	1.5	0.1-0.3	0.985-0.965	Rimed, Columns, few Fernlike Steller Dendrite and Steller Dendrite, Irregular, aggregates of Columns.
	0100-0200	1.5	0.1-0.5	0.980-0.956	Rimed, Columns, Sheaths, Bullets (Isolated and Rosette), few small Steller Dendrites, Irregular
	0200-0300	1.0	0.15-1.7	0.982-0.944	Fernlike Steller Dendrite, aggregates of Fernlike Steller Dendrites
March 23, 2011	0910-1010	6.3	0.1-0.2	0.996-0.985	Bullet Rosette, Cups, Columns, Graupel, Rimed, Irreg.
	1010-1110	2.7	0.1-0.3	0.991-0.982	Graupel, Cups, Rimed, Bullet Rosette, few Steller Dendrite, Irreg.
	1500-1600	5.4	0.1-0.4	0.992-0.972	Columns, Needles, Crossed Needles, Rimed, Plates, Steller Dendrite, Irreg.
	1600-1700	3.2	0.1-0.2	0.995-0.988	Steller Dendrite, Rimed, Plates, Irreg.
	1800-1900	3.0	0.1-0.3	0.992-0.988	Rimed, Needles, Fernlike Steller Dendrite, Steller Dendrite, few Radiating Dendrite, Irregular
	1900-2000	3.5	0.1-0.2	0.996-0.992	Steller Dendrite, Rimed, Needles, few Fernlike Steller Dendrite, Irregular
	2000-2100	3.2	0.1-0.7	0.993-0.977	Fernlike Steller Dendrite, Steller Dendrite, Rimed, Irregular, aggregates of Fernlike Steller Dendrite and aggregates of Steller Dendrite

Table (2.1) Hourly snowfall amounts (cm), crystal types, solid hydrometeor size range (cm), and ρ_{hv} range from Oakville, Ontario. The term size refers to the longest axis of hydrometeor.

2.2 Differential Reflectivity (Z_{dr})

Figure (2.2) demonstrates the lack of correlation between Z_{eh} and Z_{dr}, but one can see that generally lower values of Z_{dr} are noticed at the higher Z_{eh} scale. This was attributed (e.g. William et al. 2011, Andric et al. 2010, and Ikeda et al. 2005) to the likely presence of large aggregated dry snowflakes. The Oakville data does show that at times when aggregates are observed their corresponding Z_{dr} tend to be slightly lower in value as seen in Table (2.2) (Feb 27, between 0000-0100 UTC and March 23, between 2000-2100 UTC). Meanwhile, in the same table higher Z_{dr} values were measured during the presence of large aggregates (up to 1.7 cm long). The solid snowfall accumulation was not high (1 cm) which is consistent with the lower values of reflectivity (20 to 24 dBz) throughout the six radar scans of that hour. Although more data are required to confirm these observations and our explanation, the higher values of Z_{dr} with the presence of large aggregates could be due to the Mie resonance effect, lower fluttering angles of the aggregates at that time, or the presence of an induced field transverse to the aggregates axis.

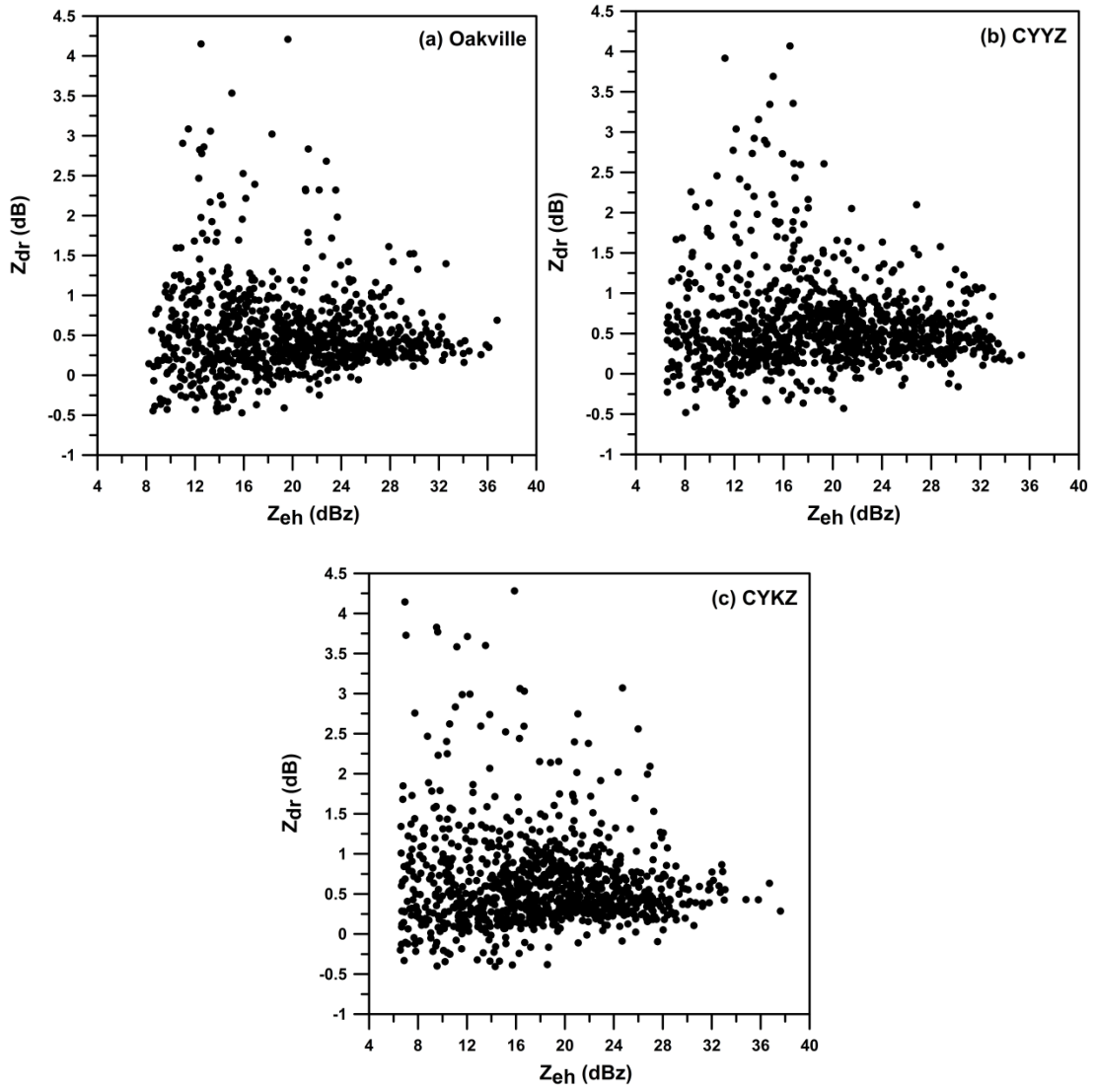

Figure 2.2 Differential reflectivity (dB), versus reflectivity factor (dBz), from (a) Oakville, (b) CYYZ, and (c) CYKZ for the period Jan-March 2011.

Date	UTC	Snowfall (cm)	Size (cm)	Z_{dr} (dB)	Crystal Types
Feb 27, 2011	0000-0100	1.5	0.1-0.3	0.20-0.54	Rimed, Columns, few Fernlike Steller Dendrite and Steller Dendrite, Irregular, *aggregates* of Columns.
	0100-0200	1.5	0.1-0.5	0.18-0.54	Rimed, Columns, Sheaths, Bullets (Isolated and Rosette), few small Steller Dendrites, Irregular
	0200-0300	1.0	0.15-1.7	0.84-2.32	Fernlike Steller Dendrite, *aggregates* of Fernlike Steller Dendrites
March 23, 2011	0910-1010	6.3	0.1-0.2	0.27-0.38	Bullet Rosette, Cups, Columns, Graupel, Rimed, Irreg.
	1010-1110	2.7	0.1-0.3	0.21-0.59	Graupel, Cups, Rimed, Bullet Rosette, few Steller Dendrite, Irreg.
	1500-1600	5.4	0.1-0.4	0.13-0.85	Columns, Needles, Crossed Needles, Rimed, Plates, Steller Dendrite, Irreg.
	1600-1700	3.2	0.1-0.2	0.42-0.52	Steller Dendrite, Rimed, Plates, Irreg.
	1800-1900	3.0	0.1-0.3	0.38-0.75	Rimed, Needles, Fernlike Steller Dendrite, Steller Dendrite, few Radiating Dendrite, Irregular
	1900-2000	3.5	0.1-0.2	0.37-0.55	Steller Dendrite, Rimed, Needles, few Fernlike Steller Dendrite, Irregular
	2000-2100	3.2	0.1-0.7	0.26-0.46	Fernlike Steller Dendrite, Steller Dendrite, Rimed, Irregular, *aggregates* of Fernlike Steller Dendrite and *aggregates* of Steller Dendrite

Table 2.2 Hourly snowfall amounts (cm), crystal types, solid hydrometeor size range (cm), and Z_{dr} (dB) range from Oakville, Ontario. The term size refers to the longest axis of hydrometeor.

2.3 Specific Differential Phase Shift (K_{DP})

One of the advantages of polarimetric radars is better rainfall estimation through the use of K_{DP}-based rainfall algorithms (Chandrasekar et al. 1990; Aydin et al. 1995; Gorgucci and Scarchilli 1997). Unfortunately, the same cannot be said for estimating snowfall rates. Figure (2.3a-c) shows the low sensitivity of K_{DP} during snowfall events. This can be attributed to the fact that K_{DP} is sensitive to the liquid water content within the sampled volume. Both Oakville and CYKZ sites shows similar results while a wider spread in K_{DP} values is noticed at CYYZ. K_{DP} values tend to be noisy. The noise level increases at the lower reflectivity factor values due to the strong ground clutter present in CYYZ.

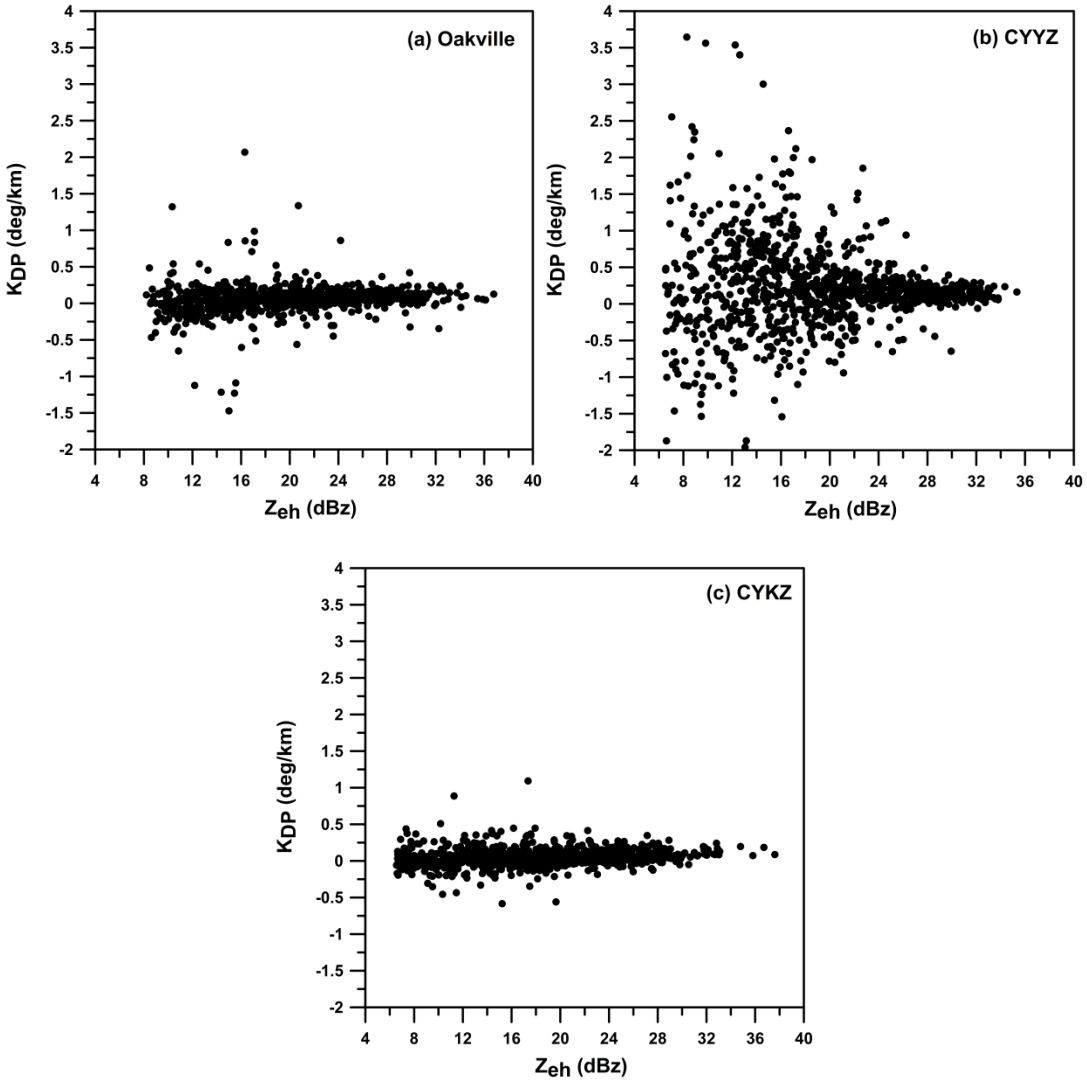

Figure (2.3) Specific differential phase shift (°/km), versus reflectivity factor (dBz), from (a) Oakville, (b) CYYZ, (c) CYKZ for the period Jan-March 2011.

CHAPTER THREE: Radar Quantitative Precipitation Estimation (QPE)

3.1 Introduction

Improvements in quantitative precipitation estimation depend on two main factors, radar measurement quality and ground precipitation measurements. The finer the measurements scale, the better precipitation rates can be estimated which in turn enables meteorologists to fine-tune the forecast and issue necessary warnings.

Although, there are radars that are capable of producing a complete scan in less than 5 minutes, the Canadian Radar Network scan strategy is designed to produce conventional and Doppler cycles every 10 minutes (Joe and Lapczak, 2002).

The GEONOR T-200B used in this study is capable of producing SWE measurements at 1 minute intervals. Unlike rainfall, measuring SWE at such a short time interval would produce a greater margin of error due to the smaller number of frozen particles collected by the gauge. In other words, during light or even moderate snowfall measurements, depending on crystal types, 1-minute SWE measurements by the gauge are very small and they are close to the gauge accuracy measurement.

The SWE measurements from the GEONOR T-200B located at CYYZ (CAN-NOW Project) and Mount Pearl, NFLD, are both at one minute intervals. Since the radar data are only available at 10 minutes interval, SWE accumulations were measured at 10 minute intervals. To show the effects of SWE measurements at longer time intervals,

SWE data were also computed at one hour intervals. Accordingly, two pairs of SWE algorithms are calculated from each gauge using 10 min and one hour radar SWE accumulation, respectively. To eliminate any measurement errors by the gauge, similar thresholds (SWE $\geq$ 0.2 mm) were used for the 1 hr and the 10 min gauge accumulations.

Since the CWKR radar is upgraded with polarimetric capabilities, the CYYZ and Oakville algorithms consist of a conventional $S(Z_{eH})$ and polarimetric $S(Z_{eH}, Z_{DR})$ algorithms, while Mount Pearl can only give $S(Z_{eH})$ as the CWTP radar does not have polarimetric capabilities. The Oakville data set was manually measured at one hour interval; consequently, only hourly algorithms are available. The coefficients of the Oakville algorithm will be compared to their counterparts from CYYZ and Mount Pearl. It is worth noting that 10 minute radar data are used throughout the process of developing the algorithms.

The iteration process to find the coefficients of all the algorithms in this study was based on minimizing the sum of square difference between the estimated and observed SWE. A software package within Microsoft Office Excel was used for this purpose. The Microsoft Office Excel Solver tool is part of a suite of commands sometimes called "what-if-analysis" tools that use several algorithms to find optimal value for a formula in an objective cell subject to constraints or limits, on the values of other formula cells on a worksheet. The Solver works with a group of cells called variable cells that participate in computing the formulas in the objective and constraint cells by adjusting the values in the variable cells to satisfy the limits on constraint cells, Solver produces the result for the objective cell. The Generalized Reduced Gradient (GRG) Nonlinear solving method for

nonlinear optimization uses a code developed by Leon Lasdon, University of Texas at Austin, and Alan Waren, Cleveland State University, and enhanced by Frontline Systems, Inc. (Frontline Systems, Inc. 2015). This method deals with active inequalities. The inequality constraints are transformed to equality constraints using a linear slack variable of the type used in linear programming problems.

Errors from each algorithm were analyzed in terms of correlation coefficient, mean bias (MB) in (mm h^{-1}), normalized mean bias (NMB %), mean absolute error (MAE) in (mm h^{-1}), root mean square error (RMSE) in (mm h^{-1}), normalized mean absolute error (NMAE %), and the mean as defined below:

$$Correlation\ Coefficient = r = \frac{\sum_{i=1}^{n}(E_i - \bar{E})(O_i - \bar{O})}{\sqrt{\sum_{i=1}^{n}(E_i - \bar{E})^2 \sum_{i=1}^{n}(O_i - \bar{O})^2}} \tag{3.1}$$

$$Mean\ Bias = \frac{1}{n}\sum_{i=1}^{n}(E_i - O_i) \tag{3.2}$$

$$NMB\ (\%) = \frac{\sum_{i=1}^{n}(E_i - O_i)}{\sum_{i=1}^{n} O_i} \times 100\% \tag{3.3}$$

$$MAE = \frac{1}{n}\sum_{i=1}^{n}|E_i - O_i| \tag{3.4}$$

$$RMSE = \sqrt{\frac{1}{n}\sum_{i=1}^{n}(E_i - O_i)^2} \tag{3.5}$$

$$NMAE\ (\%) = \frac{\sum_{i=1}^{n}|E_i - O_i|}{\sum_{i=1}^{n} O_i} \times 100\% \tag{3.6}$$

$$Mean = \frac{\sum_{i=1}^{n} E_i}{n} \tag{3.7}$$

where E_i is the estimated value from the algorithm, O_i is the observed value, n is the number of observations, $\bar{E}$ and $\bar{O}$ are the mean of the estimated and observed precipitation rate, respectively.

3.1.1 Algorithms Using Hourly SWE Measurements

In this section five algorithms will be presented, including two pairs of conventional and polarimetric algorithms from Oakville and CYYZ and a single algorithm from Mount Pearl. As mentioned in section 1.2.3, the power-law form will be used here.

The Oakville algorithms:

$$S(Z_{eH}) = 0.0124 \times Z_{eH}^{0.749} \tag{3.8}$$

$$S(Z_{eH}, Z_{DR}) = 0.0106 \times Z_{eH}^{0.765} \times Z_{DR}^{0.525} \tag{3.9}$$

The CYYZ algorithms:

$$S(Z_{eH}) = 0.0593 \times Z_{eH}^{0.500} \tag{3.10}$$

$$S(Z_{eH}, Z_{DR}) = 0.0209 \times Z_{eH}^{0.609} \times Z_{DR}^{3.24} \tag{3.11}$$

The Mt. Pearl algorithm:

$$S(Z_{eH}) = 0.0302 \times Z_{eH}^{0.617} \tag{3.12}$$

where S is in (mm h^{-1}), Z_{eH} in (mm^6 m^{-3}), and $Z_{DR} = 10^{(Z_{dr}/10)}$.

The variation between the coefficients in each of the above algorithms can be attributed to the differences in the method of snowfall measurements, the wind correction method, nature of precipitation, and ground clutter affecting the radar beam. Although a GEONOR T-200B gauge is installed at both CYYZ and Mt. Pearl sites, the shield used around each gauge orifice is different which could lead to some variation in snow collection.

Figure (3.1) show the fits for the conventional $S(Z_{eH})$ algorithm. The main noticeable feature in this figure is that the relationship between SWE and reflectivity factor is nonlinear. Departure from linearity is dependent on snowfall rate and presumably crystal type. For instance, in Figure (3.1a) SWE values can range between 0.12 to 2.4 mm h^{-1} for reflectivities less than 500 mm^6 m^{-3} (< 27 dBz). A similar observation can be made looking at Figure (3.1b) at the higher range of Z_{eH} and also in Figure (3.1c) for $Z_{eH} \leq 2200$ mm^6 m^{-3} ($\leq$ 33 dBz). Such a spread in SWE measurements within the smaller range of Z_{eH} indicates the possible role crystal types (and their densities) play in SWE measurements. The horizontal wind component affecting falling precipitation can also play a role in displacing the precipitation observed by the radar further away from ground measurement location. The presence of aggregates of dendrites within the radar sample produces higher values of the reflectivity factor, but not necessary higher SWE values since their density is very low.

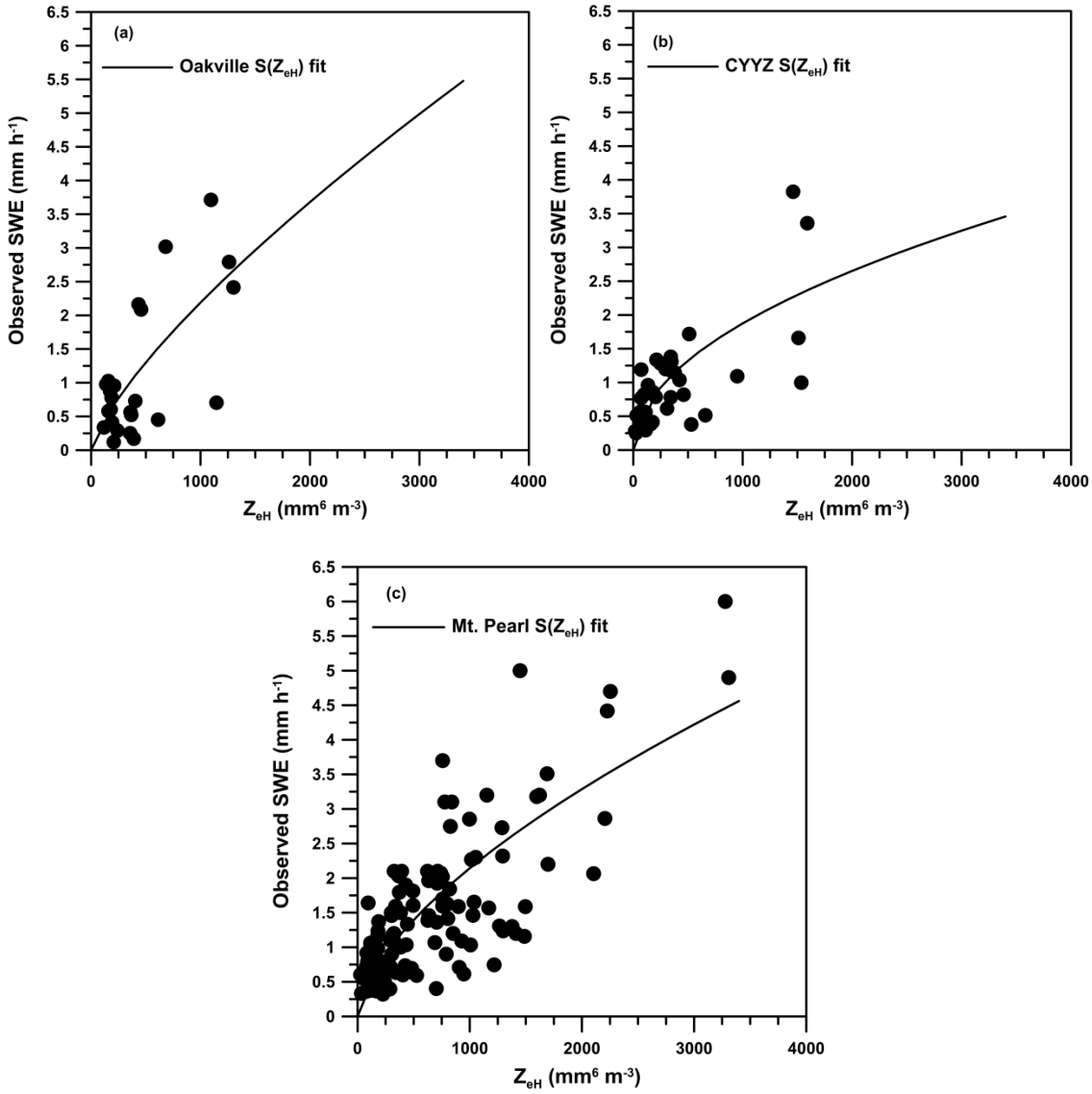

Figure (3.1) Observed SWE(mm h^{-1}) versus radar reflectivity (mm^6 m^{-3}) and the fits representing Eqs. 3.8, 3.10, and 3.12, respectively, at the three sites.

To present the contribution of Z_{DR} in the algorithms, Figure (3.2) shows the SWE estimation from $S(Z_{eH})$ and $S(Z_{eH}, Z_{DR})$ in addition to the ones from the current CWKR algorithm. A very subtle difference is noticed between $S(Z_{eH})$ and $S(Z_{eH}, Z_{DR})$ with the largest difference seen for the CYYZ location, Figure (3.2b). The latter can be mainly attributed to the ground clutter suppression applied to CYYZ and nearby area; also the different SWE measurements between the two locations can play a role in creating such a difference. The understated role Z_{DR} plays in SWE measurements does not negate its importance in mixed precipitation events (Andric et al. 2013; Trapp et al. 2001). This study supports other studies (Andric et al. 2013; Trapp et al. 2001) in that smaller values of Z_{DR} are noticed for snow aggregates while higher values can be noticed in the presence of only pristine crystals and which maybe present during very low snowfall rates that hardly produce any accumulation on ground. Furthermore, Figure (3.2) shows that SWE underestimation by the current CWKR algorithm increases with increasing snowfall rates. Similar results can be noticed from the Mt. Pearl site (not shown).

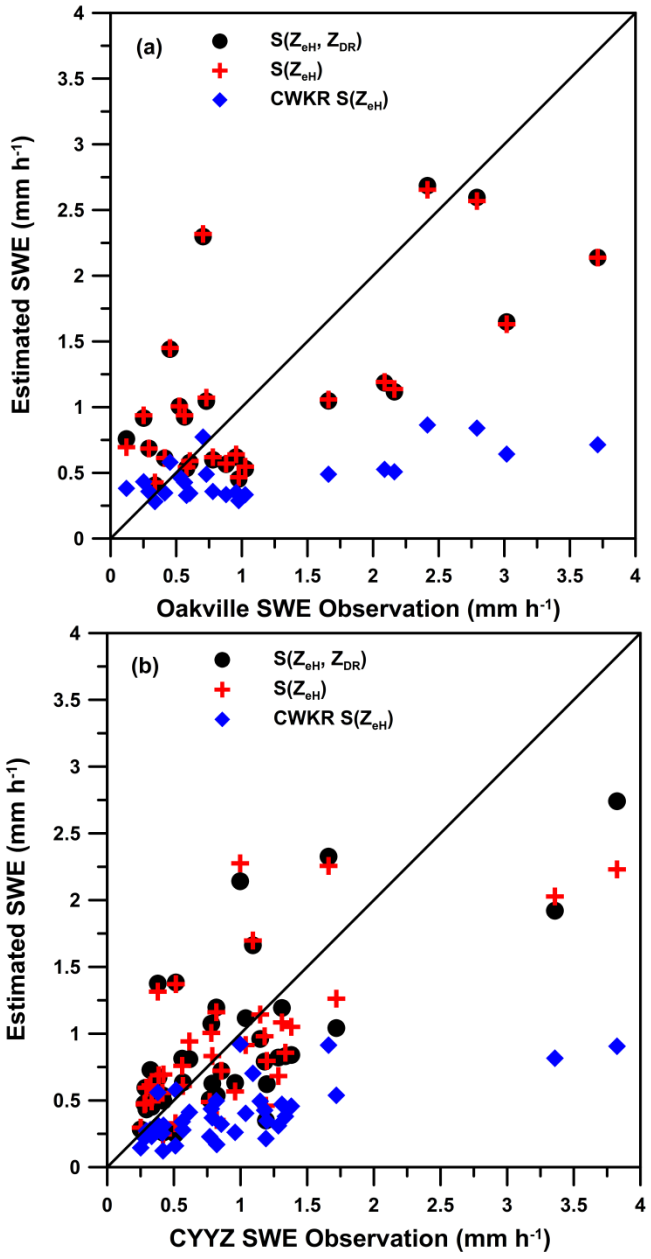

Figure (3.2) Estimated SWE (mm h^{-1}) from $S(Z_{eH}, Z_{DR})$, $S(Z_{eH})$, and CWKR $S(Z_{eH})$ at 1 hr interval using Oakville and CYYZ data and algorithms, respectively.

Table (3.1) shows the statistical scores of each of the algorithms. SWE estimation using the current Canadian Radar Network algorithm is also presented, and labelled “Radar”. It is worth noting that despite the underestimation of the current radar algorithm, its correlation coefficient is high. In statistics, the Pearson product-moment correlation coefficient is a measure of the linear correlation between two variables. The current radar SWE algorithm estimates ($S = 0.034 \times Z_{eH}^{0.452}$) hardly reach close to 1 mm h^{-1}.

	Oakville $S(Z_{eH})$/Radar	**CYYZ $S(Z_{eH})$/Radar**	**Mount Pearl $S(Z_{eH})$/Radar**	**Oakville $S(Z_{eH}, Z_{DR})$**	**CYYZ $S(Z_{eH}, Z_{DR})$**
Cor. Coeff.	0.670/0.668	0.681/0.677	0.757/0.745	0.670	0.705
NB (mm h^{-1})	-0.002/-0.628	-0.020/-0.547	-0.023/-0.96	-0.006	-0.032
NMB %	-0. 176/-56.8	-2.10/-57.6	-1.53/-62.8	-0.559	-3.36
MAE (mm h^{-1})	0.576/0.713	0.407/0.560	0.543/0.96	0.578	0.411
RMSE (mm h^{-1})	0.735/1.09	0.545/0.83	0.708/1.33	0.734	0.530
NMAE %	52.0/64.5	42.8/59.0	35.6/63.2	52.2	43.3
Est. Mean	1.10/0.478	0.929/0.402	1.50/0.567	1.10	0.917
Obs. Mean	1.11	0.949	1.53	1.11	0.949

Table (3.1) Statistical scores for all the algorithms for 1 hr interval gauge data. Observations per location: Oakville (24), CYYZ (38), and Mt. Pearl (114).

The visual inspection of the $S(Z_{eH})$ estimates from the three different sites shows that the algorithms are relatively close in range in estimating SWE up to $Z_{eh} \leq 30$ dBz (1000 mm^6 m^{-3}). The main factors that can play a role in SWE disparity beyond that point are ground clutter, gauge errors, crystal types, the wind correction method used, and finally the shields used around the gauge orifice. The area around CYYZ is heavily corrected for ground clutter due to the presence of high-rise buildings. This can be noticed at times when precipitation is present but no echo is found on radar output. Although both radar and gauge data have gone through automatic and manual inspection, there is still a room for error. Crystal types and crystal aggregation can affect SWE measurement due to their different densities, fall speed, and slanted displacement as they fall. The Oakville site was the only location where crystal types were observed, but no wind correction method used on the data. The gauge at CYYZ had a Nipher shield while the one at Mt. Pearl was surrounded by a standard protective housing supplied by the company (GEONOR 2008).

For hydrological purposes, Table (3.2) shows total SWE estimated compared to gauge accumulations. The underestimation of the current radar algorithm persists throughout the three different locations. Although the algorithms over or underestimate SWE on the hourly bases at times, the total estimation over a long period, i.e. seasonal, shows promise for hydrological application. The advantage of such algorithms is in their superior areal coverage despite gauge distribution and also during gauge mechanical or power failure challenges.

	Oakville $S(Z_{eH})$/Radar	**CYYZ $S(Z_{eH})$/Radar**	**Mount Pearl $S(Z_{eH})$/Radar**	**Oakville $S(Z_{eH}, Z_{DR})$**	**CYYZ $S(Z_{eH}, Z_{DR})$**
Total Gauge (mm)	26.5	36.1	174	26.5	36.1
Total Algo. Est. (mm)	26.5/11.46	35.3/15.29	171/64.6	26.4	34.9
Under Est. %	-0.176/-56.8	-2.10/-57.6	-1.53/-62.8	-0.559	-3.36

Table (3.2) Total gauge accumulation versus total algorithms estimation using 1 hr interval gauge data. Observations per location: Oakville (24), CYYZ (38), and Mt. Pearl (114).

3.1.2 Algorithms Using 10 min Interval SWE Measurements

Higher temporal resolution data are desirable in depicting real time events. The reason behind using 10 min SWE measurements is to understand and show the effect that higher resolution precipitation data has on the algorithm coefficients. Note that it is easier to measure light rainfall rates than measuring snowfall rates at similar intensities. Usually, light snowfall rates consist of low density crystals, which may not be sensed by the gauge when measuring SWE at shorter time interval, e.g. seconds or minutes. In addition, because of the slow fall speeds of snow crystals, the precipitation rate at the ground is not highly correlated with reflectivity aloft on short time scales, especially when the rates are varying in time. But the real time user usually interprets what the radar is seeing aloft with what is happening at the ground on the radar display (updated at times less than 10 minutes) so it is important to examine this issue.

The main differences between this section and the previous one is that SWE gauge data are used at 10 min intervals for CYYZ and Mt. Pearl sites. The Oakville data set is not included in this section as they were measured manually at 1 hour interval.

The CYYZ algorithms based on 10 min precipitation rate data can be given as:

$$S(Z_{eH}) = 0.237 \times Z_{eH}^{0.294} \tag{3.13}$$

$$S(Z_{eH}, Z_{DR}) = 0.242 \times Z_{eH}^{0.324} \times Z_{DR}^{1.13} \tag{3.14}$$

And the Mt. Pearl Algorithm is given as:

$$S(Z_{eH}) = 0.335 \times Z_{eH}^{0.328} \tag{3.15}$$

where S is in (mm h^{-1}), Z_{eH} in (mm^6 m^{-3}), and $Z_{DR} = 10^{(Z_{dr}/10)}$.

Figure (3.3) Shows the fit of $S(Z_{eH})$ for CYYZ and Mt. Pearl using 10 minute gauge data while Figure (3.4) shows the scatter plot of $S(Z_{eH})$, $S(Z_{eH}, Z_{DR})$, and CWKR algorithms against gauge data (10 min intervals).

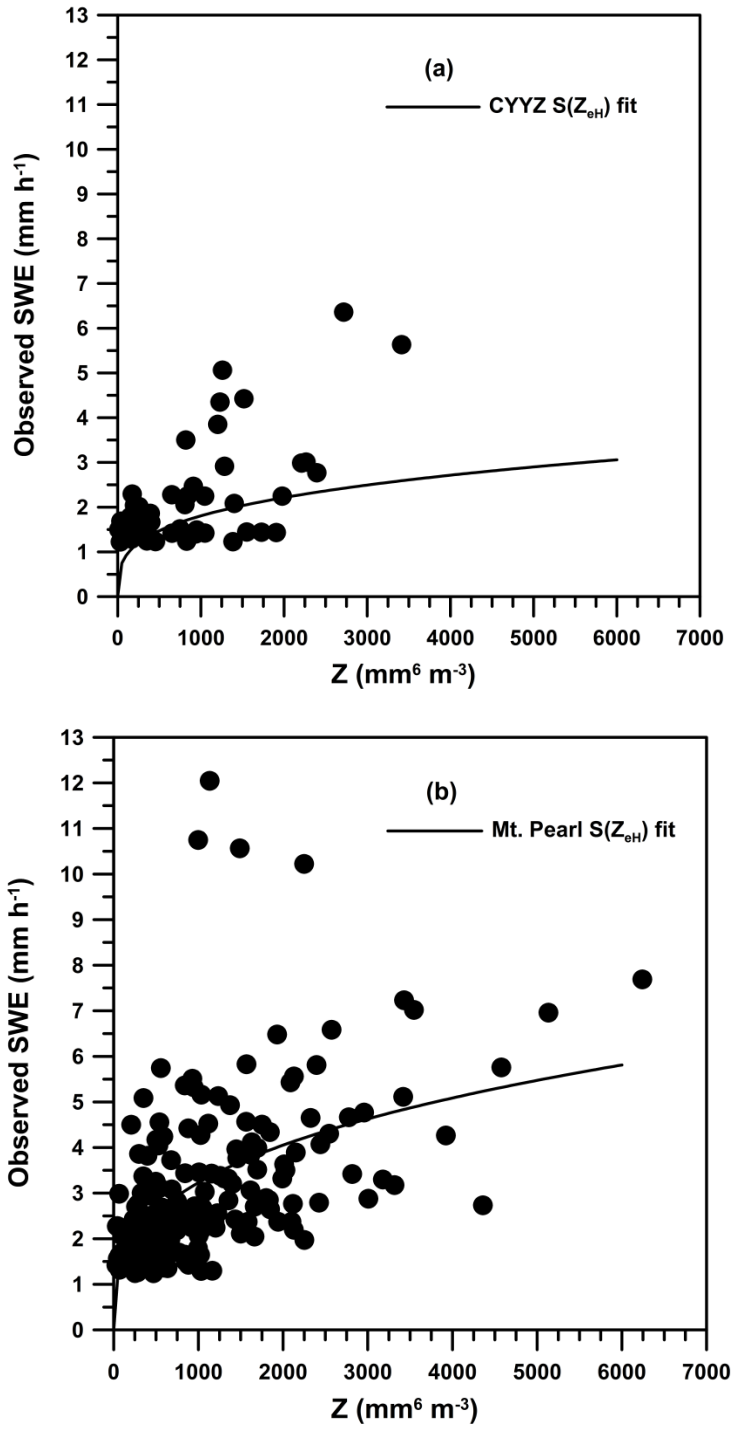

Figure (3.3) Fitted curves to 10 minutes interval gauge data set from (a) CYYZ and (b) Mt. Pearl NFLD.

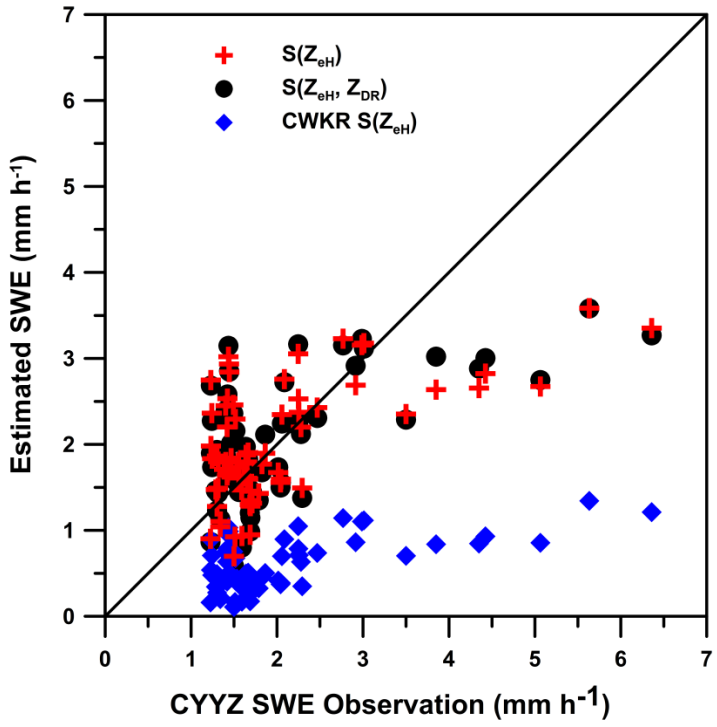

Figure 3.4 Scatter plot observes SWE at 10 min interval from CYYZ against $S(Z_{eH})$, $S(Z_{eH}, Z_{DR})$, and CWKR algorithms.

Comparing Figures (3.1) with (3.3), (noting the different scales) with respect to location, shows that the 10 minute SWE interval data includes higher values of both reflectivity and SWE, and also amplifies the scatter there is at the lower scale of measured SWE and reflectivity. It also shows that although the 10 minute data add more data points, the majority of the observed SWE data points lie at the lower end of the reflectivity scale. Although no observations of crystal types exist at both locations, this suggests the presence of dense smaller in size snow habits during such observations. Such scatter creates a noticeable difference between the algorithms' coefficients. Also, comparing Figures (3.2 b) and (3.4) shows no added skills to the algorithm when higher time resolution gauge data are used. A consistent observation is that the current CWKR

algorithm underestimates SWE (mm h^{-1}) by ~ 55 to 75%. It is important to mention that the x-axis scaling difference between Figures (3.1) and (3.3) is due to averaging Z_{eH} values over one hour in Figure (3.1) while using the calculated 10 min values by the radar in Figure (3.2). Also, one may notice that the data points in Figures (3.3) and (3.4) are not exactly sixfold the number of points in Figures (3.1) and (3.2), respectively. This is due to the fact that within the hour the radar often measures reflectivity (in the lower range), but the frozen hydrometeors have very light density and the gauge is not able to record precipitation within a 10 min interval. Thus, such points were disregarded from the data set. It is worth noting that the four highest observed SWE (mm h^{-1}) at Mt. Pearl in Figure (3.3 b) are observations that were observed during very high wind events (> 9 m s^{-1}) which is almost close to blizzard conditions as per Environment Canada threshold criteria (Blizzard warnings are issued when winds of 40 km or greater are expected). The wind correction method would force corrected gauge values to higher amounts due to severe gauge under catchment.

Table (3.3) below shows the statistical scores of the three algorithms obtained using 10 min interval gauge data. $S(Z_{eH})$ and $S(Z_{eH}, Z_{DR})$ from CYYZ confirm the subtle contribution Z_{DR} makes at times. Once more, although there is a geographical difference between CYYZ and Mt. Pearl, the statistical scores show slight differences between the two $S(Z_{eH})$ algorithms with the more pronounced difference seen in RMSE. This is due to the fact that Mt. Pearl data set is bigger and has more scatter than the CYYZ data set.

	CYYZ $S(Z_{eH})$/Radar	Mount Pearl $S(Z_{eH})$/Radar	CYYZ $S(Z_{eH}, Z_{DR})$
Cor. Coeff.	0.587/0.614	0.533/0.538	0.599
NB (mm h^{-1})	-0.021/-1.45	-0.010/-2.27	-0.026
NMB %	-1.04/-71.6	-0.344/-76.5	-1.30
MAE (mm h^{-1})	0.605/1.45	0.936/2.27	0.601
RMSE (mm h^{-1})	0.851/1.70	1.44/2.76	0.843
NMAE %	30.0/71.6	31.5/76.5	29.8
Est. Mean	2.00/0.573	2.96/0.699	1.99
Obs. Mean	2.02	2.97	2.02

Table (3.3) Statistical scores for all the algorithms used at 10 min interval gauge data. Observations per location: CYYZ (69) and Mt. Pearl (217)

Table (3.4) shows the total over-or-underestimation of each algorithm when compared to gauge totals. It is clear that there is a minimal difference between the conventional and polarimetric algorithms from CYYZ.

	CYYZ $S(Z_{eH})$/Radar	**Mount Pearl $S(Z_{eH})$/Radar**	**CYYZ $S(Z_{eH}, Z_{DR})$**
Total Gauge (mm)	139	645	139
Total Algo./Radar Est. (mm)	138/39.5	642/151.7	138
Under-Over Est. %	-1.04/-71.6	-0.344/-76.5	-1.30

Table (3.4) Total gauge accumulation versus total algorithms estimation (10 min interval) for the period Jan. to April of 2011 and Dec. 2011 to Feb. 2012. Observations per location: CYYZ (69) and Mt. Pearl (217).

Although the Mt. Pearl algorithm data set comprise of more points (217 observations) in comparison to CYYZ (69 observations), their statistical scores are comparable. The variation between their statistical scores, the 10 min versus 1 hr algorithms, is expected to be amplified later in the verification section (3.2.2).

3.1.3 Algorithms Using Combined Data Set at One Hour interval SWE Measurements

In this section all the data sets are combined together to produce a larger sample to derive the coefficients of the different algorithms. Frist, the 1 hr interval data sets from Oakville, CYYZ, and Mt. Pearl were combined into one data set to derive the coefficient from $S(Z_{eH})$ algorithm which can be written as:

$$S(Z_{eH}) = 0.0295 \times Z_{eH}^{0.618} \tag{3.16}$$

The Oakville and CYYZ data sets were combined into a single data set to derive coefficients of the $S(Z_{eH}, Z_{DR})$ algorithms as:

$$S(Z_{eH}, Z_{DR}) = 0.0220 \times Z_{eH}^{0.632} \times Z_{DR}^{1.58} \tag{3.17}$$

where S is in (mm h^{-1}), Z_{eH} in (mm^6 m^{-3}), and $Z_{DR} = 10^{(Z_{dr}/10)}$.

Figure (3.5 a) shows the fit of the $S(Z_{eH})$ algorithm while Figure (3.5 b) shows the $S(Z_{eH}, Z_{DR})$ algorithm fitted 1:1 to the observations. Tables (3.5) and (3.6) show the statistical scores of the fitted data with their total estimation, respectively. Comparing Tables (3.1) to (3.5) and (3.2) to (3.6) show similar results for $S(Z_{eH})$ and $S(Z_{eH}, Z_{DR})$. Statistically, the $S(Z_{eH})$ produced from the combined data set seems to lie closer to the Mt. Pearl algorithm as evident in Tables (3.5) and (3.6) (also more evident in a later Figure (3.8)); also the coefficients of Equations (3.12) and (3.16) are very close to each other. Meanwhile, Equation (3.17) lies between Equations (3.9) and (3.11). Such results are encouraging as they show the three data sets are not different from each other, their only difference is in the size and range of data in each set.

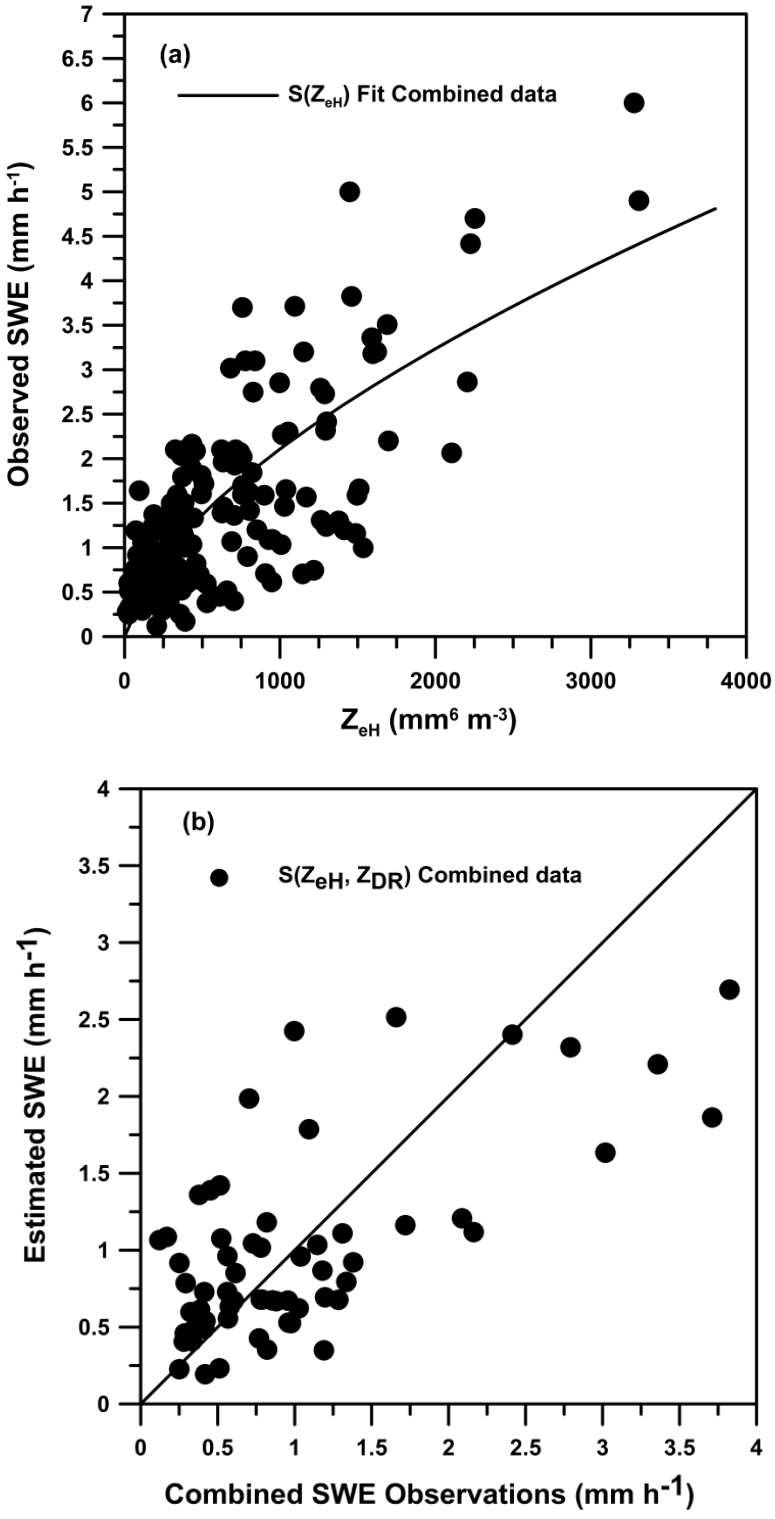

Figure (3.5) Fitting the combined hourly data. (a) $S(Z_{eH})$ fitting using combined data from Oakville, CYYZ, and Mt. Pearl and (b) is fitting $S(Z_{eH}, Z_{DR})$ using combined data from Oakville and CYYZ.

	$S(Z_{eH})$	$S(Z_{eH}, Z_{DR})$
Cor. Coeff.	0.751	0.673
NB (mm h^{-1})	-0.0228	-0.0238
NMB %	-1. 69	-2.36
MAE (mm h^{-1})	0.521	0.481
RMSE (mm h^{-1})	0.685	0.631
NMAE %	38.8	47.7
Est. Mean	1.23	0.986
Obs. Mean	1.34	1.01

Table (3.5) Statistical scores of the algorithms developed using the combined data set for the period Dec-March of 2011 and 2012. The combined data set consist of (176) observations for the $S(Z_{eH})$ and (62) observations for the $S(Z_{eH}, Z_{DR})$.

	$S(Z_{eH})$	$S(Z_{eH}, Z_{DR})$
Total Gauge (mm)	236	62.6
Total Algo. Est. (mm)	232	61.1
Under-Over Est.%	-1.69	-2.36

Table (3.6) Total SWE accumulation from gauges and observations compared to algorithms total estimation developed using combined data set for the period Dec-March 2011 and 2012. The combined data set consists of (176) observations for the $S(Z_{eH})$ and (62) observations for the $S(Z_{eH}, Z_{DR})$.

3.2 Algorithms Verification and Statistical Scores

All the previously mentioned algorithms are set to be verified using the same data, but from different sites, e.g. the Oakville conventional algorithms (obtained using 1 hr and 10 min interval) will be verified using CYYZ and Mt. Pearl observations. The algorithms obtained using 1 hr interval gauge data will be verified first then followed by the ones developed using 10 min interval gauge data.

3.2.1 Verification of One Hour Interval Algorithms

All the algorithms found from one site will be verified using data from other sites. The algorithms containing Z_{DR} are not going to be verified in Mt. Pearl as the CWTP radar is not equipped with polarimetric capabilities.

Figure (3.6 a-b) still displays the humble contribution of the polarimetric variable, Z_{DR}, makes when added to the algorithm. Equation (3.12) seems to estimate SWE slightly higher than Equation (3.10) as seen in figure (3.6 a) while Figure (3.6 b) shows that Equation (3.12) estimate SWE slightly lower than Equation (3.8).

It is worth noting that in Figure (3.6 b) all the algorithms tend to overestimates SWE by 1 to 2 mm h^{-1} in few points (SWE estimation ~1.5-3 mm h^{-1} with SWE observation ~0.5-1.5 mm h^{-1}). CYYZ METAR data for these data showed high sustained winds (10 to 13 KT) gusting (15 to 32 KT). Solid snow accumulations for these events ranged between (1 to 4 cm h^{-1}) as reported by the airport observer while their corresponding SWE accumulations were ranged between (0.4 to 1.7 mm h^{-1}), respectively. Possibly, the higher gusts lowered the catchment efficiency that even the wind correction method was not able to fully account for the total SWE.

Finally, Figure (3.6 c) shows that during heavier snowfall rates Equation (3.10) tends to underestimate SWE when compared to Equation (3.8). Such differences between the algorithms can be attributed to the methods of measuring snow on ground, ground clutter affecting radar measurements, and or the horizontal wind/fall velocity affecting frozen hydrometeor displacements creating mismatch between what the radar and the gauge are sampling.

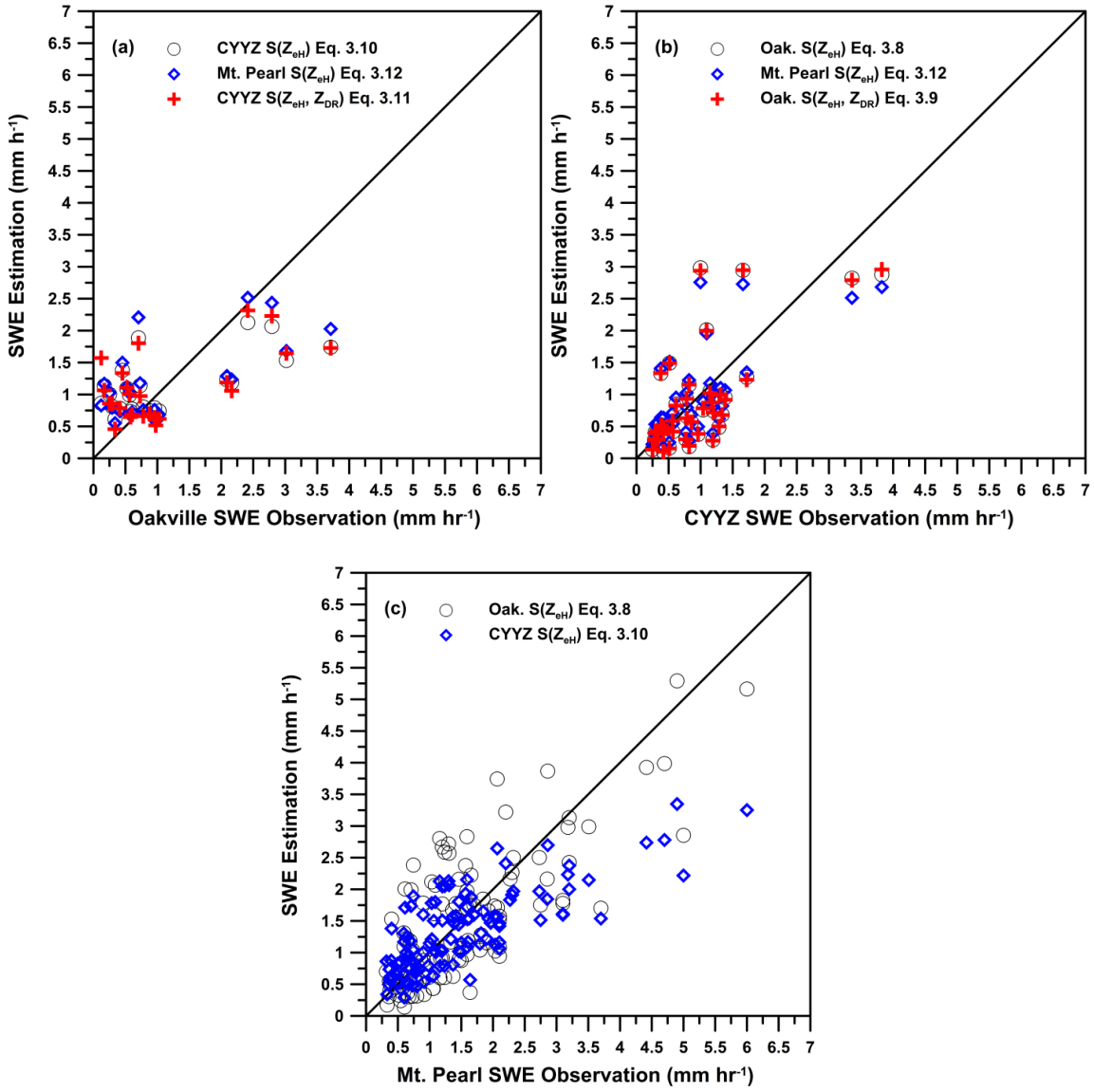

Figure (3.6) Gauge observation versus algorithm estimation for each site (a) Oakville, (b) CYYZ, and (c) Mt. Pearl.

The statistical differences between all the algorithms, Equations (3.8-3.12), are presented in Table (3.7). Generally, this table highlights the small differences between the algorithms. The biggest difference is seen in NMB which basically shows how much over or under estimation each algorithm estimates normalized by the observations. This point is reflected clearly in Table (3.8) where the total estimation of each algorithm is given. Equation (3.8) seems to be performing well when verified in both sites (CYYZ and Mt. Pearl) subjectively speaking, while the $S(Z_{eH}, Z_{DR})$, Equation (3.11), from CYYZ performs the best when verified using the Oakville data.

	Eq. 3.8 in CYYZ	Eq. 3.8 in Mt. Pearl	Eq. 3.10 in Oakville	Eq. 3.10 in Mt. Pearl	Eq. 3.12 in Oakville	Eq. 3.12 in CYYZ	Eq. 3.9 in CYYZ	Eq. 3.11 in Oakville
Cor. Coeff.	0.700	0.763	0.669	0.749	0.669	0.692	0.705	0.605
MB (mm h^{-1})	-0.0520	-0.0230	0.0100	-0.173	0.0679	0.0150	-0.0560	-0.00814
NMB %	-5.46	-1.50	0.860	-11.3	6.14	1.54	-5.95	-0.736
MAE (mm h^{-1})	0.435	0.558	0.613	0.550	0.589	0.418	0.435	0.622
RMSE (mm h^{-1})	0.602	0.729	0.768	0.758	0.743	0.569	0.597	0.792
NMAE %	45.8	36.6	55.4	36.1	53.2	44.0	45.9	56.3
Est. Mean	0.897	1.50	1.12	1.35	1.17	0.964	0.893	1.10
Obs. Mean	0.949	1.53	1.11	1.53	1.11	0.949	0.949	1.11

Table (3.7) Statistical scores of the verified algorithms. Algorithms obtained using hourly SWE data from each location were verified using data from other sites. Eq. 3.8 $S(Z_{eH})$ developed for Oakville, Eq. 3.9 $S(Z_{eH}, Z_{DR})$ developed for Oakville, Eq. 3.10 $S(Z_{eH})$ developed for CYYZ, Eq. 3.11 $S(Z_{eH}, Z_{DR})$ developed for CYYZ, and Eq. 3.12 $S(Z_{eH})$ developed for Mt. Pearl. Observations per location: Oakville (24), CYYZ (38), and Mt. Pearl (114).

	Eq. 3.8 in CYYZ	Eq. 3.8 in Mt. Pearl	Eq. 3.10 in Oakville	Eq. 3.10 in Mt. Pearl	Eq. 3.12 in Oakville	Eq. 3.12 in CYYZ	Eq. 3.9 in CYYZ	Eq. 3.11 in Oakville
Total Gauge (mm)	36.1	174	26.5	174	26.5	36.1	36.1	26.5
Total Algo. Est. (mm)	34.1	171	26.8	154	28.2	36.6	33.9	26.3
Under-Over Est. Algo %	-5.46	-1.50	0.860	-11.3	6.14	1.54	-5.95	-0.736

Table (3.8) Total gauge accumulation versus total algorithms estimation. Eq. 3.8 $S(Z_{eH})$ developed for Oakville, Eq. 3.9 $S(Z_{eH}, Z_{DR})$ developed for Oakville, Eq. 3.10 $S(Z_{eH})$ developed for CYYZ, Eq. 3.11 $S(Z_{eH}, Z_{DR})$ developed for CYYZ, and Eq. 3.12 $S(Z_{eH})$ developed for Mt. Pearl. Observations per location: Oakville (24), CYYZ (38), and Mt. Pearl (114).

3.2.2 Verification of 10 min Interval Algorithms

Verification in the section will be carried out as in the previous section while using the algorithms obtained with 10 min interval gauge data, Equations (3.13 through 3.15). The three algorithms are from CYYZ and Mt. Pearl. Ideally, such algorithms are verified using 10 min interval SWE observations from CYYZ and Mt. Pearl data sets. The above algorithms were applied to the hourly Oakville data set to verify them. In this case, the radar values were in 10 min interval while gauge values were in hourly (six consecutive radar values were used in each algorithm then the estimated SWE values were summed to produce an hourly estimate that corresponds to the hourly gauge value).

Figure (3.7 a) shows the three algorithms overestimating SWE (mm h^{-1}) at the lower end of snowfall rates with Equation (3.15), Mt. Pearl algorithm, showing the higher overestimation. Meanwhile, the polarimetric algorithm, Equation (3.14), still shows a small difference when compared to the conventional one, Equation (3.13). Figure 3.7 (b) confirms the overestimation by Equation (3.15) at the lower snowfall rates when verified using 10 min interval gauge data from CYYZ. Although Equation (3.13) demonstrates a slight improvement in SWE estimation at lower snowfall rates, it, nevertheless, showing greater underestimation, especially at higher SWE range. This is further amplified in Tables (3.9) and (3.10) as the majority of the statistical scores show larger errors (lower skills) when compared to Tables (3.7) and (3.8). Almost all the algorithms are showing overestimation of total SWE as seen in Table (3.10).

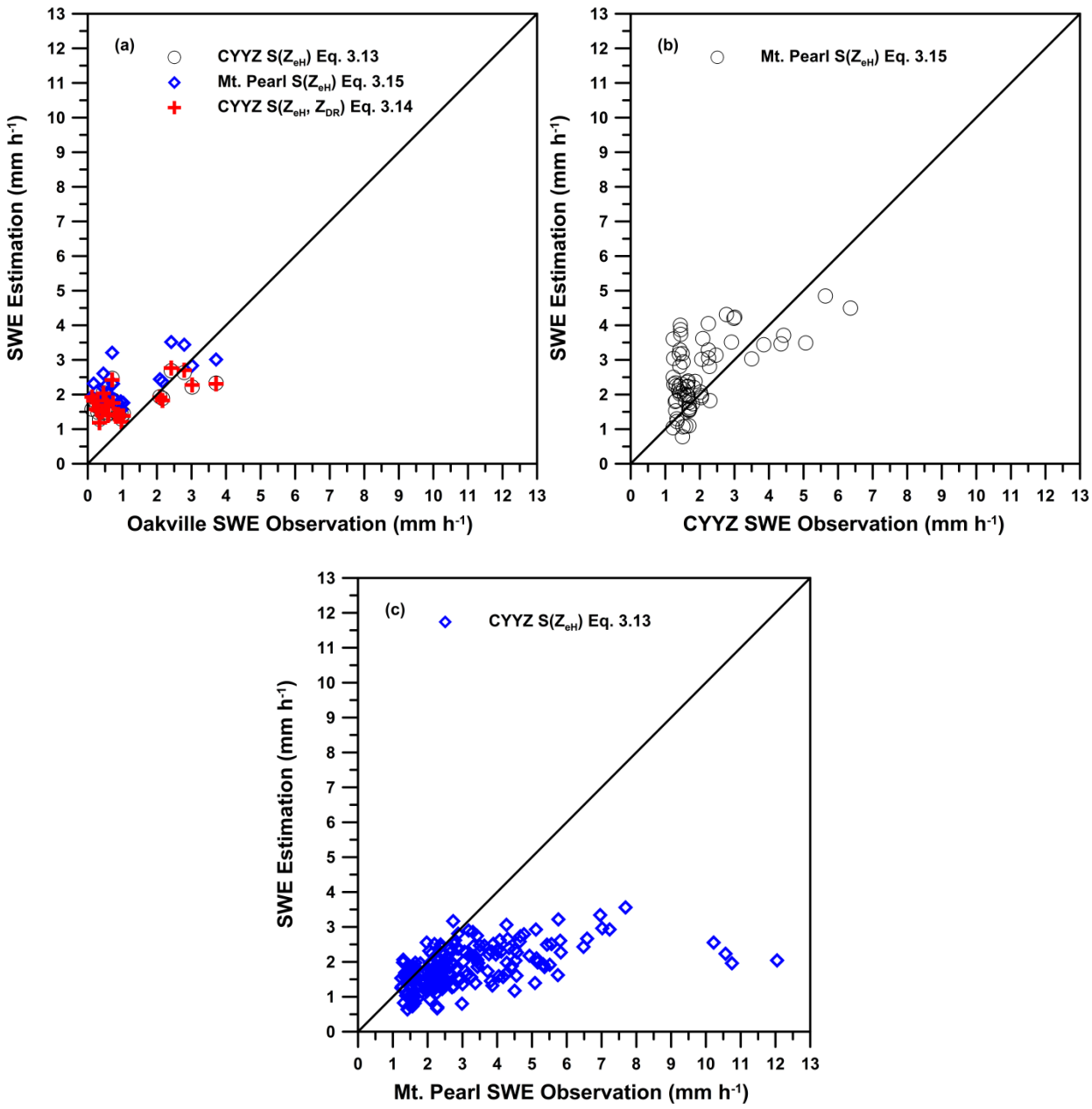

Figure (3.7) Gauge observation versus 10 min algorithms estimation for the three sites (a) 1 hour SWE observations, (b) CYYZ 10 min SWE observations, and (c) Mt. Pearl 10 min SWE observations.

	Eq. 3.13 in Oakville	Eq. 3.15 in Oakville	Eq. 3.13 in Mt. Pearl	Eq. 3.15 in CYYZ	Eq. 3.14 in Oakville
Cor. Coeff.	0.667	0.667	0.531	0.593	0.630
MB (mm h^{-1})	0.682	1.13	-0.681	0.524	0.675
NMB %	61.7	102	-22.9	26.0	61.0
MAE (mm h^{-1})	0.913	1.21	0.968	0.828	0.903
RMSE (mm h^{-1})	1.04	1.35	1.62	1.05	1.04
NMAE %	82.5	109	32.6	41.0	81.6
Est. Mean	1.79	2.24	0.160	2.54	1.78
Obs. Mean	1.11	1.11	2.97	2.02	1.11

Table (3.9) Statistical scores of the verified (10 min) interval algorithms. Algorithms obtained using hourly SWE data from each location were verified using data from other sites. Eq. 3.13 $S(Z_{eH})$ developed for CYYZ, Eq. 3.14 $S(Z_{eH}, Z_{DR})$ developed for CYYZ, and Eq. 3.15 $S(Z_{eH})$ developed for Mt. Pearl. Observations per location: Oakville (24), CYYZ (69), and Mt. Pearl (217).

	Eq. 3.13 in Oakville	Eq. 3.15 in Oakville	Eq. 3.13 in Mt. Pearl	Eq. 3.15 in CYYZ	Eq. 3.14 in Oakville
Total Gauge (mm)	26.5	26.5	645	139	26.5
Total Algo. Est. (mm)	42.9	53.8	497	175	42.7
Under-Over Est. %	61.7	103	-22.9	25.9	61.0

Table (3.10) Total gauge accumulation versus total algorithms estimation. Eq. 3.13 $S(Z_{eH})$ developed for CYYZ, Eq. 3.14 $S(Z_{eH}, Z_{DR})$ developed for CYYZ, and Eq. 3.15 $S(Z_{eH})$ developed for Mt. Pearl. Observations per location: Oakville (24), CYYZ (69), and Mt. Pearl (217).

Tables (3.7) through to (3.10) characterise the differences between the algorithms developed using gauge data at 1 hr interval and gauge data at 10 min interval. For instance, the $S(Z_{eH})$ developed using the CYYZ data set at 1 hour and 10 min intervals, Equations (3.10) and (3.13), while being verified using the Oakville data set shows better skills at the 1 hour interval, Equation (3.10) in Oakville, with MB=0.0100, NMB=0.860%, and NMAE=55.4% while the 10 min interval algorithm, Equation (3.13) in Oakville, scores are MB=0.682, NMB=61.7%, and NMAE=82.5%. The total underestimation of Equation (3.10) is 0.860% while Equation (3.13) overestimates SWE by 61.7%. Similar results can be seen when comparing the same algorithms verified at Mt. Pearl, Equations (3.10) and (3.13) in Mt. Pearl. Similarly, the $S(Z_{eH})$ developed using Mt. Pearl data set at 1 hour and 10 min interval shows similar trends when verified with Oakville and CYYZ data set, Equations (3.12) and (3.15) in Oakville, (3.12) and (3.15) in CYYZ. The same thing can be said for the $S(Z_{eH}, Z_{DR})$ algorithms developed using CYYZ when verified with Oakville data set, Equations (3.11) and (3.14) in Oakville. Thus, it is more suitable to use the algorithms developed using 1 hour gauge interval as they show superior results. The longer accumulation time reduced errors arising from high winds, lower snowfall rates, or less dense crystal types that show higher reflectivities but measure very little in the gauge.

Although the coefficients of 1 hr interval $S(Z_{eH})$ algorithms vary from one another, Equations (3.8), (3.10), and (3.12), their SWE estimation is still close at low-to-moderate reflectivity factors, i.e. $Z_{eH} \leq 30$ dBz with their differences increasing at higher reflectivity; and this can be clearly seen in Figure (3.8). It is clear that the three algorithms are close in their SWE estimates at around $26 \leq Z_{eH} \leq 28$ dBz (400 to 600 $mm^6\ m^{-3}$). At lower reflectivities, Equation (3.8) tends to estimate SWE ($mm\ h^{-1}$) slightly lower than Equations (3.10) and (3.12), while higher estimation by Equation (3.8) can be seen at higher estimates at higher reflectivities; in

both cases Equation (3.12) tend to lie in between both Equations (3.8) and (3.10) with it being closer to Equation (3.10) when Z_{eH} < 26 dBz and gets closer to Equation (3.8) beyond that threshold. When combining the Oakville, CYYZ, and Mt. Pearl 1 hour interval gauge data to develop a single S(Z_{eH}) algorithm, Equation (3.16), it appears that the algorithm follows closely to Equation (3.12) developed in Mt. Pearl. This is a further proof that the differences in the geographical location do not yield very different algorithms, at least in the weak to moderate precipitation rates.

The threshold applied on gauge-measured SWE was (SWE≥0.2 mm h^{-1}) in the 1 hr interval data and (SWE≥1.2 m h^{-1}) in the 10 min interval data. The thresholds were applied to eliminate any gauge error readings. Such thresholds would differentiate both data sets in such that the 10 min interval data set would contain less data points at the lower end of the precipitation rate. Thus, it is clear from Figure (3.8) that both 10 min interval algorithms tend to overestimate SWE at the low to moderate precipitation rates when compared to rest of the algorithms.

The Finish Meteorological Institute (FMI) operates a C-band Doppler radar and uses an empirical equation to determine the most likely water phase for each radar measurement bin. Upon detection of snow, the radar uses a specific S(Z_{eH}) algorithm ($SWE = 0.1 \times Z_{eH}^{0.5}$) that was adjusted from Sekhon and Srivastava (1970) based on gauge comparisons in 2005 (Saltikoff et al. 2010). Huang et al. (2010) presented several algorithms developed at CARE site in Ontario using a 2D video distrometer (2DVD) and the CWKR radar. Among a total of seven algorithms they developed, one algorithm ($SWE = 0.0345 \times Z_{eH}^{0.6329}$) scored very well when compared to the double-fence international reference (DFIR) gauge located near Egbert, Ontario. Since both algorithms were developed using C-band radar, such algorithms can be further compared to the

ones developed in this study. In general, both algorithms tend to overestimate SWE. A logical explanation for such overestimation, assuming all other measurements are error free, is that their data sets comprise of multiple hours of denser snowfall events and/or their data sets include more observations at higher SWE values.

The box and whisker plot in Figure (3.8) consistently shows a greater spread at the higher observed SWE than at the lower end as seen when comparing the upper and lower whiskers. Also, this spread increases with increasing reflectivity. Among other factors, differences in temperature and humidity play a major role in the formation of different snow habits. The reflectivity factor is mainly affected by the type and concentration of the snow habits within the radar volumetric sample. In other words, the presence of a certain type and concentration of snow crystals, or their aggregates, within the sampled volume could produce the same reflectivity factor as other types of snow crystals; but the major difference is that both sampled volumes will give different SWE, and possibly solid, accumulation on ground.

Furthermore, the box and whisker plot in Figure (3.8) shows that as Z_{eH} increases and the algorithms diverge in estimating SWE, Equations (3.12) and (3.16) are persistently lying within the median observed SWE. Since Equation (3.16) was developed using the entire three data sets, it is considered the best representative of the entire observed SWE and can be recommended for adoption by EC.

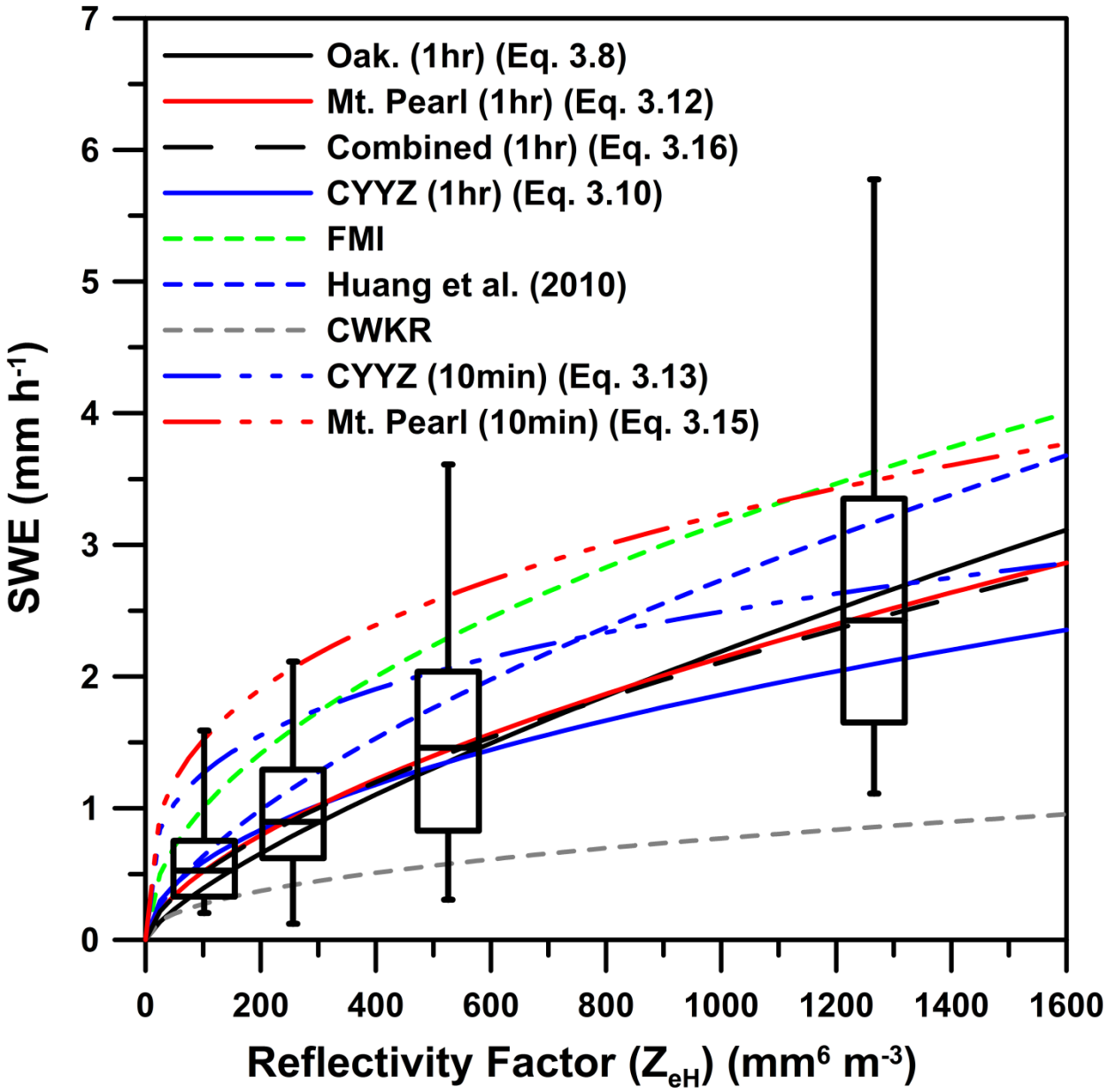

Figure (3.8) $S(Z_{eH})$ SWE estimation versus reflectivity factor (Z_{eH}) in ($mm^6\ m^{-3}$) using the 1hr interval, the combined data set, the 10 min interval, FMI, Huang et al. (2010), and the current CWKR algorithms. The box plots represent the 25%, 50% and 75% of the observed data while the whiskers represent the extremes.

CHAPTER FOUR: Solid Snowfall Estimation

4.1 Introduction

Estimating SWE is very important to meteorologists and hydrologists. In addition to SWE, solid snowfall rates are considered as valuable for on duty meteorologists issuing alerts for specific regions. In the Rayleigh scattering regime the radar back scattering cross-section of ice particles is a function of the particles mass, which can be expressed as a melted particle diameter, irrespective of their shapes. The particle shape becomes important at the shorter wavelengths (higher frequency) where the received power depends upon the particle shape.

In this section hourly snowfall data from Oakville taken between Jan-March of 2011 will be used to produce two algorithms, $S(Z_{eH})$ and $S(Z_{eH}, Z_{DR})$. The latter algorithms will be verified using hourly data from the same site conducted during winter 2012 and 2013.

4.2 Solid Snowfall Algorithms Using Hourly Snowfall Observations

Boucher and Wieler (1985) found encouraging results relating radar reflectivity to solid snowfall rate using an X-band radar in Sudbury, Massachusetts, USA. Although the CWKR radar has a longer wavelength (C-band) than the one used by Boucher and Wieler, it is possible to use the solid snowfall data from Oakville collected during winter 2011 to produce a pair of algorithms [$S(Z_{eH})$ and $S(Z_{eH}, Z_{DR})$] that directly relate reflectivity factor to solid snowfall rates (cm h^{-1}). Since the Oakville data set is at 1 hour intervals, there will be no 10 min interval algorithms. The algorithms will be verified using hourly solid snowfall rates collected in Oakville during winters 2012 and 2013.

The algorithms estimating solid snowfall rates can be given as:

$$S(Z_{eH}) = 0.0338 \times Z_{eH}^{0.681} \quad (4.1)$$

$$S(Z_{eH}, Z_{DR}) = 0.0551 \times Z_{eH}^{0.655} \times Z_{DR}^{-3.31} \quad (4.2)$$

where, S is in cm h^{-1}, Z_{eH} in (mm^6 m^{-3}), and $Z_{DR} = 10^{(Z_{dr}/10)}$.

Figure (4.1) shows the scatter plot of the observed solid snowfall rates (cm h^{-1}) against the radar reflectivity (mm^6 m^{-3}) fitted with the $S(Z_{eH})$ algorithms. This figure shows that the fitting could be promising when compared to Figure (3.1). On the other hand, Figure (4.2) shows the subtle contribution of Z_{DR} when added to the algorithm. The underestimation of the current CWKR algorithm is also very prominent in this figure. Such underestimation was also noted by Boudala et al. (2006). It is worth noting that a 10:1 ratio is used by CWKR to convert SWE (mm h^{-1}) to solid snowfall rates (cm h^{-1}). Such constant SLR value is based on a Canadian study by Potter (1965), thus it is used by most meteorological applications in Canada (Boudala et al. 2014).

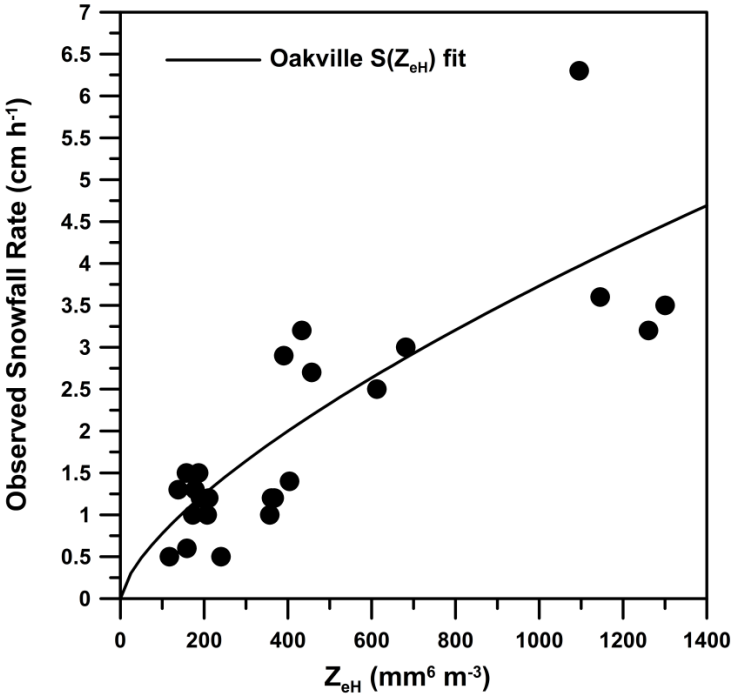

Figure (4.1) Observed snowfall rates from Oakville versus reflectivity factor and fitted $S(Z_{eH})$ algorithm (Eq. 4.1).

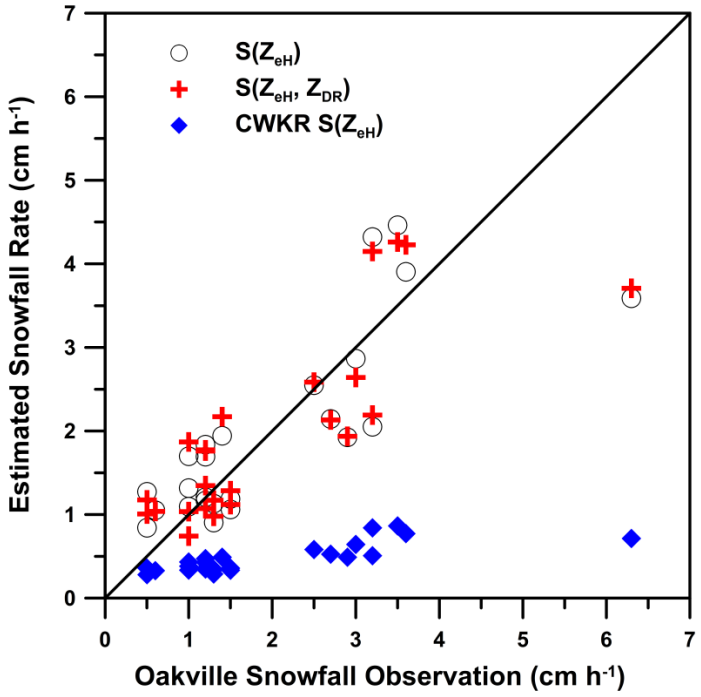

Figure 4.2 The observed snowfall rates from Oakville versus the estimated ones by the $S(Z_{eH})$ (Eq. 4.1), $S(Z_{eH}, Z_{DR})$ (Eq. 4.2), and the CWKR algorithms.

Table 4.1 shows the close score of both Equations 4.1 and 4.2 in estimating solid snowfall rates (cm h^{-1}). Table 4.2 further complements the previous table in showing the close overall estimation of both algorithms during the entire period (Jan-March, 2011). Both tables show the underestimation of the CWKR algorithm.

	$S(Z_{eH})$/Radar	**$S(Z_{eH}, Z_{DR})$**
Cor. Coeff.	0.802/0.802	0.815
Bias (cm h^{-1})	-0.00354/-1.49	0.00306
NMB %	-0.180/-75.8	0.155
MAE (cm h^{-1})	0.569/1.49	0.580
RMSE (cm h^{-1})	0.795/1.92	0.772
NMAE %	28.9/75.8	29.4
Est. Mean	1.97/0.478	1.97
Obs. Mean	1.97	1.97

Table (4.1) Statistical scores of the solid snowfall rate algorithms $S(Z_{eH})$ (Eq. 4.1), $S(Z_{eH}, Z_{DR})$ (Eq. 4.2), and the current King City radar CWKR ("Radar") algorithm. The Oakville data consists of (24) observations for winter 2011.

	$S(Z_{eH})$/Radar	$S(Z_{eH}, Z_{DR})$
Total Gauge (cm)	47.3	47.3
Total Algo. Est. (cm)	47.2/11.46	47.4
Under-Over Est.%	-0.180/-75.8	0.155

Table (4.2) Total solid snowfall observation versus total algorithms estimation (Eqs. 4.1 and 4.2) for the period Jan-March 2011. The 10:1 ratio is used by CWKR ("Radar") algorithm to convert SWE (mm h^{-1}) to solid snowfall rates (cm h^{-1}). The Oakville data set consists of (24) observations for winter 2011.

4.3 Verification of the Solid Snowfall Algorithms

The winter of 2011-2012 was warmer than normal in North America due to the unusual northward shift in the jet stream which in turn allowed above seasonal temperatures into southern Ontario throughout the entire season (statistically, more than half of Canada experienced above seasonal temperatures during that winter). Some of that could be attributed to the unusual position of the above normal 500 hPa heights during La Niña. Despite all that, many hours of solid snowfall observations were recorded in Oakville during Jan. and Feb. of 2012. The winter of 2012-2013 was more generous in solid snowfall observation and numerous hours of observations were recorded in Oakville. This data set will be used to verify Equations (4.1) and (4.2).

Figure (4.3) shows the observed snowfall rates (cm h^{-1}) against the estimated ones from the algorithms. It is clear from Figure (4.3) that the underestimation of the CWKR solid snowfall algorithm increases with precipitation rates. At first glance, both $S(Z_{eH})$ and $S(Z_{eH}, Z_{DR})$ are close

to the 1:1 line at times. This is a second confirmation that such algorithms could be valuable especially when compared to the CWKR estimation. Although both algorithms, i.e. Equations (4.1) and (4.2), are close to each other at times, the $S(Z_{eH}, Z_{DR})$ tend to overestimate solid snowfall rates for a few occasions due to the higher values of Z_{DR} during such observations.

There is an observation in Figure (4.3) where the three algorithms tend to underestimate. The observation was taken during a lake effect band off Lake Ontario on Jan 25, 2013 between (2100-2300 UTC). The main band of lake effect was skirting the eastern edge of the Town of Oakville with the main band affecting the city of Mississauga-Etobicoke, and east of the City of Toronto into Bowmanville. During two continuous hours of observation, 3 cm accumulated in the Oakville site. The reflectivity values over the Oakville site was very low, but the prevailing north-easterly winds managed to advect the falling snow from the eastern edge of the town to the observation site while keeping it below the radar beam height.

Table (4.3) demonstrate the statistical scores of the algorithms in Figure (4.3). With the exception of NMB and NMAE, the scores of both $S(Z_{eH})$ and (Z_{eH}, Z_{DR}) are close to each other with $S(Z_{eH})$ showing the lowest statistical scores. Table (4.4) shows the total solid snowfall estimation by the algorithms in comparison to the ground observation. The closest estimation to the ground truth is the one estimated by $S(Z_{eH})$ with only (8.33%) overestimation.

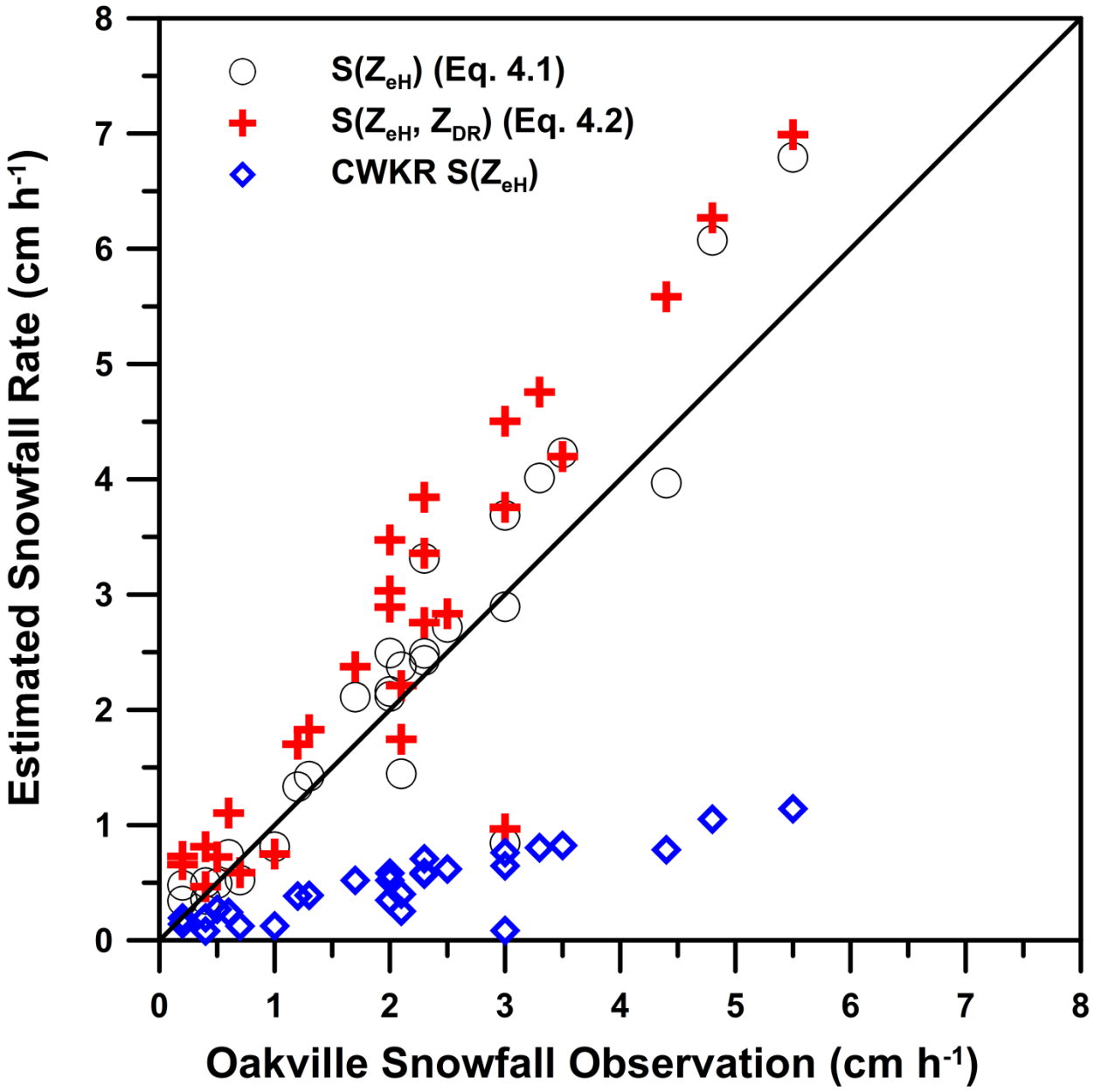

Figure (4.3) Solid snowfall observation (cm h^{-1}) from Oakville during the winter of 2012-2013 (Jan-Feb 2012, Dec 2012, and Jan-Feb 2013) versus estimated snowfall rates (cm h^{-1}) from Eqs. 4.1 and 4.2 and the CWKR algorithm.

	Eq. 4.1 $S(Z_{eH})$/Radar	Eq. 4.2 $S(Z_{eH}, Z_{DR})$
Cor. Coeff.	0.931/0.867	0.923
NB (cm h^{-1})	0.173/-1.61	0.593
NMB %	8.32/-77.1	28.5
MAE (cm h^{-1})	0.442/1.61	0.790
RMSE (cm h^{-1})	0.654/1.96	0.952
NMAE %	21.2/77.1	37.9
Est. Mean	2.26/0.477	2.68
Obs. Mean	2.08	2.08

Table (4.3) Statistical scores of the solid snowfall rate algorithms $S(Z_{eH})$ (Eq 4.1), $S(Z_{eH}, Z_{DR})$ (Eq. 4.2), and the CWKR ("Radar") when verified using solid snowfall observations from Oakville during winter 2012-2013. The Oakville data set consists of (28) observations for the winter of 2012-2013.

	$S(Z_{eH})$/Radar	$S(Z_{eH}, Z_{DR})$
Total solid snowfall (cm)	58.3	58.3
Total Algo. Est. (cm)	63.2/13.4	74.9
Under-Over Est. %	8.33/-77.1	28.5

Table (4.4) Total solid snowfall accumulation versus total algorithms estimation $S(Z_{eH})$ (Eq 4.1), $S(Z_{eH}, Z_{DR})$ (Eq. 4.2), and the CWKR ("Radar") for the winter of 2012-2013 (Jan-Feb 2012, Dec 2012, and Jan-Feb 2013). The 10:1 ratio is used by CWKR algorithm to convert SWE (mm h^{-1}) to solid snowfall rates (cm h^{-1}). The Oakville data set consists of (28) observations for the winter of 2012-2013.

To illustrate the conversion of reflectivity values to solid snowfall rates, a reported observation mentioned in Table (2.1) in section 2.1 will be used. A snowfall measurement of 1.5 cm was observed at the Oakville site between (0000-00100 UTC) on 27 February, 2011. Table (4.5) shows the six reflectivity values (dBz) during that hour (10 min radar scan). The reflectivity values must be converted to the linear scale before being implemented in any algorithm [$Z\ in\ dBz = 10 \times log_{10}(Z\ in\ mm^6 m^{-3})$]. The last two columns in Table (4.5) show the 10 min estimation of each of the algorithms (Radar and Eq. 4.1) in (cm). It is clear from the total estimation that the current radar algorithm underestimated solid snowfall by more than 4 times in this case. It is worth noting that the radar algorithm uses a constant 10:1 SLR to convert estimates SWE to solid snowfall rates while Equation (4.1) directly estimates solid snowfall.

Date	UTC	$Z_{(eH)}$ (dBz)	$Z_{(eH)}$ ($mm^6\ m^{-3}$)	Radar Est. (cm)	Eq. 4.1 Est. (cm)
27 Feb. 2011	00:00	23.2	208	0.0631	0.214
	00:10	22.5	178	0.0588	0.193
	00:20	24.2	262	0.0700	0.251
	00:30	20.7	119	0.0489	0.146
	00:40	22.1	161	0.0561	0.180
	00:50	22.9	193	0.0610	0.203
	Total snowfall ($cm\ h^{-1}$)			0.358	1.19

Table (4.5) An example illustrating the underestimation of the current Radar algorithm (Sekhon-Srivastava 1970) using reported observation from Oakville from Table (2.1).

The Oakville data set comprises of sampled snow-liquid ratio (SLR) values for the winter seasons of 2011, 2012, and 2013. SLR is defined as the ratio of the solid precipitation (mm) to its melted liquid (mm). The meteorological winter season was defined as (December-January-February). The median SLR value for the entire three winter seasons was 15:1 with a mean of 18:1. The seasonal median and mean SLR values in Table (4.5) show that the winter season of 2013 (December 2012 and January-February 2013) had the lowest values among the three seasons. It is worth noting that the 2012 winter season (January-February) comprises of very few data points due to the unusual above-seasonal temperatures associated with this season, thus the reported median and mean SLR values for this season does not fairly represent the entire season.

Winter Season	Mean SLR	Median SLR	# of Cases
December	13	14	8
January	19	17	16
February	21	15	20
March	13	14	6
Winter of 2011	21	17	23
Winter of 2012	22	20	7
Winter of 2013	14	12	20

Table (4.6) The mean and median SLR values and the number of cases for each month and season.

It is evident from Table (4.5) that the beginning and end of the winter season marks the lowest SLR values, and this agrees with Dubé (2003). Climatologically, January is considered the coldest month in Oakville (February the second coldest), thus higher values of SLR (low snow density) are associated with colder temperatures (Dubé 2003). The histogram in Figure (4.4) shows that highest frequency of SLR values lies between 10:1 and 15:1 (13:1 is considered as the highest SLR frequency among the entire sampled data set). SLR values of higher than 10:1 agrees with Baxter et al. (2005), Dubé (2003), and Roebber et al. (2003). The two very high SLR values (51:1 and 55:1) in the Oakville data (Figure 4.4) were associated with light density fluffy snow composed of aggregates and heavy snowfall rates which produced high ground accumulation and lower SWE values and this resulted in such high SLR values.

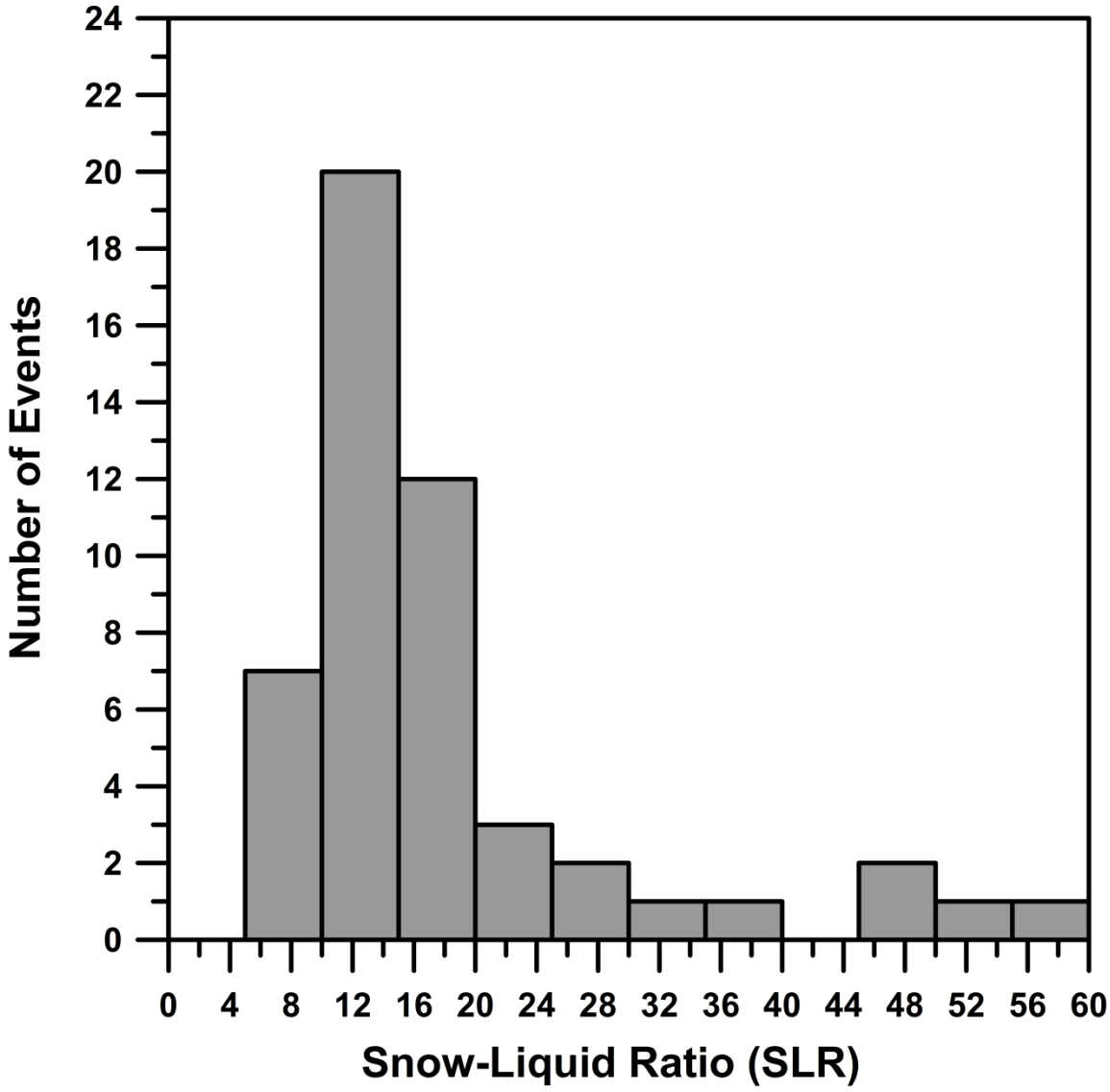

Figure (4.4) The distribution of the observed snow-liquid ratio (SLR) from the Oakville site for the 2011, 2012, and 2013 winter seasons.

Dubé (2003) showed no substantial difference in mean SLR with solid snowfall accumulations (cm). Similarly, the Oakville data did not further substantiate mean SLR values from solid snowfall intensity (Table 4.6). This could be attributed to the variation of SLR values within each event.

Snow Accumulation (cm)	Mean SLR
< 2	19
2-4	18
≥ 4	18

Table (4.7) The mean SLR values are categorized by solid snowfall accumulation during the 2011, 2012, and 2013 winter seasons.

CHAPTER FIVE: Rainfall Microphysical Properties and Estimation

5.1 Introduction

Unlike snow, decades of research are available in studying rainfall microphysical properties using polarimetric radars. Reflectivity factor based rainfall algorithms suffer from attenuation especially at the shorter wave radars, e.g. C and X band. Meanwhile, a phase-based rainfall algorithm, i.e. $R(K_{DP})$, is not affected by attenuation, partial beam blockage, calibration, or hail contamination (Zrnic and Ryzhkov 1996 and Vivekanandan et al. 1999). In addition to that, the differential reflectivity adds a further insight to the shapes of the droplets within the sampled volume (Vivekanandan et al. 1999). Thus when added to the reflectivity factor, $R(Z_{eH}, Z_{DR})$, it shows an improvement in rainfall estimation. The different responses that polarimetric variables have during precipitation enable them to be utilized in multiple ways. For instance, there are multiples polarimetric rainfall estimation algorithms and different Hydrometeor Identification algorithms (Hyang et al. 2009).

In this study the GEONOR B-200T gauge located in CYYZ was used to collect rainfall rates during May-Sept. of 2011 and 2012. Similar to the previous chapters, the gauge resolution is at 1 minute while the CWKR radar data are at 10 minutes interval. The gauge data were processed at 10 minutes interval to match the radar scan. In addition to quality control thresholds written within the program, a further visual inspection and comparison of METAR data with gauge observations and radar data were used to ensure the highest quality in the data set. No wind correction method was used as there is none for rain. Minimum surface temperatures were set to be greater than 15°C to ensure that the radar sampled volume was below the bright band (melting layer).

The first section will display the rainfall microphysical properties followed by the rainfall algorithms.

5.2 Rainfall Microphysical Properties

The polarimetric variables respond differently to rain than snow. Comparing Figure (2.1) Figure (5.1) reveals that ρ_{hv} is closer to unity in light and moderate rainfall then in snow. Moreover, the two figures depict a similar relationship between reflectivity factor and ρ_{hv}, i.e. ρ_{hv} increases with increasing reflectivity factor, but during heavy rainfall rates, ρ_{hv} shows a reduction in value. Such a reduction can be attributed to the presence of hail or larger droplets. Only one confirmed observation from CYYZ METAR of 3 mm hail on the ground was reported during the entire data set. In this case ρ_{hv} dropped to (0.940) while Z_{eh} was (50.9 dBz) and Z_{dr} jumped to (4.64 dB). This agrees with Anderson et al. (2011) as they found that higher Z_{dr} (3-8 dB) during hail events using a C-band radar. This can be attributed to a resonance effect if the sampled volume contains large rain drops and melting hailstones ($D \geq 5.5$ mm at C-band) (Zrnic et al. 2000). Otherwise, the sampled volume is dominated by a mixture of large raindrops and small melting hail (Ryzhkov et al. 2007). Two cases were also found with similar radar variables, but no ground observation confirmed hail at the airport. The hail could have melted before hitting the ground or landed few hundreds of meters away from the airport. The other low values of ρ_{hv} at higher rainfall rates could be attributed to the presence of a mixture of larger and small drops within the sampled volume that leads to a lower ρ_{hv}. The presence of only large drops within the sampled volume would produce resonant scattering and lower ρ_{hv} values.

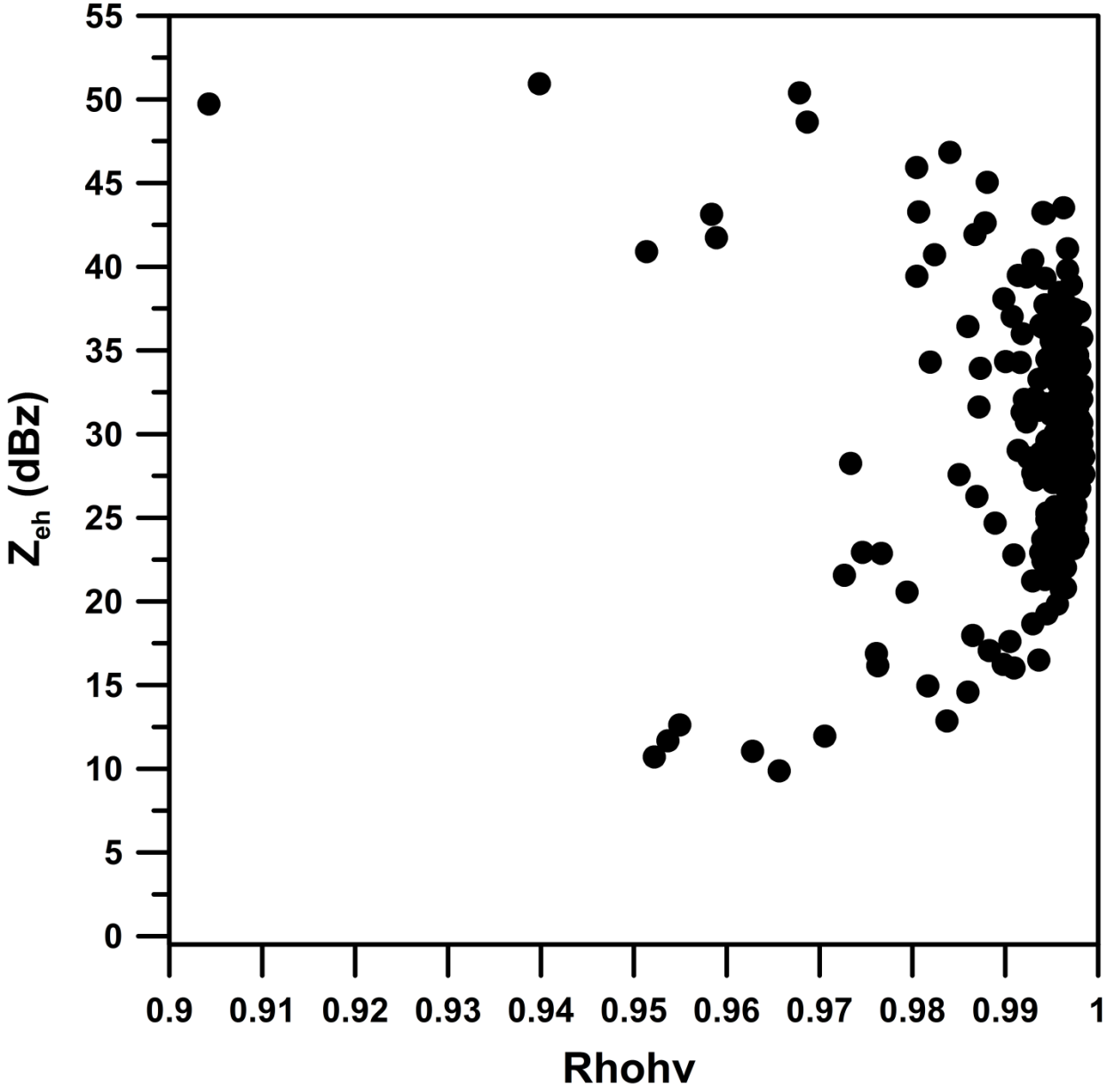

Figure (5.1) Reflectivity factor (dBz) versus co-polar correlation coefficient during rainfall events for the period May-Sept. 2011 and 2012.

Unlike snow, Figure (5.2) shows that Z_{DR} tends to increase with increasing reflectivity factor. As the rainfall event gets heavier, the coalescence process tends to occur, which increases the drop size. The overall aerodynamic forces (e.g. surface tension, hydrostatic pressure, external aerodynamic pressure, electrostatic charge, and internal circulation) affecting the falling drops lead them to have a flattened base and smoothly rounded curvature (like a hamburger bun). The radar horizontally polarized signal will undergo more resistance than the vertical signal and thus would lead to higher Z_{DR} values. During hail events, Z_{DR} tends to decrease with increased Z_{eH} in S-band radars. This is due to the fact that hailstones are less oblate than raindrops, hailstones tend to tumble while falling, and hailstones have a smaller dielectric constant than raindrops (Anderson et al. 2011). The opposite occur in C-band radars, as Z_{DR} increases with increasing Z_{eH}. Due to the resonance effects associated at such shorter wavelengths. Thus, larger hailstones, smaller melting hailstones, or bigger raindrops tend to produces higher Z_{DR} values in C-band than S-band radars (Zrnic et al. 2000 and Ryzhkov et al. 2007b).

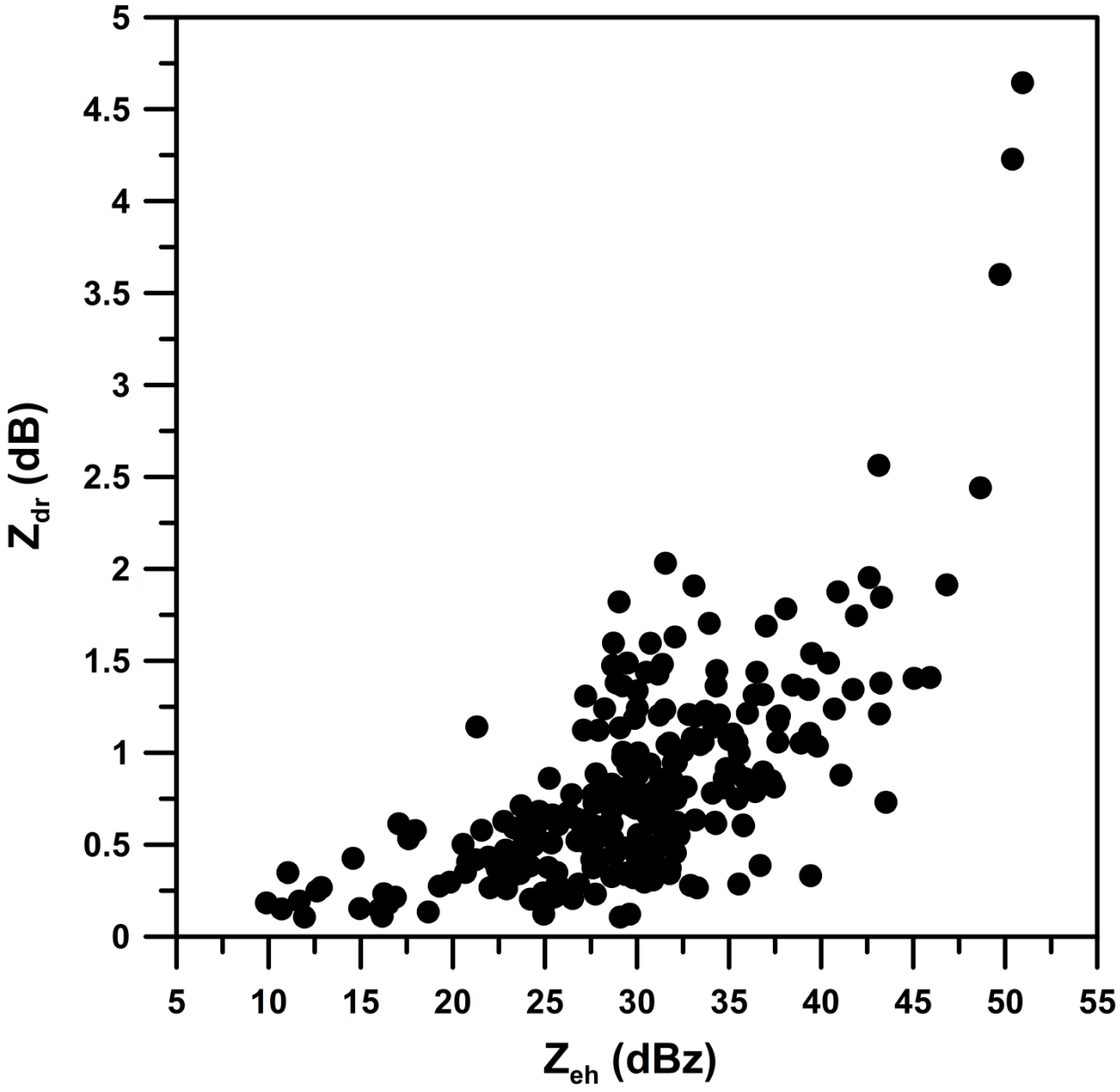

Figure (5.2) Differential reflectivity (dB) versus reflectivity factor (dBz) during rainfall events for the period May-Sept. 2011 and 2012.

Similar to Z_{DR}, K_{DP} tends to generally increase with increasing rainfall rates as seen in Figure (5.3). K_{DP} is a measure of total liquid water content (LWC) along the path. In addition to its numerous benefits, K_{DP} tends not to be exaggerated during the presence of hail within the sampled volume (Jameson 1985). This is substantial since Z_{eH} tends to over exaggerate during the presence of hail. The only caveat is that during the presence of large hydrometeors ($5.5<D<7$ mm at C-band) the resonance effect tends to bring K_{DP} to sub-zero values, thus producing negative rainfall rates in K_{DP}-based algorithms (Snyder et al. 2010).

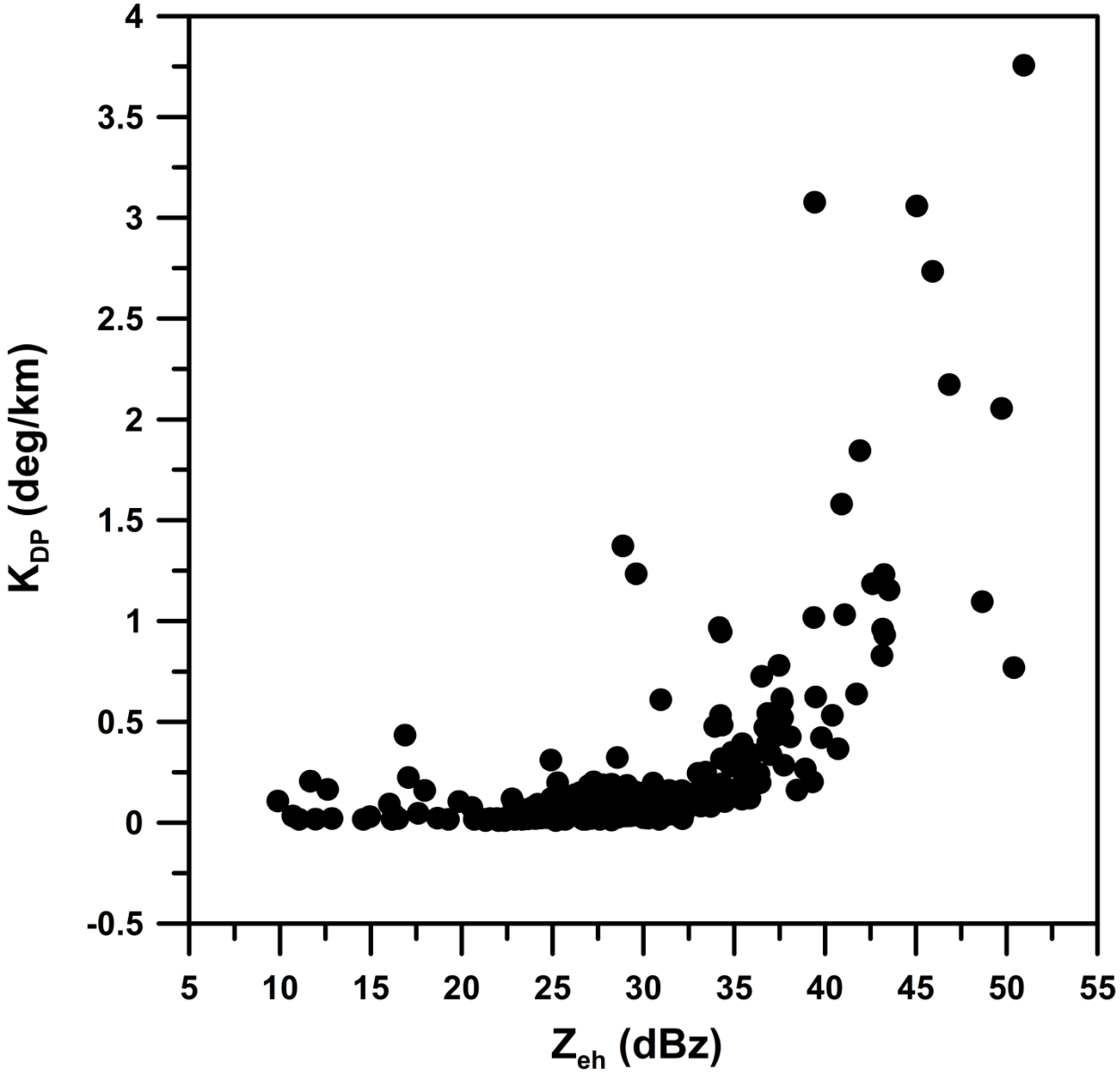

Figure (5.3) Specific differential phase shift (°/km) versus reflectivity factor (dBz) during rain events for the period May-Sept. 2011 and 2012.

5.3 Rainfall Algorithms

Rainfall measurements were collected using the GEONOR T-200B at CYYZ during May-September of 2011 and 2012. Observed surface temperatures (T > 15°C) were used as a preliminary screening method to ensure no rain-snow mix or wet snow cases are included within the radar sample volume over the airport (~ 400 m AGL). 10-minutes interval gauge accumulations were visually checked before being compared to the different radar variables (i.e. Z_{eH}, ρ_{hv}, K_{DP}, and Z_{DR}) to ensure higher data quality.

The current algorithm adopted by CWKR radar is the Marshall-Palmer (1948) given as:

$$R(Z_{eH})_{MP} = 0.0365 \times Z_{eH}^{0.6250} \tag{5.1}$$

where Z_{eH} is in ($mm^6\ m^{-3}$).

The CYYZ data set collected between May-Sept. of 2011 and 2012 was used to train three different algorithms to be then compared to the current CWKR algorithm, i.e. Eq. 5.1. The trained algorithms will also be compared with their counterpart algorithms developed by Bringi et al. (2011). The Bringi et al. (2011) algorithms were developed using Joss disdrometer data from Chilbolton, UK and C-band radar in convective storms during three summer months of 2007. Once the drop size distribution information was obtained from the disdrometer data, the data were used in a FORTRAN-based computer model, named T-Matrix, to obtain the algorithms coefficients while assuming constant values for the drop axial ratio, temperature, radar wavelength, and the attenuation correction method to correct Z_{eH} and Z_{DR}.

The three rainfall algorithms developed in this study can be written as:

$$R(Z_{eH}) = 0.349 \times Z_{eH}^{0.437} \tag{5.2}$$

$$R(Z_{eH}, Z_{DR}) = 0.0561 \times Z_{eH}^{0.700} \times Z_{DR}^{-1.66} \tag{5.3}$$

$$R(K_{DP}) = 25.8 \times K_{DP}^{0.660} \quad (5.4)$$

where Z_{eH} in ($mm^6\ m^{-3}$), $Z_{DR} = 10^{(Z_{dr}/10)}$, Z_{dr} in (dB), and K_{DP} in (°/km).

Figure (5.4 a-c) shows the three algorithms compared to the observations. It is worth noting that no wind correction method was used to correct gauge accumulation as there isn't one available. Figure (5.4 a) shows that the Bringi et al. (2011) $R(Z_{eH})$ algorithm (V.B. $R(Z_{eH})$) tends to underestimate rainfall rates when compared to the other two algorithms. In Figure (5.4 a) and at the lower scale of rainfall rates, i.e. observed rainfall rates ≤ 20 mm h^{-1}, the $R(Z_{eH})$ developed in this study generally tends to overestimate the rainfall rates while a general underestimation is noticed by Bringi et al. (2011) and the CWKR $R(Z_{eH})$. For rainfall rates > 20 mm h^{-1}, the $R(Z_{eH})$ developed in this study tends to reasonably estimate rainfall rates when compared to the other two algorithms. A noticeable improvement can be seen in estimating rainfall rates in Figure (5.4 b) when Z_{DR} is incorporated in the algorithm. A similar remark can be made as the Bringi et al. (2011) algorithm estimates lower rainfall rates when compared to the current algorithms developed in this study. Although the $R(K_{DP})$, Figure (5.4 c), doesn't show a substantial improvement at the lower scale of rainfall rates, but arguably improves rainfall estimation when compared to Figure (5.4 b) during rainfall rates > 20 mm h^{-1}. The differences between all three algorithms in this study and their counterparts from Bringi et al. (2011) could be due to the different methods used to obtain the coefficients of the algorithm.

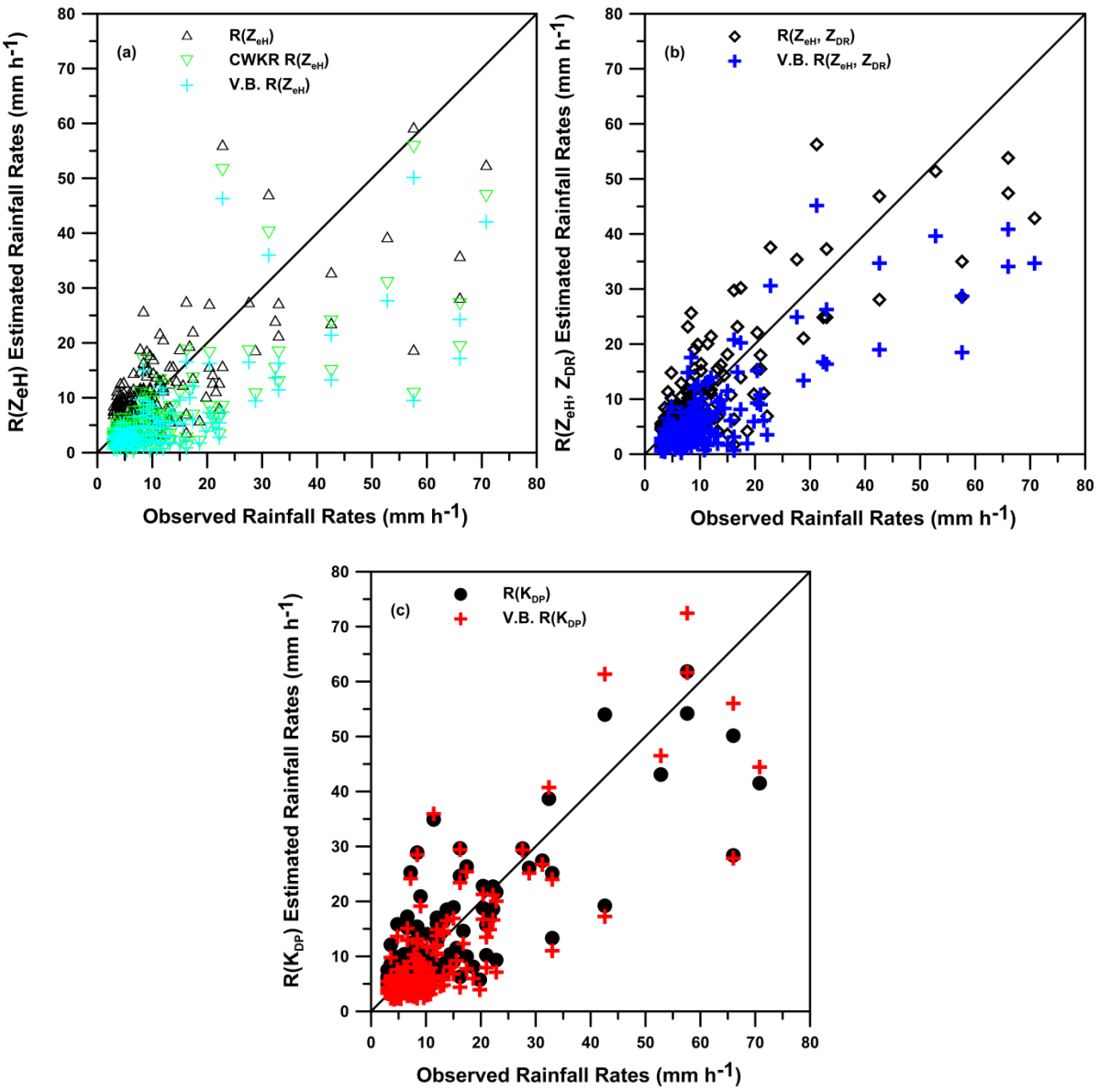

Figure (5.4 a-c) Three algorithms developed in this study (Eqs. 5.1, 5.2, and 5.3) versus observed rainfall rates from CYYZ during May-Sept. 2011 and 2012. The developed algorithms are compared to CWKR and Bringi et al. (2011) algorithms.

Tables (5.1) and (5.2) below show the statistical skills of the algorithms compared to their counterparts from CWKR and Bringi et al. (2011). The $R(K_{DP})$ and $R(Z_{eH}, Z_{DR})$ algorithms show substantial improvements when compared to the CWKR algorithm with about ~40% improvement in total rainfall estimation. Unlike estimating SWE, polarimetric variables are shown to add significant value in estimating rainfall rates, especially during heavy rainfall rates as can be seen in Figure (5.4 b-c). Although the Bringi et al. (2011) polarimetric-base algorithms were developed using a different method with a larger data sample, the algorithms in this study have comparable estimation to the Bringi et al. (2011) ones, especially the $R(K_{DP})$ as seen in Table (5.1).

	$R(Z_{eH})$/Radar	$R(Z_{eH}, Z_{DR})$	$R(K_{DP})$	V.B. $R(Z_{eH})$	V.B. $R(Z_{eH}, Z_{DR})$	V.B. $R(K_{DP})$
Cor. Coeff.	0.754/0.744	0.826	0.826	0.744	0.832	0.829
MB (mm h^{-1})	-0.0913/-5.32	-0.554	-0.210	-5.96	-4.73	-1.77
NMB %	-0.802/-0.467	-4.84	-1.84	-52.4	-41.3	-15.5
MAE (mm h^{-1})	5.04/6.03	4.50	4.08	6.43	5.50	4.37
RMSE (mm h^{-1})	7.75/9.54	6.87	6.67	10.0	8.42	7.01
NMAE %	44.3/52.9	39.3	35.8	56.4	48.1	38.4
Est. Mean	11.3/6.07	10.9	11.2	5.42	6.72	9.62
Obs. Mean	11.4	11.5	11.4	11.4	11.5	11.4

Table (5.1) Statistical scores of the three algorithms (Eqs. 5.1, 5.2, and 5.3) compared to their counterparts from CWKR ("Radar") and Bringi et al. (2011) (V.B.). The CYYZ data set consists of (180) observations for May-September of 2011-2012 [169 observations for the $R(Z_{eH}, Z_{DR})$ algorithms].

	$R(Z_{eH})$/Radar	$R(Z_{eH}, Z_{DR})$	$R(K_{DP})$	V.B. $R(Z_{eH})$	V.B. $R(Z_{eH}, Z_{DR})$	V.B. $R(K_{DP})$
Total Gauge (mm)	2050	1936	2050	2050	1936	2050
Total Algo. Est.(mm)	2033/1093	1842	2012	976	1136	1732
Under-Over Est.%	-0.802/-46.7	-4.84	-1.84	-52.4	-41.3	-15.5

Table (5.2) Total rainfall from gauge compared to total rainfall estimation from the algorithms. The CYYZ data set consists of (180) observations for May-September of 2011-2012 [169 observations for the $R(Z_{eH}, Z_{DR})$ algorithms].

It is worth noting that the difference between the R(Z_{eH}, Z_{DR}) data set and the other algorithms is due to the fact that a few observations were discarded due to their unreasonable Z_{DR} values while other parameters were reasonably valued.

The polarimetric-based algorithms show improved skills in estimating rainfall rates at certain polarimetric variable thresholds. Thus, a logic tree was devised to choose the optimal algorithm based on the radar variables as seen in Figure (5.5). The thresholds in the logic tree were drawn by comparing the best rainfall estimation to the polarimetric variables.

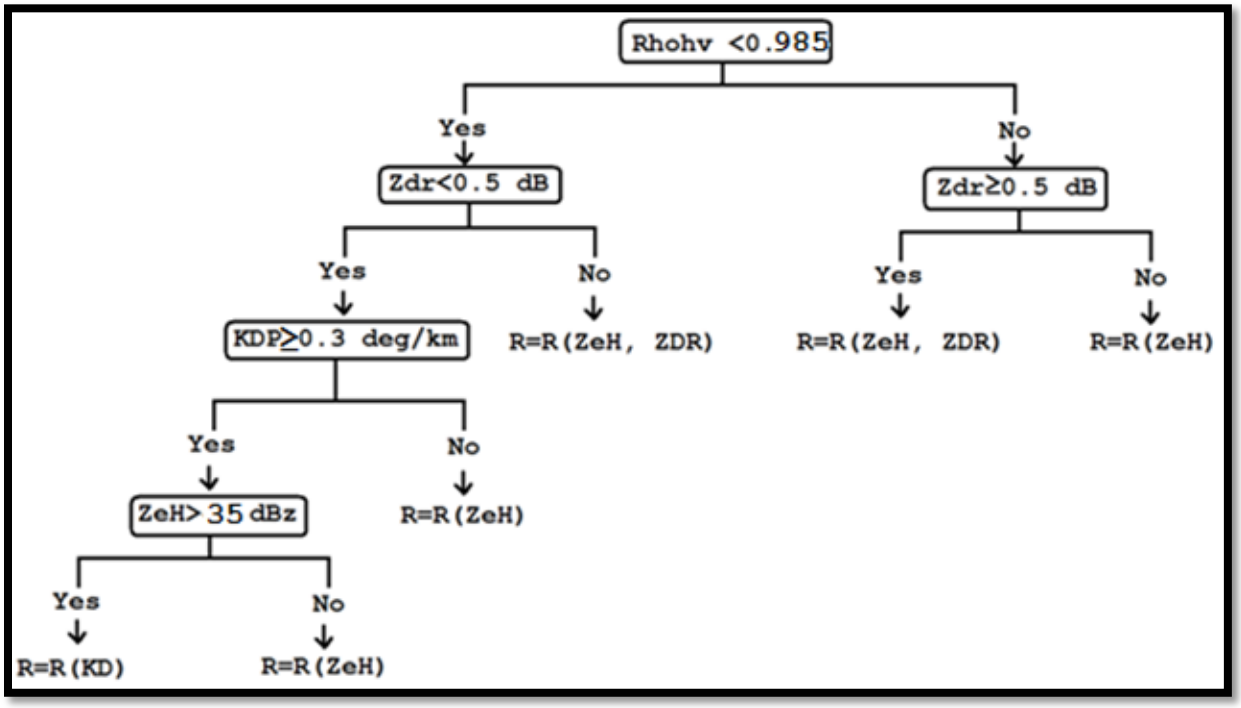

Figure (5.5) Logic tree decision making chart to choose the optimal algorithm to estimate rainfall rates.

The logic tree conditions were applied to the same data set and as seen in Figure (5.6). Comparing Figures (5.6) and (5.5) shows improvement in the estimating rainfall rates mainly along the heaviest rainfall rates. Tables (5.3) and (5.4) further support the role of the logic tree-based algorithms in estimating rainfall rates.

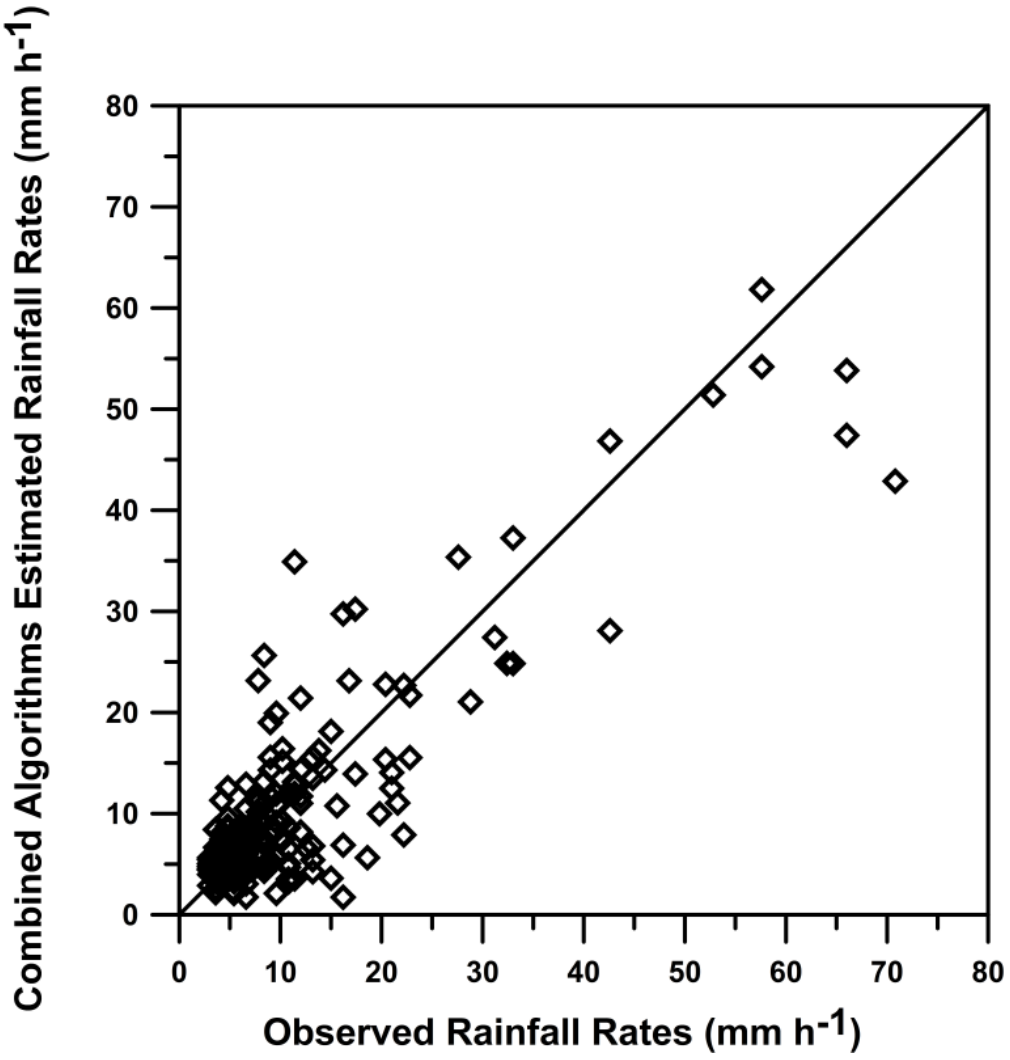

Figure (5.6) Estimated rainfall rates (mm h^{-1}) based on the logic tree decision making versus observed rainfall rates (mm h^{-1}).

	Combined Algorithms
Cor. Coeff.	0.868
MB (mm h^{-1})	-0.405
NMB %	-3.56
MAE (mm h^{-1})	3.96
RMSE (mm h^{-1})	5.90
NMAE %	34.8
Est. Mean	11.0
Obs. Mean	11.4

Table (5.3) Statistical skills of the logic tree-based algorithms. The CYYZ data set consists of (180) observations for May-September of 2011-2012.

	Combined Algorithms
Total Gauge (mm)	2050
Total Algo. Est.(mm)	1977
Under-Over Est.%	-3.56

Table (5.4) Total rainfall from gauge compared to total rainfall estimation from the logic tree-based algorithms. The CYYZ data set consists of (180) observations for May-September of 2011-2012.

There will always be a mismatch between ground observations and radar sampling volume. Increasing the spatial coverage of ground observations would reduce such a disparity and would improve rainfall estimation. The algorithms developed in this study are considered among the first to be developed using data from southern Ontario and Canada. Environment Canada is currently in the process of upgrading the current radar network with dual polarization capability. The algorithms developed in this study could be implemented across Canada to further verify the proposed logic tree thresholds, and thus improve up on estimating rainfall rates.

CHAPTER SIX: Summary and Conclusions

Weather events can cause fatalities, substantial damage, and inconvenience across the globe. Since weather events are inevitable, forecasting such events with accuracy can help reduce such constraints. One of the main tools that forecasters use is weather radars. Hydrologists also find weather radar very useful to quantitatively estimate the amount of precipitation which has fallen over a particular area (e.g. drainage basin, city, etc.). Decades of research in the area of radar meteorology have led to an upgraded generation of radars that use dual polarimetric capabilities instead of the commonly used mono-polarized ones (e.g. McCormick and Hendry 1975; McCormick and Hendry 1979; McCormick 1981). Environment Canada is following the USA in upgrading their entire radar network with dual polarimetric capabilities.

This study aims to *i.)* evaluate the current snowfall algorithm implemented by Environment Canada for Canadian radars to estimate Snow Water Equivalent (SWE), *ii.)* establish new algorithms to better represent observed SWE, *iii.)* evaluate the capabilities of dual polarimetric-based algorithms in estimating SWE, *iv.)* establish algorithms to directly estimate solid snowfall rates, *v.)* develop a set of algorithms to better estimate rainfall rates.

To achieve this, ground observations from three sites in Canada were used. SWE and solid snowfall rates were measured in Oakville, Ontario, during the winter season of 2011, 2012, and 2013. The hourly observations at Oakville consisted of SWE and solid

snowfall measurements in addition to crystal types and sizes. SWE observations from the CAN-Now project at Pearson International Airport (CYYZ) near Toronto, Ontario, were acquired from a GEONOR T-200B gauge during the winter of 2011/2012 in addition to rainfall measurements during May-September of 2011 and 2012. Finally, SWE measurements from a GEONOR T-200B gauge located in Mount Pearl, Newfoundland, were obtained during the winter season of 2011-2012.

In conjunction with the ground observations, radar data were used from the dual-polarized King City radar (CWKR) located just north of Toronto, Ontario, and the Holyrood radar (CWTP) located in Newfoundland. It is worth noting that all the data, ground observations and radar, were quality controlled and also visually inspected to ensure high quality data. The Oakville ground observation data were at 1 hr intervals, while the CYYZ and Mt. Pearl gauge temporal resolution were at 1 min. The radar data used throughout the entire study were consistently at 10 min intervals.

The gauge at CYYZ was surrounded by a Nipher shield while an Alter shield surrounded the gauge at Mt. Pearl. Accordingly, two different wind correction methods were used to calculate gauge catchment efficiency and correct the measured SWE for winds.

The gauge data from CYYZ and Mt. Pearl were accumulated into 10 min intervals and also in 1 hr intervals. The 1 hr interval data from the Oakville and CYYZ sites were used to develop two algorithms that estimate SWE, $S(Z_{eH})$ and $S(Z_{eH}, Z_{DR})$, while the Mt. Pearl 1 hr interval data were used to develop a $S(Z_{eH})$ algorithm. No polarimetric-based

algorithms were established in Mt. Pearl because the CWTP radar is yet to be equipped with dual polarimetric capabilities.

The 10 min interval gauge data from CYYZ and Mt. Pearl were used to develop two $S(Z_{eH})$ algorithms, one for each site. Moreover, the 10 min interval CYYZ data were used to develop a $S(Z_{eH}, Z_{DR})$ algorithm. The main reason behind handling the gauge data at different time intervals is to examine the algorithms' sensitivity to the gauge collection time interval.

Furthermore, the 1 hr interval data from the three sites were combined to produce one data set that is used to develop a $S(Z_{eH})$ algorithm. This leads to four $S(Z_{eH})$ and two $S(Z_{eH}, Z_{DR})$ hourly based algorithms in addition to two $S(Z_{eH})$ and two $S(Z_{eH}, Z_{DR})$ 10 min based algorithms.

The results show that the 10 min-based algorithms tend to overestimate SWE at the lower snowfall rates and underestimate SWE at the higher snowfall rates. The main reason was attributed to the fact that during light snowfall rates, especially during snow crystal and aggregate events, the gauge may not represent an accurate measurement during such a short time interval.

It was found that the polarimetric-based algorithms, $S(Z_{eH}, Z_{DR})$, show only subtle differences when compared to the $S(Z_{eH})$ algorithms. This was attributed to the low sensitivity of the polarimetric variables during moderate and heavy snowfall rates.

The algorithms developed in this study were compared against the current CWKR, the Finnish Meteorological Institute, and Huang et al. 2010 algorithms. The hourly algorithms developed in this study showed better statistical scores for individual sites

when compare to their counterparts' algorithms. The uncertainty of the algorithms is represented by the RMSE if the bias is small, as the case for the SWE algorithms developed here, but not with the CWKR algorithm. The hourly $S(Z_{eH})$ and $S(Z_{eH}, Z_{DR})$ algorithms based on the combined data set have minimal bias and the mean absolute errors (MAE) suggest a SWE uncertainty of less than 50% (Table 3.5). The current CWKR algorithm has a large negative bias (Table 3.1) of about 60% which dominates the uncertainty of those estimates. The similarity of the $S(Z_{eH})$ algorithm for Ontario and Newfoundland suggests that one algorithm might be suitable for different climate zones. However, this should be studied in more detail using data from other sites. It is worth noting that increasing the data set could only refine the coefficients of the $S(Z_{eH})$ algorithm to a certain degree, but would not reduce the scatter between SWE and radar reflectivity factor.

According to the Box and Whisker plot in Figure (3.8), for an estimated SWE of 2.4 mm h^{-1} by the combined algorithm there is a 50% probability that the observed SWE would be 1.6-3.3 mm h^{-1}. Meanwhile, for an estimated 0.55 mm h^{-1}, there is 50% probability that the observed SWE would lie between 0.35-0.8 mm h^{-1}. It is recognized that estimating snowfall rates (SWE) with these algorithms are not precise and there is a considerable level of uncertainty at times. Although defining the level of the uncertainty was not one of the objectives of this research, further work should be done in order to help inform the end user.

Rainfall measurements at 1 min temporal resolution from CYYZ were accumulated at 10 min intervals to train three rainfall rate algorithms [$R(Z_{eH})$, $R(Z_{eH}$,

Z_{DR}), R(K_{DP})]. Unlike for snow, polarimetric parameters add significant value for rainfall estimation. These algorithms showed better statistical scores when compared with the current Marshall-Palmer algorithm used by the CWKR (and the entire Environment Canada radar network).

Since the polarimetric-based algorithms are sensitive to the different radar variables, a logic tree was devised to choose the optimal algorithm using radar variables thresholds. The verification of the logic tree-based algorithms shows an improvement in estimating rainfall rates.

It was found that although the polarimetric-based algorithms do not further contribute to SWE estimation, polarimetric variables are able to shed a light on few microphysical processes during snow and rainfall events and thus be used in radar-based hydrometeor classification algorithm s (e.g. Thompson et al. 2014; Dolan and Rutledge 2009).

The ground observations revealed that the co-polar correlation coefficient, ρ_{hv}, could be sensitive to the size ranges of different snow habits within the radar sampled volume and thus could be used to distinguish different mixture of hydrometeors, e.g. ice pellets and snow or freezing rain and snow.

The results also showed that although lower Z_{DR} values are associated with aggregates, higher Z_{DR} values are also measured with large aggregates. The reason behind such higher values of Z_{DR} was attributed to the Mie resonance effect, lower fluttering angles, or the presence of an induced field transverse along the horizontal axis of the aggregates.

The importance of this study is highlighted year-round in Canada. The severe isolated thunderstorms that occurs every summer across the country (like the one occurred in Toronto on July 8th, 2013) can produce flash flood events in a very short time and can leave motorists and pedestrian stranded in addition to causing havoc to cities and municipalities and their associated infrastructural services. Such algorithms and a logic tree, like the one developed in this study, can increase the forecasters' ability to issue the appropriate warnings. Furthermore, the usual Canadian winter produces snow across a great part of the country, thus accurate estimation of SWE and solid snowfall rates serve as vital information to meteorologists and hydrologists. Government agencies and private companies can better plan their operations to mitigate the human and financial loss caused by such weather events with improved quantitative snowfall information.

References

Anderson, M. E., L. D. Carey, W. A. Petersen, and K. R. Knupp, 2011: C-band dual-polarimetric radar signatures of hail. *J. Opera. Meteor.*, EJ02.

Andric, J., D. Zrnic, J. M. Straka, and V. Melnikov, 2010: The enhanced Z_{DR} signature in stratiform clouds above melting layer. *13th Conf. on Cloud Physic, Portland, Oregon, Amer. Meteor. Soc., P2.89.* [http://ams.confex.com/ams/13CldPhy13AtRad/techprogram/paper_171308.htm].

Andric, J., M. R. Kumjian, D. S. Zrnic, J. M. Straka, and V. M. Melnikov, 2013: Polarimetric signatures above the melting layer in winter storms: An observational and modeling study. *J. Appl. Meteor. Climatol.*, **52**, 682-700, doi:10.1175/JAMC-D-12-028.1.

Atlas, D., Ed., 1990: Radar in Meteorlogy - Battan Memorial and 40th Anniversary Radar Meteorology Conference. Amer. Meteor. Soc., 806 pp.

Aydin K., V. N. Bringi, and L. Liu, 1995: Rain-rate estimation in the presence of hail using S-band specific differential phase and other radar parameters. *J. Appl. Meteor.*, **34**, 404-410.

Bader, M. J., S. A. Clough, and G. P. Cox, 1987: Aircraft and dual polarization radar observations of hydrometeors in light stratiform precipitation. *Quart. J. Roy. Meteor. Soc.*, **113**, 491-515.

Baldini, L., E. Gorgucci, V. Romaniello, 2008: An integrated procedure for rainfall estimation using C-band dual-polarization weather radars. Radar Conf. RADAR '08. IEEE, Rome.

Battan, L. J., 1973: Radar Observation of the atmosphere. The University of Chicago Press, Chicago, 324 pp.

Baxter, M. A., C. E. Graves, and J. T. Moore, 2005: A climatology of snow-to-liquid ratio for the contiguous United States. *Wea. Forecasting*, **20**, 729-744.

Bent, A. E., 1943: Radar echoes from atmospheric phenomena. M.I.T. Radiation Laboratory Rep. No. 42-2, March 13, 1943.

Boodoo, S., D. Hudak, M. Leduc, A. V. Ryzhkov, N. Donaldson, and D. Hassan, 2009: Hail detection with a C-band dual polarization radar in the Canadian Great Lakes region. 34th Conf. on Radar Meteo., Williamsburg, VA, USA, AMS.
[http://ams.confex.com/ams/34Radar/techprogram/paper_156032.htm].

Boudala, F. S., R. Rasmuseen, G. A. Isaac, and B. Scott, 2014: Performance of hot place for measuring solid precipitation in complex terrain during the 2010 Vancouver Winter Olympics. *J. Atmos. Oceanic Technology*, **31**, 437-446.

Boudala, F. S., G. A. Isaac, and D. Hudak, 2006: Ice water content and precipitation rate as a function of equivalent radar reflectivity and temperature based on in situ observations. *J. Geophys. Res.*, **111**, D11202, doi:10.1029/2005JD006499.

Brandes, E. A., 2000: Dual-polarization radar fundamentals and algorithm prospects. NCAR, Boulder, Colorado. [http://www.roc.noaa.gov/wsr88d/PublicDocs/AppsDocs/algorithm00.pdf].

Bringi, V. N., and V. Chandrasekar, 2001: *Polarimetric Doppler Weather Radar: Principles and Application*. Cambridge University Press, 179 pp.

Bringi, V. N., M. A. Rico-Ramirez, and M. Thurai, 2011: Rainfall estimation with an operational polarimetric C-band radar in the United Kingdom: comparison with gauge network and error analysis. *J. Hydrometeor.*, **12**, 935-954.

Browne, I. C., and N. P. Robinson, 1952: Cross-polarization of the radar melting band. *Nature*, **1970**, 1078-1079.

Carey, L. D., W. A. Petersen, and E. V. Schultz, 2011: Dual-polarimetric signatures of ice orientation for lightning prediction: A radar modeling study of ice mixtures at X, C and S bands. *91st AMS Annual Meeting, Lightning*

warning and prediction using observations and models II session, Seattle, Washington.

Chandrasekar, V., V. N. Bringi, N. Balakrishnan, and D. S. Zrnic, 1990: Error structure of multiparameter radar and surface measurements of rainfall. Part III: Specific differential phase. *J. Atmos. Oceanic Technol.*, **7**, 621-629.

Cremonini, Roberto and Renzo Bechini, 2010: Heavy rainfall monitoring by polarimetric C-band weather radars. *Water*, **2**, 838-848, doi:10.3390/w2040838.

Crisologo, I., G. Vulpiani, C. C. Abon, C. P. C. David, A. Bronster, and Maik Heistermann, 2014: Polarimetric rainfall retrieval from a C-band weather radar in a tropical environment (The Philippines). *Asia-Pacific J. Atmos. Scie.*, **50**, 595-607.

Dolan, B. and S. A. Rutledge, 2009: A theory-based hydrometeor idenitifcation algorithm for X-band polarimetric radars. *J. Amots. Scie. Oceanic Technol.*, **26**, 2071-2088.

Dubé, I.,2003: From mm to cm. Study of snow/liquid water ratios in Quebec. Meteorological service of Canada, Quebec region, internal Rep., 127. [www.meted.ucar.edu/norlat/snowdensity/from_mm_to_cm.pdf].

Feingold, G. and Z. Levin, 1986: the lognormal fit to raindrop spectra from convective clouds in Israel. *J. Clim. Appl. Meteorol.*, **25**, 1346-1363.

Frontline Systems, Inc., www.solver.com

GEONOR, 2008: T-200B Series Precipitation Gauge. [http://www.geonor.com/precipitation_gauge.html].

Gershenzon, Yu. M., and A. B. Shupyatsky, 1961: Scattering of elliptically polarized radio waves by nonspherical atmospheric particles. *Tr. Cent. Aerolog. Obs.*, **36**, 102–108 (in Russian).

Goodison, B. E., P. Y. T. Louie, and D. Yang, 1998: WMO Solid Precipitation Measurement Intercomparison. WMO Instruments and Observing Methods, Report No. 67, 36 pp.

Gorguci, E., and G. Scarchilli, 1997:Intercomparison of multiparameter radar algorithms for estimating rainfall rate. 28th Conf. on Radar Meteorology, Austin, TX, USA, AMS. 55-56.

Gu, Ji-Young, A. Ryzhkov, P. Zhang, P. Neilley, M. Knight, B. Wolf, Dong-In Lee, 2011: Polarimetric attenuation correction in heavy rain at C band. *J. Appl. Meteor. Climatol.*, **50**, 39-58.

Hitschfeld, W. F., 1986: The invention of radar meteorology. Bull. Amer. Meteor. Soc., **67**, 33-37.

Hogan, R. J., P. R. Field, A. J. Illingworth, R. J. Cotton, and T. W. Choularton, 2002: Properties of embedded convection in warm-frontal

mixed-phase cloud from aircraft and polarimetric radar. *Q. J. R. Meteorolo. Soc.*, **128**, 451-476.

Houze, R. A., Jr., P. V. Hobbs, P. H. Herzegh, and D. B. Parsons, 1979: Size distributions of precipitation particles in frontal clouds. *J. Atmos. Sci.*, **36**, 156-162.

Huang, G.-J., V. N. Bringi, R. Cifelli, D. Hudak, and W. A. Petersen, 2010: A methodology to derive radar reflectivity-liquid equivalent snow rate relations using C-band radar and a 2-D video disdrometer. *J. Atmos. Oceanic Technol.*, **27**, 637–651.

Hubbert J., and V. N. Bringi, 1995: An iterative filtering technique for the analysis of copular differential phase and dual-frequency radar measurements. *J. Atmos. Oceanic Technol.*, **12**, 634-648.

Hudak, D., P. Rodriguez, G. W. Lee, A. V. Rhyzhkov, F. Fabry, and N. Donaldson, 2006: Winter precipitation studies with a dual polarized C-band

radar. Fourth European Conf. on Radar in Meteorology and Hydrology (ERAD 2006), Barcelona, Spain, 9-12.

Hunter, I. M., 1954: Polarization of radar echoes from meteorological precipitation. *Nature*, **1973**, 165-166.

Hyang, S. K., A. V. Ryzhkov, D. S. Zrnic, and K. E. Kim, 2009: The hydrometeor classification algorithm for the polarimetric WSE-88D: Description and application to an MCS. *Wea. Forecasting*, **24**, 730-748.

Ikeda K., E. A. Brandes, G. Zhang, and S. A. Rutledge, 2005: Observations of winter storms with a 2-D video disdrometer and polarimetric radar. AMS 32nd Conf. on Radar Meteor., Albuquerque, NM, USA. [http://ams.confex.com/ams/32Rad11Meso/techprogram/paper_97054.htm].

Isaac, G. A., M. Bailey, F. Boudala, S. G. Cober, R. Crawford, N. Donaldson, I. Gultepe, B. Hansen, I. Heckman, L. Huang, A. Ling, J. Mailhot, J. A. Milbrandt, J. Reid, and M. Fournier, 2012: The Canadian airport nowcasting systems (CAN-Now). In press *Meteorological Applications*.

Jameson, A. R., 1985: Deducing the microphysical character of precipitation from multiple-parameter radar polarization measurements. *J. Climatol. and Appl. Meteorol.*, **24**, 1037-1047.

Joe, P. and S. Lapczak, 2002: Evolution of the Canadian operational radar network. Proceedings. 2nd European Conference on Radar in Meteorology and Hydrology (ERAD), Delft, Netherlands. pp.370-382.

Joss, J. and E. G. Gori, 1978: Shapes of raindrop size distributions. *J. Appl. Meteorol.*, **17**, 1054-1061.

Kennedy, P. C., S. A. Rutledge, 2011: S-Band dual-polarization radar observations of winter storms. *J. Appl. Meteor. Climatol.*, **50**, 844-858.

Korolev A. and G. Isaac, 2003: Roundness and aspect ratio of particles in ice clouds. *J. of Atmos. Sci.*, **60**, 1795-1807.

Kuhlman, K. M., and K. L. Manross, 2011: Lightning and polarimetric signatures of two electric winter storms in central Oklahoma. 91st AMS Annual Meeting, Washington, USA. [http://ams.confex.com/ams/91Annual/webprogram/Manuscript/Paper185790/Kuhlman_AMS2011.pdf].

Kumjian, M. R., Alexander V. Ryzhkov, Heather D. Reeves, and Terry J. Schuur, 2013: A dual-polarization radar signature of hydrometeor refreezing in winter storms. *J. Appl. Meteor. Climatol.*, **52**, 2549-2566.

Laws, J. O., and D. A. Parsons, 1943: The relations of raindrop size to intensity. *Trans. Amer. Geophys. Union*, **24**, 452-460.

Lo, K. K., and R. E. Passarelli, 1982: The growth of snow in winter storms: An airborne observational study. *J. Atmos. Sci.*, **39**, 697-706.

Luchs S., Zhang G., Ryzhkov A., Xue M., Ryzhkova L., Cao Q., 2009: Observations of snow particle size distribution with 2-D video disdrometer and polarimetric radar. 13th Conf. IOAS-AOLS, Phoenix, AZ, Paper P2.5.

MacDonald, J. P. and J. W. Pomeroy, 2008: Gauge undercatch of two common snowfall gauges in a prairie environment. *Proceedings of the Eastern Snow Conference, 64. 119-126*.

McCormick, G. C. and A. Hendry, 1975: Principles for the radar determination of the polarization properties of precipitation. *Radio Sci.*, **10**, 421-434.

McCormick, G. C. and A. Hendry, 1979: Techniques for the determination of the polarization properties of precipitation. *Radio Sci.*, **14**, 1027-1040.

McCormick, G. C., 1981: Polarization errors in a two-channel system. *Radio Sci.*, **16**, 67-75.

Marshall, J. S., R. C. Langille, and W. McK. Palmer, 1947: Measurement of rainfall by radar. *J. Meteor.*, **4**, 186–192.

Marshall, J. S., and W. McK. Palmer, 1984: The distribution of raindrops with size. *J. Meteor.*, **5**, 165-166.

Marshall, J. S., and K. L. Gunn, 1952: Measurement of snow parameters by radar. *J. Meteor.*, **9**, 322–327.

Minervin, V. E., and A. B. Shupyatsky, 1963: Radar method of determining the phase state of clouds and precipitation. *Tr. Cent. Aerolog. Obs.*, **47**, 63–84 (in Russian).

Morgunov, S. P., and A. B. Shupyatsky, 1964: Evaluation of artificial modification efficiency from the polarization characteristics of the echo signal. *Tr. Cent. Aerolog. Obs.*, **57**, 49–54 (in Russian).

Newell, R. E., S. G. Geotis, M. L. Stone, and A. Fleisher, 1955: How round are raindrops? Proc., *Fifth weather radar conf.*, Boston, MA, Amer. Meteor. Soc., 261-268.

Niu, S, X. Jia, J. Sang, X. Liu, C. Lu, and Y. Liu, 2010: Distributions of raindrop sizes and fall velocities in a semiarid plateau climate: Convective versus stratiform rains. *J. Appl. Meteor.*, **49**, 632-645.

Oguchi, T., 1983: Electromagnetic wave propagation and scattering in rain and other hydrometeors. *Proc. IEEE,* **9**, 1029-1078.

Otto, T. and H. W. J. Russchenberg, 2011: Estimation of specific differential phase and differential backscatter phase from polarimetric weather radar measurements of rain. *IEEE Geosci. Remote Sens. Let.*, **8**, 9880992.

Passarelli, R. E., 1978: Theoretical and observational study of snow-size spectra and snowflake aggregation efficiencies. *J. Atmos. Sci.*, **35**, 882-889.

Potter, J. G., 1965: Water content of freshly fallen snow. CIR-4232, TEC-569, Meteorology Branch, Dept. of Transport, Toronto, ON, Canada, 12 pp. [Available from National Snow and Ice Data Center User Services, University of Colorado, Campus Box 449, Boulder, CO 80309-0449].

Rasmussen, R., J. Vivekanandan, J. Cole, B. Myers, and C. Masters, 1999: The estimation of snowfall rate using visibility. *J. Appl. Meteor.*, **38**, 1542–1563.

Rasmussen, R., and Coauthors, 2001: Weather support to deicing decision making (WSDDM): A winter weather nowcasting system. *Bull. Amer. Meteor. Soc.*, **82**, 579-595.

Rasmussen, R., M. Dixon, S. Vasiloff, F. Hage, S. Knight, J. Vivekanandan, and M. Xu, 2003: Snow nowcasting using a real-time correlation of radar reflectivity with snow gauge accumulation. *J. Appl. Meteor.*, **42**, 20–36.

Rasmussen, R., B. Baker, J. Kochendorfer, T. Meyers, S. Landolt, A. P. Fischer, J. Black, J. M. Theriault, P. Kucera, D. Gochis, C. Smith, R. Nitu, M. Hall, K. Ikeda, and E. Gutmann, 2012: How well are we measuring snow? *Bull. Amer. Meteoro. Soc.*, **93**, 811-829.

Rodriguez, Y., W. Al Cooper, S. Goeke, J Goldstein, and C. Bousquet, 2001: Estimating snowfall rates using polarimetric radar data. SOARS, UCAR Library.

Roebber, P. J. S. Bruening, D. M. Schultz, J. V. Cortinas Jr, 2003: Improving snowfall forecasting by diagnosing snow density. *Wea. Forec.*, **18**, 264-287.

Rogers, R. R., and P. L. Smith, 1996: A short history of radar meteorlogy. Historical Essays on Meteorology 1919-1995, J. R. Fleming, Ed., Amer. Meteor. Soc., 57-98.

Ryzhkov, A. V., S. E. Giangrande, and T. J. Schuur, 2005: Rainfall estimation with a polarimetric prototype of WSR-88D. *J. Appl. Meteor.*, **44**, 502-515.

Ryzhkov, A. V., T. J. Schuur, and D. S. Zrinc, 2001: Radar rainfall estimation using different polarimetric algorithms. 30th International Conf. on Radar Meteorology, Munich, Germany.

Ryzhkov, A. V., P. Zhang, D. Hudak, J. L. Alford, M. Kniht, and J. W. Conway, 2007a: Validation of polarimetric methods for attenuation correction at C band. 33th International Conf. on Radar Meteorology, Cairns, Australia.

[https://ams.confex.com/ams/33Radar/techprogram/paper_123122.htm]

Ryzhkov, A. V., D. S. Zrnic, P. Zhang, J. Krause, H. S. Park, D. Hudak, J. Yong, J. L. Alford, M. Kniht, and J. W. Conway, 2007b: Comparison of polarimetric algorithms for hydrometeor classification at S and C bands, 33th International Conf. on Radar Meteorology, Cairns, Australia.

Saltikoff, E., A. Huuskonen, H. Hoti, J. Koistinen, and H. Jarvinen, 2010: Quality assurance in the FMI Doppler weather radar network. *Boreal Environment Research*, **15**, 579-594. ISSN 1239-6095.

Schneebeli, M., Nicholas Dawes, Michael Lehning, and Alexis Berne, 2013: High-resolution vertical profiles of X-band polarimetric radar observables during snowfall in the Swiss Alps. *J. Appl. Meteor. Climatol.*, **52**, 378-394.

Sekhon, R. S., and R. C. Srivastava, 1970: Snow size spectra and radar reflectivity. *J. Atmos. Sci.*, **27**, 299-307.

Sempere Torres, D., J., M. Porra, and J. D. Creutin, 1994: A general formulation for raindrop size distribution. *J. Appl. Meteorol.*, **33**, 1494-1502.

Sempere Torres, D., J., M. Porra, and J. D. Creutin, 1998: Experimental evidence of a general description for raindrop size distribution properties. *J. Geophys. Res. (D)*, **103**, 1785-1797.

Seliga, T. A., V. N. Bringi, 1976: Potential use of radar differential reflectivity measurements at orthogonal polarizations for measuring precipitation. *J. Appl. Meteor.*, **15**, 69-76.

Shupyatsky, A. B., 1959: Radar scattering by nonspherical particles. *Trans. Cent. Aerolog. Obs.*, **30**, 39–52 (in Russian).

Shupyatsky, A. B., and S. P. Morgunov, 1963: The application of polarization methods to radar studies of clouds and precipitation. *Tr. Vsesoiuznoe Nauchi Meteor. Soveshchaniia Leningrad*, 295–305 (in Russian).

Smith, P. L., 1984: Equivalent radar reflectivity factors for snow and ice particles. *J. Climate Appl. Meteor.*, **23**, 1258-1260.

Smith, J. A. and W. F. Krajewski, 1993: A modeling study of rainfall rate – reflectivity relationships. *Water Resour. Res.*, **29**, 2505-2514.

Snyder, J. C., H. B. Bluestein, G. Zhang, and S. J. Fraiser, 2010: Attenuation correction and hydrometeor classification of high-resolution, X-band, dual-polarized mobile radar measurements in severe convective storms. *J. Atmos. Oceanic. Technol.*, **27**, 1979-2001.

Strutt, J., 1899: On the transmission of light through an atmosphere containing small particles in suspension, and on the origin of the blue of the sky. Philosophical Magaz, 5, **47**, 375-394.

Theriault, J. M., R. Rasmussen, K. Ikeda, S. Landolt, 2012: Dependence of snow gauge collection efficiency on snowflake characteristics. *J. Appl. Meteor. Climatol.*, **51**, 745-762.

Thompson, E. J., S. A. Rutledge, and B. Dolan, 2014: A dual-polarization radar hydrometeor classification algorithm for winter precipitation. *J. Atmos. Oceanic Technol.*, **31**, 1457-1481.

Thurai, M., D. Hudak, and V. N. Bringi, 2008: On the possible use of copolar correlation coefficient for improving the drop size distribution estimates at C Band. *J. Atmos. Oceanic Technol.*, **25**, 1873-1880.

Trapp, R. J., M. D. Schultz, A. V. Ryzhkov, and R. L. Holle, 2001: Multiscale structure and evolution of an Oklahoma winter precipitation event. *Mon. Wea. Rev.*, **129**, 486-501.

Uijlenhoet, R., 1999: Parameterization of rainfall microstructure for radar meteorology and hydrology. Doctoral dissertation, Wageningen University, The Netherlands, 279 pp.

Uijlenhoet, R., 2001: Raindrop size distributions and radar reflectivity-rain rate relationships for radar hydrology. *Hydrol. Earth Syst Sci*, **5**, 615-637.

Ulbrich, C. W., 1983: An empirical method of accounting for variations in the form of the raindrop size distribution in dual-measurement techniques. *Preprints 21st Conf. Radar Meteorology*, Edmonton, Amer. Meteor. Soc., 317-322.

Ulbrich, C. W. and D. Atlas, 1984: Assessment of the contribution of differential polarization to improved rainfall measurements. *Radio Sci.*, **19**, 49-57.

Ulbrich, C. W. and D. Atlas, 1998: Rainfall microphysics and radar properties: analysis methods for raindrop size spectra. *J. Appl. Meteorol.*, **37**, 912-923.

VAISALA, 2002: Weather Sensor FD12P Users' Guide M210296en-A. [http://www.vaisala.com/Vaisala%20Documents/User%20Guides%20and%20Quick%20Ref%20Guides/FD12P%20User%20Guide%20in%20English.pdf].

Vivekanandan, J., W. M. Adams, and V. N. Bringi, 1999: Rigorous approach to polarimetric radar modeling of hydrometeor orientation distributions. *J. Appl. Meteorol.*, **30**, 1053-1063.

Vivekanandan, J., G. Zhang, S. M. Ellis, D. Rajopadhyaya, and S. K. Avery, 2003: Radar reflectivity calibration using differential propagation phase measurement. *Radio Sci.*, **38**(3), 8049.

Vulpiani, G., S. Giangrande, and F. S. Marzano, 2009: Rainfall Estimation from Polarimetric S-Band Radar Measurements: Validation of a Neural Network Approach. *J. Appl. Meteor. Climatol.*, **48**, 2022-2036.

Wang, Y., and V. Chandrasekar, 2009: Algorithm for estimation of the specific differential phase. *J. Atmos. Oceanic Technol.*, **26**, 2565-2578.

Whiton, R. C., 1971: On the use of radar in identifying tornadoes and severe thunderstorms: A diagnostic guide for scope interpretation. Air Weather Service Rep. AWS-TR-243, 18 pp.

Williams, E. R., D. J. Smalley, M. F. Donovan, R. G. Hallowell, K. T. Hood, B. J. Bennett, R. Evaristo, A. Stepanek, T. Bals-Elsholz, J. Cobb, and J. Ritzman, 2011: Dual polarization radar winter storm studies supporting development of NEXRAD-based aviation hazard products. AMS 35th Conf. on Radar Meteo., Pittsburgh, PA, USA. [http://ams.confex.com/ams/35Radar/webprogram/Paper191770.html].

Wexler, R., 1955: An evaluation of the physical effects in the melting layer. Proc., *Fifth Weather Radar Conf.*, Boston, MA, Amer. Meteor. Soc., 329–334.

Wiesner, J., 1895, Beitrage zur kennitniss des tropischen regens. *Akad, Wiss, Vienna, Math. Nat.* Klasse, Sitzungsb, **104**, 1397-1434.

Woods, C. P., M. T. Stoelinga, and J. D. Locatelli, 2008: Size spectra of snow particles measured in wintertime precipitation in the Pacific Northwest. *J. Atmos. Sci.*, **65**, 189-205.

Zrnic, D. S., and A. Ryzhkov, 1996: Advantages of rain measurements using specific differential phase. *J. Atmos. Oceanic Technol.*, **13**, 454-464.

Zrnic, D. S., T. D. Keenan, L. D. Carey, P. May, 2000: Sensitivity analysis of polarimetric variables at a 5-cm wavelength radar in rain. *J. Appl. Meteor.*, **39**, 1514-1526.

Zrnic, D. S., V. M. Melnikov, and A. V. Ryzhkov, 2006: Correlation coefficients between horizontally and vertically polarized returns from ground clutter. *J. Atmos. Oceanic Technol.*, **23**, 381-394.

Appendices

Appendix A: **FD12P Technical Notes and Reasons to Discard SWE Data**

The FD12P weather sensor is a multi-variable sensor for automatic weather stations and airport weather observing systems. One of its functions is measuring the intensity and quantity of both liquid and solid precipitation by employing a combination of a capacitive device named DRD12 and an optical receiver unit named FDR12. The DRD12 contains two RainCap^{TM} sensing elements that consist of thin wires protected by an insulating glass coating. The capacity of the elements will alter with the presence of precipitation on the instrument. Integrated heating resistors within the sensor are expected to keep the elements dry. The entire DRD12 unit is protected by a windshield to reduce the effect of wind during measurements. On the other hand, the FDR12 unit is a light receiver that detects rapid changes in the scattered signal and converts it to optical precipitation intensity and amount (FD12P User's Guide 2002).

A decision was made to adopt the wind-corrected GEONOR T-200B as ground truth in measuring SWE (mm h^{-1}) rather than FD12P on grounds of:

1. The DRD12 in FDR12 units, responsible for measuring SWE, has a small footprint with no method to correct catchment efficiency induced by wind while a WMO study (Goodison et al. 1998) satisfactorily compared the catch efficiency of the Nipher Shield to the Doubled Fence Intercomparison Reference (DFIR).
2. The wind shield around the DRD12 is not high enough to protect against blowing snow off the sensor. No such concern exists for the GEONOR.

3. The principle method of measurement in the DRD12 could produce errors during moderate and heavy snowfall as the heating resistance would be unable to melt all the snow accumulated on the sensing elements to measure SWE. Also, the heating resistance could result in a certain percentage of evaporation that would not be accounted for during each measurement. This case is not applicable to the GEONOR T-200B due to the presence of antifreeze that immediately melts the snow once it enters the container.